Distributional Fixed Point Equation model of island nucleation processes during submonolayer deposition

PhD Thesis

Hrvojka Krcelic

Department of Chemical and Process Engineering
University of Strathclyde, Glasgow

September 20, 2018

This thesis is the result of the author's original research. It has been composed by the author and has not been previously submitted for examination which has led to the award of a degree.

Acknowledgements

I would like to thank Paul Mulheran and Michael Grinfeld for their excellent guidance and for all of their generous help without which the completion of this work wouldn't be possible.

I would also like to thank my friends and colleagues for their support.

Abstract

In this thesis, we look into the problem of finding an analytical model for the submonolayer nucleation processes on a substrate. More specifically, we explore the Distributional Fixed Point Equation (DFPE) approach of modelling the size distribution of the gaps between nucleated islands (GSD) on a one dimensional substrate, and the size distribution of capture zones (CZD) around the islands (areas where a free monomer is more likely to be absorbed into the relevant island than to escape to the next one).

The DFPEs incorporate information about the critical island size, the nucleation mechanism (via diffusing monomers or through deposition) and the probability $P(a)$ of a new island nucleation occurring at a position a inside a gap. The corresponding distribution P_z for the capture zones is derived from the fragmentation probability P for the gaps, so it cannot be directly observed.

We develop a strategy to solve the inverse problem of calculating the distribution P and P_z from the Integral Equation form of the DFPE, for a known GSD and CZD, in which we build P and P_z as a finite Fourier series. Additionally, we solve the inverse problem in another way: by using the Tikhonov regularisation method, and compare these results against each other and with the theoretical predictions. For the case of the gaps, we can directly measure P during the kinetic Monte Carlo simulations. We compare the results to the previously calculated P and find good consistency.

For the capture zones, we define an alternative distribution, one that can be measured: the probability of fragmenting a zone at a position a, $Q(a)$. We then create an DFPE for this distribution Q, and we also use it to directly sample CZD. Since both approaches give promising results, we conclude our work by testing them on a two dimensional substrate, where we find that only the latter approach gives good results.

Contents

List of Figures

List of Tables

Chapter 1

Introduction

Studies of the initial stage of growth of nanoclusters and thin films on a substrate during deposition have been attracting a lot of interest since the 1960's because of its importance to the subsequent film properties and morphology.

One of the key interests is detailed characterization and understanding of the spatial arrangement of structures nucleated on a substrate, and their size distribution. This effort has its place in a broader goal of first elucidating and then controlling the formation of various nanostructures.

A lot of work has been done in this area, yet a lot of problems are still open research questions. We will begin setting the stage by explaining the basic processes and then proceed to the thesis motivation and aims.

1.1 Basic processes

An important method in ultrathin film growth is epitaxy: a method of depositing a crystalline overlayer on a crystalline substrate. The term epitaxy derives from Greek and denotes an ordering (*taxis*) on top or over (*epi*); the structure grown on top of a substrate will have some particular crystalline order determined by the substrate. Because of that, it is important in semiconductor thin film production, where certain levels of crystal lattice matching are required for the desired electronic properties. Homoepitaxy uses the same material both for the substrate and the deposited film and heteroepitaxy deposits a different material to the substrate.

Molecular beam epitaxy is an ultra high vacuum - based method (to minimize resulting surface defects) of producing epitaxial films of high purity, where atoms or single clusters of atoms (heated up so they are in gas phase) are slowly deposited onto a substrate so that layer by layer growth ensues, in a high vacuum environment [7]. The deposition rate F (deposition flux in newer literature) is measured in monolayers per unit time. Once on the substrate, monomers can re-evaporate (at high substrate temperature) or diffuse as adatoms across the surface, with a diffusion constant which can, to a very good approximation, be taken to be the Arrhenius rate [1] [8]:

$$D = D_0 e^{-E_d/k_B T} \tag{1.1}$$

where E_d is the activation energy for surface diffusion, k_B the Boltzmann constant and T the substrate temperature. The pre-exponential factor is given by $D_0 = \frac{1}{b}\nu a^2$, where b is the lattice connectivity ($b = 2$ in one dimension and in two $b = 4$), ν is attempt frequency (vibration frequency for hopping) and a is a lattice constant (in simulations, this is the distance between the lattice grid sites). In Molecular Dynamics (MD) simulations D_0 is typically of the order of atomic vibration frequency and is often set to $10^{-12} - 10^{-13} s^{-1}$ [9].

The average time in which a surface site will be hit by a depositing atom is $1/F$, and an adatom will diffuse away after a meantime $1/D$, so the growth dynamics depends on the ratio $R = D/F$ [1] [10]. Typical experimental values for growth are $R \sim 10^5 - 10^{10}$. Island density decreases with R increasing; for growing values of R the rates of diffusion become larger than the rate of deposition so adatoms can travel further before being absorbed into an island (the creation of islands is discussed below).

The kinetics of growth also depend on the percentage of the surface covered with atoms (coverage θ). Coverage is frequently used as a measure of time when desorption is negligible; then $\theta = Ft$, where t is the deposition time [2].

When diffusing adatoms collide, they can form a cluster, called an island, if the thermal energy k_BT is significantly smaller than the binding energy between the adatoms (or one adatom and the substrate surface, in case of a single adatom attaching to the surface). An important parameter is the critical island size i: islands made up of $i+1$ atoms are the smallest stable islands and are more likely to grow than decay.

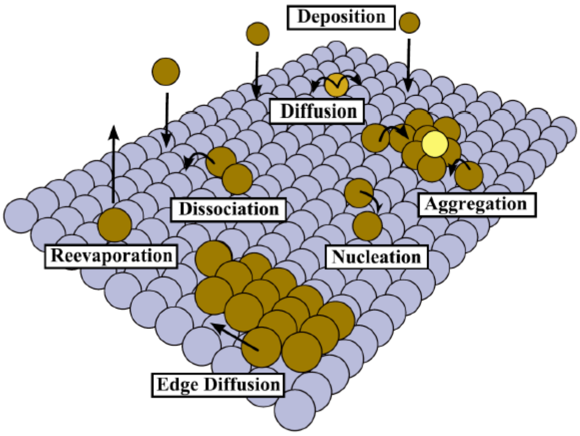

Figure 1.1: Elementary moves during early-stage deposition and growth. Figure taken from Ref. [1].

We distinguish three stages of growth [11] [12]:

a) in the initial (so-called *transient*) regime the adatom number density n_1 grows linearly in time according to the law $n_1 \simeq Ft$, leading to nucleation of far-distanced islands. This causes a "depletion zone" around these islands: adatoms surrounding them aggregate with the island which locally reduces n_1. Depletion zones grow (with radius $r \backsim (D\Delta t)^{1/2}$, Δt being the time elapsed since nucleation [13]) and start to cover most of the substrate surface. Finally, as they collide, they form boundaries of capture zones: areas surrounding an island where a diffusing monomer is more likely to aggregate to that particular island then to the neighbouring ones [14].

b) when the island density becomes approximately equal to adatom density, we enter the *aggregation* regime. The substrate surface is now completely tessellated by capture zones. Nucleation of new islands still occurs, but most deposited atoms will aggregate with existing islands. Since most of atoms deposited within a capture zone will aggregate with that zone's island, island growth rate is proportional to the capture zone area [3] [14].

c) at coverage around $20 - 40\%$ [15] [16], *coalescence* (merging) of islands occurs; after this stage second-layer growth will start.
In this work, we will be interested only in the aggregation regime.

The nucleation and growth of nanostructures can be studied with either completely deterministic (analytic) or completely stochastic models (typically kinetic Monte Carlo (kMC) simulations). Analytical theoretical models are required to interpret and extend kMC simulation results; the latter are widely used as an easy to obtain substitute for (more scarce) experimental data.

1.1.1 Kinetic Monte Carlo simulations

Kinetic Monte Carlo simulations of deposition and nucleation usually follow the same basic set of rules. They are performed on a lattice which is initially empty and are driven by diffusion and deposition steps. The ratio R dictates the procedure, since it determines the number of diffusion steps relative to the deposition steps [17] [18].

In deposition steps, new monomers are added randomly at an appropriate rate F. At each diffusion step a monomer is selected at random and moved by a unit length on the lattice, in a random direction, and in a deposition step a monomer is placed on a random lattice site. If a monomer arrives (or is deposited) to a position adjacent to another cluster of monomers, or to an existing stable island, it will be fixed on that position provided that the total number of monomers has exceeded i. This way islands nucleate and grow.

The main difference between different models is the shape of islands - they can be extended (dendritic, spherical) or point islands.

In the point island model they are kept as single points on the lattice and their size is recorded and incremented with the number of captured atoms. This way the island shape effects are alleviated and islands will not coalesce for large coverage θ, which makes this model a convenient way to study the asymptotic scaling limit $\theta \longrightarrow \infty$.

In an extended island model an s-size two-dimensional island occupies s sites on the lattice. Typically coalescence starts being relevant at approximately $\theta = 20\%$ [16].

For the purposes of this thesis, in our simulations we will use point island model on a one-dimensional substrate, and an extended spherical island model in two dimensions.

1.2 Research problem and the aim of the thesis

We have stated that this thesis will be looking only at the aggregation regime of the nucleation and growth. Within this regime, an interesting phenomena occurs: if the sizes of islands are divided by its average value (scaled to the average), the distribution of their sizes remains (approximately) the same as coverage grows. The same is true for the distribution of capture zone sizes.

As we show in the literature review in Chapter 2, the search for a satisfying analytical model which would reproduce the correct island size distribution (ISD) and capture zone distribution (CZD) is an active research topic.

This thesis adopts and explores a Distributional Fixed Point Equation (DFPE) model of Mulheran, O'Neill, Grinfeld and Lamb [5]. Limiting the problem to a one-dimensional substrate, they proposed an analytic model for the distribution of interisland gap sizes (gap size distribution, GSD) and the CZD.

On a 1d lattice, the creation of a new island is viewed as a fragmentation of the inter-island gap. Then the evolution of a gap (and a capture zone) is tracked: a new gap that was created when an older, larger gap (the parent gap) is fragmented via new island nucleation. In Chapter 3 we will explain the model and the derivation of the equations in detail; here it suffices to say it yields an integral equation:

$$\phi(x) = \int_0^{min(x,1)} \phi\left(\frac{x}{a} - 1\right) \frac{P(a)}{a} da, \tag{1.2}$$

where x is the gap size scaled to the average, ϕ is the gap size distribution and P is the probability that the new island nucleation occurs at a position $a \in [0, 1]$ within the (parent) gap. As we will explain in Chapter 2, it is proposed that the functional form of P:

$$P(a) = \frac{(2\alpha + 1)!}{(\alpha!)^2} a^{\alpha}(1-a)^{\alpha} \tag{1.3}$$

can be (independently of the DFPE model) derived from the monomer density profiles within the gap.

This theoretical P is derived from two idealized cases (giving the two values of α): the diffusion driven P (where it is taken that all of the nucleations are a result of collisions of $i + 1$ monomers diffusing along the lattice with the diffusion constant D), and the deposition driven P (where the nucleations are a result of a deposition of a monomer directly on top of, or next to, a pre-existing unstable cluster of i monomers).

Following a similar logic, an analysis of the capture zones yields the same functional form for the CZD:

$$\phi_z(z) = \int_0^{min(z,1)} \phi_z\left(\frac{z}{a_z} - 1\right) \frac{P_z(a_z)}{a_z} da_z, \tag{1.4}$$

where z is the capture zone size (scaled to the average) and ϕ_z is the CZD. Unlike the probability P for the gaps however, probability P_z doesn't have a straightforward physical meaning; it is a function derived from the probability P for the gaps. It is therefore also split in 2 idealized cases, diffusion and deposition.

The realistic nucleation processes on a lattice involve both cases, so the results of the kMC simulations lie roughly between these two distributions.

Equations (1.2) and (1.4) offer an analytic description of the nucleation within the scaling regime parametrized by i, and a unique possibility to determine P (P_z) from a known GSD (CZD), either from kMC simulation results or experimental data. Therefore, in this work we explore the model further.

The main goals of the thesis are:

1. to establish a reliable way of calculating P and P_z from a known GSD and CZD. Equation (1.3) gives two limiting idealized cases, so wish to calculate the true P and

P_z from a known GSD and CZD (the GSD and CZD obtained from a kMC simulation). Because equations (1.2) and (1.4) are an ill-posed problem, we need to regularise them in order to solve them. We can then see how much does one mode of nucleation contribute relative to the other.

2. test the extension of this one-dimensional model to two dimensions. The definition of capture zones (unlike that of gaps) doesn't depend on the dimension of the substrate, which leaves open the possibility of writing an equation for capture zone areas similar to Equation (1.4).

Some of the results from this thesis were presented in a talk on the 5th International Statistical Physics Conference (Sigma Phi 2017), held in Corfu, Greece. Chapter 7 has been converted to a paper; Ref. [19] is the arXiv preprint.

1.2.1 Thesis overview

Chapter 2 is a literature review which gives a (broad) background and establishes a niche for this work.

Chapter 3 introduces and explains the DFPE model from Ref. [5]; Equations (1.2) and (1.4) are derived here and the problem is set up.

In Chapter 4 we describe the numerical methods used to integrate Equation (1.2) as well as the simulation method we use throughout the thesis.

Chapters 5, 6 and 7 cover the problem of inverting equations (1.2) and (1.4). In Chapter 5 we use the textbook Tikhonov regularisation method to calculate P and P_z. We find that, while the strategy gives reasonable solutions relatively quickly, the expected symmetry and positivity of these solutions is not guaranteed.

In Chapter 6 we develop and alternative method, one that enforces symmetry and positivity, and solve the inverse problem for P and P_z.

In Chapter 7 we compare the best solutions from these two chapters. For the case of the gaps, it is possible to measure P directly during the kMC simulation; we collect the results and compare them to the results of the inverse problem.

Chapter 8 explores the fragmentation probability for the capture zones: while P_z used in Equation (1.4) is a mathematical construct that cannot be measured, it *is* possible to measure a fragmentation probability Q defined in a different way. This new distribution Q doesn't rely on gaps so its extension to 2d is straightforward. We write alternative equations for CZD that utilizes it; while the results aren't as good of a fit for the kMC obtained CZD as Equation (1.4) was, they are still encouraging enough to be tested in 2d.

Finally, in Chapter 9 we attempt to expand the model for the CZD to two dimensions. We find that our DFPE approach with fragmentation probability Q gives very poor results, due to its built-in (over) simplifications. We conclude our work with yet another model equation, one that still utilizes the distribution Q and gives fairly good results, which would make it the most promising future work direction.

Chapter 2

Literature review

2.1 Rate equations

The analytic approach utilizing Smoluchowski aggregation equations has been developed more than 50 years ago. Following previous work in classical nucleation theory, Walton [8] used a set of coupled ordinary differential equations (mean field rate equations) to describe the time evolution of mean field quantities such as the single atom or monomer density n_1 and densities of islands of size s (islands made of s atoms/monomers), n_s. It is assumed that only single adatoms are mobile, islands grow by capturing a single adatom at a time and these adatoms are randomly produced in their vicinity either by deposition or by release from an existing island. Also, direct impingement of atoms on islands is neglected. This gives an (infinite) set of rate equations (REs):

$$\frac{dn_1}{dt} = F - 2D\sigma_1 n_1^2 - Dn_1 \sum_{s\geq 2} \sigma_s n_s + 2\frac{1}{\tau_2} n_2 + \sum_{s\geq 3} \frac{1}{\tau_s} n_s \tag{2.1}$$

$$\frac{dn_s}{dt} = D\sigma_{s-1} n_1 n_{s-1} - D\sigma_s n_1 n_s + \frac{1}{\tau_{s+1}} n_{s+1} - \frac{1}{\tau_s} n_s, \quad s = 2, 3, ... \tag{2.2}$$

Term n_s/τ_s is the rate of dissociation of an island of size s (by single atom release); $1/\tau_s$ is the characteristic time for dissociation of an atom from an s-size island [20].

The term $D\sigma_s n_1 n_s$ is the rate of attachment of single atoms to s-size islands; σ_s are the so-called *capture numbers* of atoms by s-size islands. They are a measure of how effective an s-size island is in competing with other islands for the available adatoms.

In the first equation, each dimer formation results in the loss of two monomers or adatoms; so $D\sigma_1 n^2$ is multiplied by 2. The first equation states that the total density of single atoms is increased by deposition F, dissociation of an island made of two atoms and release of atoms from $s = 3, 4, ...$ -size islands; the adatom density is decreased by aggregation of two atoms into a $s = 2$ -size island and capture of an atom by $s = 2, 3, ...$-size islands.

The (missing) key ingredients for solving this system of equations are the capture numbers. The main problem of using REs is that the functional form of σ_s is not known.

The simplest assumption is that $\sigma_s = \sigma_{average} = const.$, which gives a good result for the average island density for $R \gg 1$ [1] [21].

A more sophisticated approach determined σ_s self-consistently from diffusion equations for adatom capture by a specific, s-size island. This resulted in capture numbers given in terms of Bessel functions K_0 and K_1 [2] [22]:

$$\sigma_s = 2\pi \frac{R_s}{\zeta} \frac{K_1(R_s/\zeta)}{K_0(R_s/\zeta)} \tag{2.3}$$

where R_s is the island radius (islands are taken to be circular) and ζ is the average distance an adatom travels before being captured by an island or another adatom; it is identified with the loss term in equation (2.1):

$$\zeta^{-2} = 2\sigma_1 n_1 + \sum_{s \geq 2} \sigma_s n_s \tag{2.4}$$

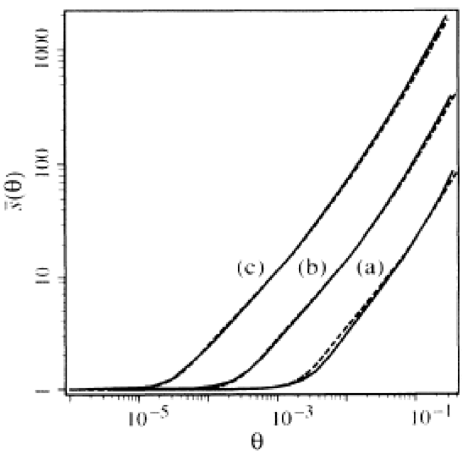

Figure 2.1: Average island size versus coverage for: (a) $D/F = 10^5$, (b) $D/F = 10^7$ and (c) $D/F = 10^9$. Dashed lines are numerical solutions from the RE and solid lines are obtained from kMC simulation. Figure taken from Ref. [2].

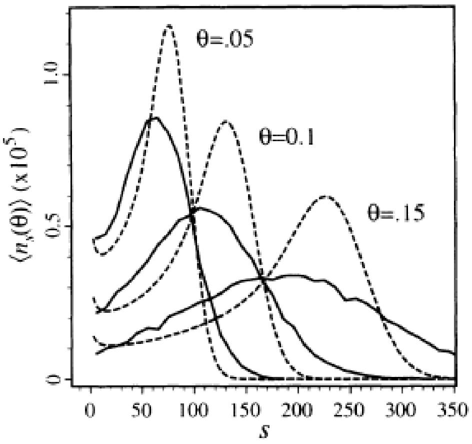

Figure 2.2: Island size distribution versus s (number of atoms in an island) at three different coverages. The dashed lines are obtained from RE and solid lines from kMC simulation. Figure taken from Ref. [2].

These attempts on the REs are perfectly adequate for average values (such as mean island size or total island density) but fail in the description of the island size distribution (ISD) [2] [21]. The reason for this is that the REs describe the growth of clusters that depend only on time and their sizes, but not on their local environments. Since it employs a mean field assumption that the surroundings of islands are independent of their shapes and sizes [21], it neglects the fact that larger islands have larger capture zones [14] and predict that all the islands grow with the same rate. This does not reproduce the correct form of the ISD and does not agree with simulations [2] [23], as is shown in Figures 2.1 and 2.2.

Properties of scale invariance are often observed in non-equilibrium growth processes. One example is the scale invariance of the ISD: the average island size changes during growth but the distribution of island size relative to the average does not. Much work has been done in an effort to explain and incorporate this, and scaling theory has been used in attempts to obtain the ISD from REs.

2.2 Scaling theory

Since the normalised ISD will at any time look the same when plotted against island size divided by the average island size ($s/\langle s\rangle$), the average island size $\langle s\rangle$ is the only relevant size scale. Therefore a scaling ansatz for solving the REs has been proposed early in the 1980's by Vicsek and Family [24]:

$$n_s(\theta) = \frac{\theta}{\langle s\rangle^2} f\left(\frac{s}{\langle s\rangle}\right) \tag{2.5}$$

where the scaling function $f(x)$ must satisfy the normalization and the first moment conditions [1]

$$\int_0^\infty f(x)dx = \int_0^\infty xf(x)dx = 1 \tag{2.6}$$

Since then the validity of (2.5) has been confirmed in simulations [25] [26] and experimentally, in STM studies [27], and it was used further by different authors [21] [15] [28]. The mean quantities $\langle s\rangle$, $\langle n_1\rangle$ and $\langle n\rangle$ (island size, monomer number density and total number density) can be written in the form [25] [26]:

$$\langle s\rangle \sim \theta^z R^x \tag{2.7}$$

$$\langle n_1\rangle \sim \theta^{-r} R^{-w} \tag{2.8}$$

$$\langle n\rangle \sim \theta^{1-z} R^{-x} \tag{2.9}$$

The exponents z, x, r, w have been obtained from simulation [26] and experiment [29] [30] for different modes of growth. They can also be obtained from the REs [25] [31] when an appropriate form of σ_s is chosen:

$$\sigma_s \sim s^p. \tag{2.10}$$

But despite the fact that this form of σ_s reproduces and agrees with the exponent values of (2.7) - (2.9) which concur with previous findings, there have been no report of a success in obtaining a correct ISD from RE with it.

2.2.1 ISD scaling function of Amar and Family

Amar and Family [32] proposed an explicit expression for the scaling function $f(s/\langle s\rangle)$:

$$f(x) = C_i x^i e^{-ia_i x^{1/a_i}} \tag{2.11}$$

where i is the critical island size and parameters C_i and a_i are such that $f(x)$ satisfies normalization conditions (2.6). This function fits both the ISD they obtained through kMC and the experimentally obtained ISD [27]. The dependence of the scaling function (2.11) on i allows identification of the critical island size from experimental data. To that end, it has been used in many analyses of experimental data [33–38].

The form of ISD scaling function (2.11) is accurate for $i = 1, 2, 3$; but an expression that works for $i = 0$ hasn't been found [32].

2.3 Refinements of capture numbers

2.3.1 Work of Bartelt and Evans - kMC obtained capture numbers

Bartelt and Evans [21] [39] performed kMC simulations to obtain σ_s numerically, from the mean number of attachments M_s to islands of size s during a time interval Δt. Then they calculated σ_s as $\sigma_s = M_s/(L^2 \Delta t D n_s n_1)$, where L is the lattice length, and found that it depends linearly on s for $s > \langle s\rangle$, where $\langle s\rangle$ is the average island size, and is almost exactly a constant for $s < \langle s\rangle$. Their simulation data agrees with capture numbers that were measured with STM in an experiment where first Co islands were formed on Ru(001) and then additional Cu was deposited [39].

Similar results for σ_s were obtained in a later experiment with Ag islands on Ag(001) [40].

Their simulation results strongly suggested a scaling ansatz for σ_s:

$$\frac{\sigma_s}{\langle\sigma\rangle} \sim C\left(\frac{s}{\langle s\rangle}\right) \tag{2.12}$$

Using (2.12), the ISD scaling function f, where they used $n_s \sim \theta/\langle s\rangle^2 f(x)$, $x = s/\langle s\rangle$, was obtained from the REs:

$$f(x) = f(0)exp\left(\int_0^x \frac{(2z-1) - C'(y)}{C(y) - zy}dy\right) \tag{2.13}$$

where $z = d(\ln\langle s\rangle)/d(\ln t)$.

2.3.2 Level set method of determining σ_s

A different way of obtaining σ_s numerically was undertaken by Gibou *et al.* [28] [41] [42]. They used a level-set method [41], a general technique for simulating the motion of moving boundaries (here, boundaries of an island) represented by a smooth function φ. Its motion is obtained from the evolution equation [43]:

$$\frac{\partial\varphi}{\partial t} = v_n|\nabla\varphi| \tag{2.14}$$

where v_n is the normal boundary velocity. It is determined by the influx of monomers to the island boundaries, which can, in turn, be calculated from the diffusion equation for the monomer number density. Since the island boundary velocity is describing island growth, σ_s can then be calculated from it.

Gibou *et al.* separated the nucleation regime from the island growth regime; they focused on the well established aggregation regime where they neglected new nucleations, thus making sure the existing capture zone network will not be rearranged by nucleations. In contrast to kMC, these σ_s are a function of time, but still they can only be obtained numerically.

Unlike the kMC results of Bartelt and Evans, this σ_s doesn't have a plateau; it has an approximately linear dependence on island size s both for $s < \langle s \rangle$ and for $s > \langle s \rangle$.

They were able to obtain a scaling function for ISD from the REs with these values of σ_s which agreed extremely well with kMC obtained ISD, however no analytic form of σ_s that would allow integration of the REs was found.

More recently, Körner, Einax and Maas extended the numerical study of σ_s using the same approach as Bartelt and Evans. They calculated σ_s as a function of both the island size s and coverage [44], and later as a function of island size, coverage and ratio R [45]. They used these numerically obtained $\sigma_s(\theta, R)$ to integrate the REs and the resulting ISD was in excellent agreement with the kMC obtained ISD.

An analytic variant of this was done by Dubrovskii and Sibirev [46], with a functional form $\sigma_s(\theta) = \alpha(\theta)(a + s - 1)$, with coefficient a and an arbitrary function $\alpha(\theta)$ that yield σ_s corresponding to the previously discussed kMC measured σ_s of Bartelt and Evans [21] and Körner, Einax and Maas [45]. A choice of $\alpha(\theta) = c\theta^p$ (with coefficient $c > 0$ and $p > -1$) was used to calculate the ISD from the REs [46]. A choice of $\alpha(\theta) = 1$ was also explored [47], corresponding to a closed system with discontinued deposition (so F is set to $F = 0$ in the REs).

An issue not addressed by these approaches is the fact that different islands of a particular size s have different capture areas, which is a result of the spatial fluctuations during island nucleations. These islands will then grow differently which cannot (easily) be incorporated into a single σ_s. An additional complication is that a capture area can greatly change if a new island nucleates near it [9].

2.4 Capture zone areas - substrate tessellation

Capture zones are generally identified as Voronoi cells [3] where the island centres are used as the Voronoi cell generators. A Voronoi cell is a polygon that encloses all of the points whose distance to that cell's generator (which is a predefined point) is less or equal than the distance to another cell's generator. So, for a network where the island centres are the generators, points of a particular cell are closer to the center of the corresponding island than to any other island's centre.

Since the size distribution of islands basically follows the associated Voronoi cells, scaling properties in such a model appear naturally, which can be seen on Figure 2.3 and 2.4 (Voronoi cells with generators in island centres, from [3]).

In a study of nucleation on substrate defect sites (so-called heterogeneous nucleation), Mulheran and Blackman found that a semi-empirical expression for capture zone area distribution, derived from random Voronoi networks, reasonably well matches the kMC data [3]:

$$A(z) = \frac{\beta^{\beta}}{\Gamma(\beta)} z^{\beta-1} e^{-\beta z} \tag{2.15}$$

where z is the cell area divided by the average cell area, and β an empirical parameter. (For a more general form of (2.15) in 1, 2 and 3 dimensions see [48]).

This Gamma distribution fit was used by a number of authors; in 2d for simulation results [49] [50] and for experimental data [51–54], and also for 1d simulations [55] (here, it was also used to fit the ISD).

A refinement of this tesselation was also made, with the Voronoi cells generated around the island's edges (Edge Cells) [14] [11] [40] instead of its centre. It was reported [14] that for the case of nucleation via monomer diffusion (so-called homogeneous nucleation), Edge Cells make a small but visible improvement over cells with islands centres as generators. (In the case of nucleation on substrate defects sites (heterogeneous nucleation), substituting one type of cells with the other made no difference.) It was also claimed [11] that Edge Cells are a necessary improvement for large islands (large coverages).

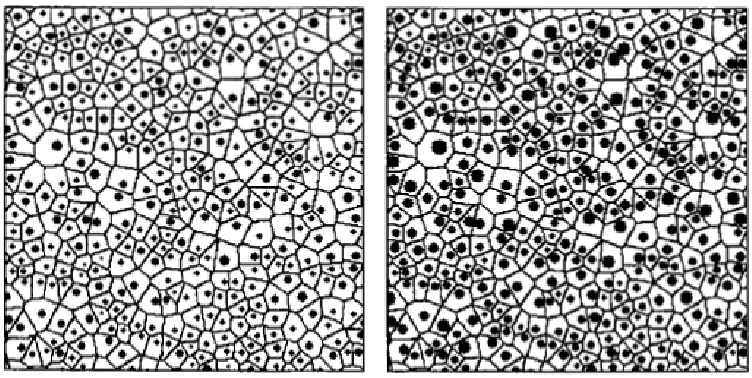

Figure 2.3: Snapshots of growing islands in their Voronoi cells, at coverage $\theta = 10$ and 20%. Voronoi network was generated after the simulation. Figure taken from Ref. [3].

Amar, Family and Popescu used a set of Voronoi cell area (island-size dependant) evolution equations coupled to the usual REs for island densities [56] and obtained capture numbers as a function of coverage out of it.

A different study was undertaken by Mulheran and Robbie [57] [58], who used the concept of capture zones to make a Joint Probability Distribution for island sizes and capture zone areas and constructed RE governing their evolution. If $n_{s,z}$ is a distribution of islands of size s with a capture zone area z, then its time evolution is given by the RE:

$$\frac{dn_{s,z}}{dt} = P(s-1,z) - P(s,z) + \sum_{z+} P^{\#}_{s,z+} \frac{d\left(\sum_{s>i} n_s\right)}{dt} - P^{\#}_{s,z} \frac{d\left(\sum_{s>i} n_s\right)}{dt}. \tag{2.16}$$

Here the term $P(s,z)$ is the probability that an island of size s and capture zone area z absorbs another monomer. This is composed of the case when a diffusing monomer hits the island ($P \sim \sigma_{s,z} n_{s,z} n_1$) and the case of a monomer being deposited onto the island ($P \sim F n_{s,z}$).

$P^{\#}_{s,z}$ is the probability that a newly nucleated island's cell is overlapping the existing

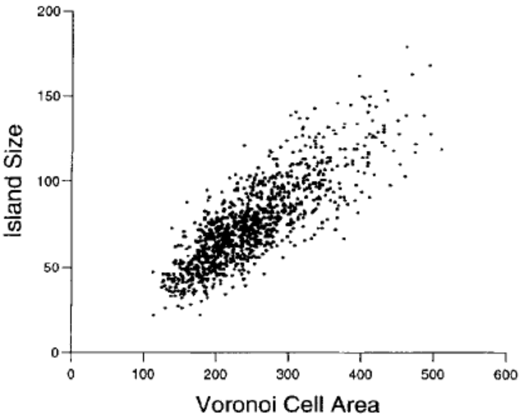

Figure 2.4: The correlation between island size and Voronoi cell area, in units of lattice constant squared. Figure taken from Ref. [3].

cell (of size z) of the island (of size s). If the cell before this new nucleation was of size z, new nucleation will decrease $n_{s,z}$. If the cell was larger, of some size $z+ > z$, then $n_{s,z}$ will increase. Then, the third term in (2.16) is the gain term for $n_{s,z}$ accounting for increase of cells of size z belonging to islands of size s, and the fourth term is the loss term.

This approach was later explored further by Bartelt and Evans [59] [60].

2.4.1 Generalised Wigner surmise

Pimpinelli and Einstein [61] proposed the generalised Wigner surmise (GWS) as a model function for the CZD. It is a probability distribution function rooted in random matrix theory and it can, for this problem, be written in the form:

$$A_\beta(z) = a_\beta z^\beta e^{-b_\beta z^2} \tag{2.17}$$

where z is the capture zone area divided by its mean. The constants a_β and b_β are determined by normalization conditions $\int_0^\infty A(z)dz = \int_0^\infty zA(z)dz = 1$:

$$a_\beta = \frac{2\Gamma\left(\frac{\beta+2}{2}\right)^{\beta+1}}{\Gamma\left(\frac{\beta+1}{2}\right)^{\beta+2}}, \quad b_\beta = \left[\frac{\Gamma\left(\frac{\beta+2}{2}\right)}{\Gamma\left(\frac{\beta+1}{2}\right)}\right]^2 \tag{2.18}$$

The single parameter β is given by:

$$\beta = \begin{cases} \frac{2}{d}(i+1) & \text{if } d = 1,2 \\ (i+1) & \text{if } d = 3 \end{cases}$$

where d is the spatial dimension and i is the critical island size.

Equation (2.17) is qualitatively similar to semi-empirical distribution (2.15) that followed from Voronoi tessellation, but decays faster which makes it less skew and shifts the peak towards a larger z. Unlike the gap fragmentation equation (2.29), it is claimed to hold for all dimensions. However, in kMC simulations performed in $d = 1, 2, 3, 4$ dimensions for the $i = 1$ point island model [62], it was found that, specifically for $d = 1$, CZDs are narrower and with a higher peak than predicted by GWS.

In the 2d case with $i = 1$, it was found that a different, higher β is required for a good fit and a case was made that the general form of $A(z)$ is more complex than the GWS model [63]. This, along with observed experimental data on twodimensional island growth, led Einstein and Pimpinelli to modify the original $\beta = i + 1$ to $\beta = i + 2$ [64].

The small size asymptotic behaviour ($z \longrightarrow 0$) of the model has been questioned in Ref. [65].

In later publications, Einstein and Pimpinelli discussed the limitations of the model for large zone sizes, and suggested it to be a good approximation at least in the midrange of scaled CZ sizes ($[0.5, 2]$) [64].

The GWS has been used to fit experimental data in several studies, from which i was deduced [54] [66] [38].

2.5 Fragmentation approach

Instead of describing nucleation with the formalism of classical nucleation theory through the REs, it can be viewed as a fragmentation process: each new nucleation fragments the relevant cell.

2.5.1 Precursor: Work of Blackman and Mulheran (1d lattice)

Adatoms diffusing near islands locally satisfy the diffusion equation [2] [15] [9]:

$$\frac{\partial n_1}{\partial t} - D\nabla^2 n_1 = F - Dn_1 \left[2\sigma_1 n_1 + \sum_{s\geq 2} \sigma_s n_s \right] \tag{2.19}$$

where the last term is the rate of nucleation of new islands and attachment onto existing ones. In the aggregation regime, when the single atom density n_1 is in approximate steady state, $n_1(X)$ between two point islands situated at $X = 0$ and $X = Y$ on a one-dimensional substrate satisfies the steady-state diffusion equation:

$$D\frac{d^2 n_1}{dX^2} + F \simeq 0 \tag{2.20}$$

The solution is the saturated form of the monomer density:

$$n_1(X) = \frac{1}{2R} X(Y - X), \quad 0 \leq X \leq Y \tag{2.21}$$

and integrating this over the interval $X \in [0, Y]$ gives the total number of single adatoms (monomers) in a gap: $n_{1,TOT} = Y^3/12R$. By averaging $n_{1,TOT}$ over all the gaps along the substrate we get average adatom density $\langle n_1 \rangle = \langle Y^3 \rangle \langle n \rangle /12R$, where $\langle n \rangle$ is the (mean) total density of islands, $\langle n \rangle = \sum_s \langle n_s \rangle$. With average gap size $\langle Y \rangle = 1/\langle n \rangle$ and scaled variable $y = Y/\langle Y \rangle$ we have:

$$12\langle n \rangle^3 \langle n_1 \rangle R = \langle y^3 \rangle \tag{2.22}$$

To get the capture zone distribution (in one dimension), two gaps (one to the left and the other to the right of the point island) are bisected. With the assumption that there is no correlation between the sizes of two gaps, the capture zone distribution $A_c(z)$ is:

$$A_c(z) = 2\int_0^{2z} \phi(y)\phi(2z - y)dy \tag{2.23}$$

where ϕ is the gap size distribution. This equation was numerically solved with numerical values of $\phi(y)$ from the relation (2.22); the result compares favourably with data obtained through kMC simulation [15].

This approach was extended by Amar *et al.* [56] [67] for the two-dimensional substrate, again with fairly good comparison of ISD with kMC data; however the capture zone area distribution was less satisfactory.

2.5.2 Gap fragmentation equation

On a 1d substrate, given the steady - state monomer density (2.21), the probability of a nucleation occurring is proportional to $n_1(X)^\alpha$, where α reflects the nature of nucleation [68]:

a) for $\alpha = i+1$ nucleation is driven by diffusion of monomers and $i+1$ of them are needed to form a stable island, and

b) for $\alpha = i$, stable islands are created when a monomer is newly deposited next to (or directly onto) a pre-existing cluster made up of i monomers.

A nucleation in the gap of width Y ('parent gap') results in creation of two new gaps ('daughter gaps') of widths X and $Y-X$. Processes like this are usually described with the linear fragmentation equation [65] [69] [70]:

$$\frac{\partial}{\partial t}u(X,t) = -a(X)u(X,t) + \int_X^\infty b(X|Y)a(Y)u(Y,t)dY \tag{2.24}$$

where $u(X,t)$ is the number density of gaps of widths X at time t, $a(X)$ is the rate of fragmenting gaps of width X and $b(X|Y)$ denotes the distribution of gaps of width X that were created by fragmentation of the parent gap of width Y. Conditions:

$$\int_0^Y b(X|Y)dX = 2, \qquad \int_0^Y Xb(X|Y)dX = Y \tag{2.25}$$

enforce the fact that each nucleation produces exactly two new gaps and that the total width of all gaps is preserved. Since the probability of a new nucleation in a gap of width Y is proportional to $n_1(X)^\alpha$, $a(Y)$ is given by [65]:

$$a(Y) = \int_0^Y X^\alpha (Y-X)^\alpha dX = B(\alpha+1, \alpha+1) Y^{2\alpha+1} \tag{2.26}$$

where B is the Beta function and the probability that this nucleation will occur at a position $r = X/Y$ in the gap is proportional to:

$$h(r) = r^\alpha (1-r)^\alpha, \qquad 0 \leq r \leq 1 \tag{2.27}$$

When properly normalised, this becomes:

$$p(r) = \frac{r^\alpha (1-r)^\alpha}{B(\alpha+1, \alpha+1)} = \frac{(2\alpha+1)!}{(\alpha!)^2} r^\alpha (1-r)^\alpha \tag{2.28}$$

Now the fragmentation equation (2.24) can be written as:

$$\frac{\partial}{\partial t} u(X,t) = -B(\alpha+1, \alpha+1) X^{2\alpha+1} u(X,t) + 2 \int_X^\infty \left(X(Y-X)\right)^\alpha u(Y,t) dY \tag{2.29}$$

This is a special form of a linear, homogeneous fragmentation equation which admits similarity solutions [65] [70]:

$$u(X,t) = \langle X(t) \rangle^{-2} \phi(X / \langle X(t) \rangle) \tag{2.30}$$

where $\langle X \rangle$ is the average gap size and the *reduced distribution* ϕ satisfies the norm conditions $\int_0^\infty \phi(Y) dY = \int_0^\infty Y \phi(Y) dY = 1$. With (2.30), asymptotic behaviour is found [65] [68]:

$$\phi(x) \sim k x^\alpha \quad as \quad x \longrightarrow 0 \tag{2.31}$$

$$\phi(x) \sim k x^{-2} \exp\left(-c x^{2\alpha+1}\right) \quad as \quad x \longrightarrow \infty \tag{2.32}$$

where k, c are constants and $x = X/\langle X\rangle$.
The connection with the CZD is given in (2.23), and with this the small-size asymptotic CZD behaviour is:

$$A(z) \sim kz^{2\alpha+1} \quad as \quad z \longrightarrow 0 \tag{2.33}$$

The large-size asymptotics of CZD can be calculated only for the case $\alpha = 1$, $i = 0$:

$$A(z) \sim kz^{-9/2} \exp\left(-2z^3/\mu^3\right) \quad as \quad z \longrightarrow \infty \tag{2.34}$$

where $\mu > 0$ is a constant.
These results were in good agreement with extensive kMC simulations results [68], but an extension to a dimension $d > 1$ wasn't possible.

In a later publication [5], a model equation for the GSD and CZD was derived within the gap fragmentation framework on a 1d lattice: the Distributional Fixed Point Equation (DFPE). The DFPE model is the topic of this thesis, so we will dedicate the next chapter to the work previously done on it.

Chapter 3

Previous work on the DFPE model

Inspired by work of Seba who modelled the distribution of spacings between parked cars on a street [4], Mulheran *et al.* devised a new model for the GSD and CZD [5].

On a 1d substrate and within a point-island model, a gap of size x (daughter gap) was created when a larger (parent) gap of size $x + y$ fragmented. Here the sizes of gaps are scaled to the average: $x = X/\langle X \rangle$. Since y is unknown (the procedure of fragmenting new gaps is a stochastic one) and because the sizes of gaps are scaled to average, a mean field approximation is used: $y = 1$. Now the statistics of processes where a parent gap of size $x + 1$ breaks into proportions a and $1 - a$ is described with a distributional fixed-point equation (DFPE):

$$x \triangleq a(1 + x) \tag{3.1}$$

The symbol $\triangleq$ means that the left and right side of the equation have the same distribution (so, the random variable x on the left and x on the right are drawn separately from the same distribution).

3.1 The Dickman distribution

Seba had used the DFPE (3.1) to model the distribution of open spaces between cars parked in a street. By x he denoted the distance between car bumpers (scaled to the average) and, again, $a \in [0, 1]$ determines the proportions this open space will break into when a new car parks in it. For $a = 0$ the new car will park immediately in front of the left edge of the parking space, for $a = 1$ it parks on the right edge and for $a = 1/2$ it parks exactly in the middle.

With the presumption that a new car will park on a random position in the open space, without any preference, a will have the probability density:

$$P(a) = 1, \qquad a \in [0, 1] \tag{3.2}$$

This yields the well-known case of the Dickman distribution [71]. Figure 3.1 shows the distribution of open spaces for this case.

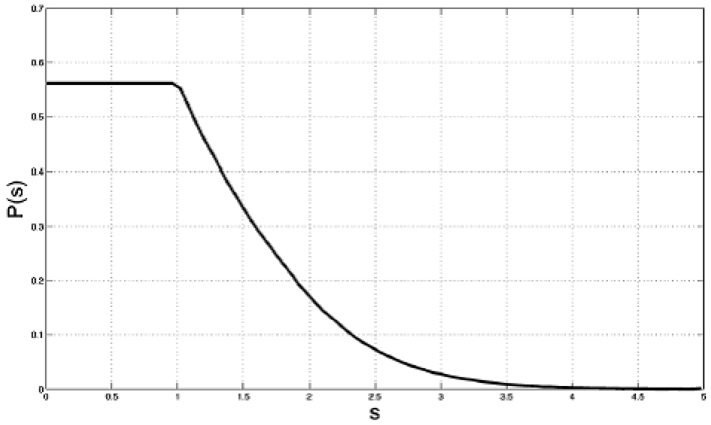

Figure 3.1: Probability distribution of open spaces (scaled to the average), for the Dickman case ($P(a) = 1$, $a \in [0, 1]$). Figure taken from Ref. [4].

However, the Dickman case isn't a realistic model for parked cars; at minimum it is reasonable to expect $P(0) = P(1) = 0$. Seba used a probability density $P(a)$ given with a Beta function to model the measured distances between parked cars on a street in a city in Czech republic [4]. This has also been used to model the distances of birds sitting on a power line [72].

3.2 Modelling the GSD and CZD with DFPE

The probability of fragmenting a gap into proportions a and $(1-a)$, as described by the DFPE $x \triangleq a(1+x)$, is denoted by $P(a)$. $\phi(x)$ denotes the probability distribution function of gaps $x \in [0, \infty)$ and $\Phi(x)$ is the cumulative distribution function (CDF) that corresponds to it; defined as:

$$\Phi(x) = \int_0^x \phi(x_1) dx_1 \tag{3.3}$$

As in Ref. [4], with this an Integral Equation can be derived from the DFPE:

$$\begin{aligned}
\Phi(x) &= \text{Prob}[x_1 \leq x] \\
&= \int_0^1 \text{Prob}[a(1+x_1) \leq x|a] P(a) da \\
&= \int_0^1 \text{Prob}[x_1 \leq x/a - 1] P(a) da \\
&= \int_0^1 \Phi\left(\frac{x}{a} - 1\right) H\left(\frac{x}{a} - 1\right) P(a) da
\end{aligned} \tag{3.4}$$

Here the Heaviside step function $H(r)$ (zero for $r \leq 0$, otherwise one) enforces the fact that $\Phi(r) = 0$ for $r \leq 0$. Then, since a can take values in interval $[0, 1]$, argument of H is equal or greater than zero only if $a \leq x$:

$$\Phi(x) = \int_0^{min(x,1)} \Phi\left(\frac{x}{a} - 1\right) P(a) da \tag{3.5}$$

Since the probability density function is the derivative of the CDF, it can be determined by differentiating (3.5) in two regions, $x < 1$ and $x > 1$ (since it is not clear if Φ is differentiable at $x = 1$). With the Leibniz rule:

$$\frac{d}{dx} \int_A^B \Phi(a, x) P(a) da = \int_A^B \frac{\partial}{\partial x} \Phi(a, x) P(a) da + \Phi(B, x) P(B) \frac{dB}{dx} - \Phi(A, x) P(A) \frac{dA}{dx} \tag{3.6}$$

for $x < 1$ (3.5) gives:

$$\begin{aligned}\phi_L(x) = \frac{d}{dx}\Phi(x) &= \int_0^x \frac{\partial}{\partial x}\Phi\left(\frac{x}{a}-1\right)\frac{P(a)}{a}da + \Phi\left(\frac{x}{x}-1\right)P(x) \\ &= \int_0^x \phi\left(\frac{x}{a}-1\right)\frac{P(a)}{a}da \end{aligned} \tag{3.7}$$

since $\Phi(0) = 0$. For $x > 1$ (3.5) gives

$$\phi_R(x) = \frac{d}{dx}\Phi(x) = \int_0^1 \frac{\partial}{\partial x}\Phi\left(\frac{x}{a}-1\right)\frac{P(a)}{a}da = \int_0^1 \phi\left(\frac{x}{a}-1\right)\frac{P(a)}{a}da \tag{3.8}$$

Since the left side limit:

$$\lim_{x\to 1^-}\phi_L(x) = \int_0^1 \phi\left(\frac{x}{a}-1\right)\frac{P(a)}{a}da \tag{3.9}$$

and the right side limit:

$$\lim_{x\to 1^+}\phi_R(x) = \int_0^1 \phi\left(\frac{x}{a}-1\right)\frac{P(a)}{a}da \tag{3.10}$$

are the same, $\Phi(x)$ *is* differentiable at $x = 1$ and (3.7) and (3.8) can be written as:

$$\phi(x) = \int_0^{min(x,1)} \phi\left(\frac{x}{a}-1\right)\frac{P(a)}{a}da \tag{3.11}$$

This is the Integral Equation (IE) for DFPE and it holds for any differentiable $P(a)$, $a \in [0, 1]$. It can be solved iteratively if $P(a)$ is known.

The probability that the nucleation will occur at a position a was already obtained in the fragmentation equation model (Equation (2.28)):

$$P(a) = \frac{a^\alpha(1-a)^\alpha}{B(\alpha+1,\alpha+1)} = \frac{(2\alpha+1)!}{(\alpha!)^2}a^\alpha(1-a)^\alpha \tag{3.12}$$

where $B(m, n) = \Gamma(m)\Gamma(n)/\Gamma(m + n)$ is the Beta function and parameter α holds information about the dominant nucleation mechanism - diffusion or deposition. For

$\alpha = i + 1$ islands are nucleated by $i + 1$ diffusing monomers and for $\alpha = i$ an island nucleated when a monomer was deposited in the vicinity of a pre-existing cluster of size i.

Equation (3.12) assumes that the diffusing monomers are in a steady - state (with a saturated density profile described by Equation (2.21)).

Specially, for the case $i = 0$ and $\alpha = i$, an analytic expression for ϕ was found [5]:

$$\phi(x) = \frac{3x^2}{\Gamma(2/3)\mu^3} \int_{(x/\mu)^3}^{\infty} t^{-4/3} e^{-t} dt, \quad \text{where} \quad \mu = \frac{4}{3}\Gamma\left(\frac{2}{3}\right). \tag{3.13}$$

With $P(a)$ given with (3.12), the small-size asymptotic form of (3.11) is:

$$\phi(x) \sim kx^{\alpha} \quad as \quad x \longrightarrow 0 \tag{3.14}$$

as it was in the fragmentation equation approach (2.31). The large-size asymptotics couldn't be obtained analytically [5].

Figure 3.2 shows kMC simulation results used to test the DFPE model. For $i > 0$ there is virtually no difference between the scaled GSD $\phi(x)$ for the extended and the point island model.

Figure 3.3 compares GSD $\phi(x)$ obtained through kMC simulations in a point-island model and coverage 100% with the solutions of IE (3.11), for $\alpha = i + 1$ and $\alpha = i$ case. Equation (3.13) is shown on the $i = 0$ panel. The kMC data is (roughly) between the $\alpha = i$ and the $\alpha = i + 1$ case of the IE, suggesting that both the deposition and diffusion driven cases of the DFPE (IE) model contribute to the actual nucleation on the lattice.

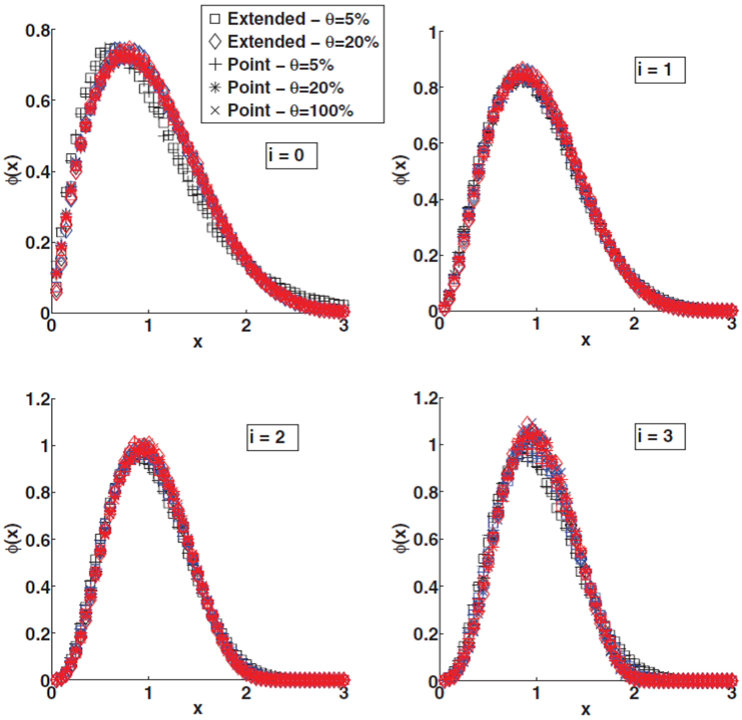

Figure 3.2: GSD for extended and point islands obtained from kMC with coverages $\theta = 5\%$, 20% and (just for point islands) 100%. Black symbols are for the case $R = 10^7$, blue and light gray for $R = 10^8$ and the red and dark grey for $R = 10^9$. Data for $R = 10^9$ and $\theta = 100\%$ on the $i = 3$ panel are not included. Figure taken from Ref. [5].

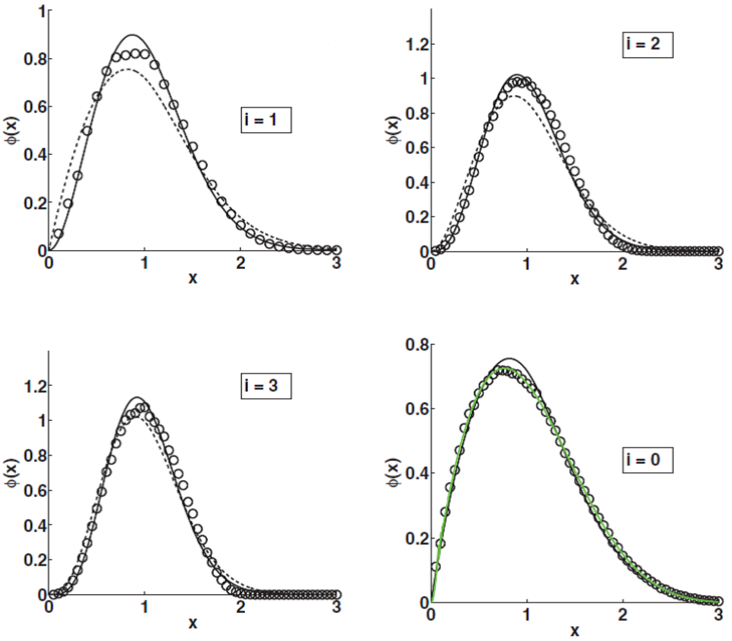

Figure 3.3: GSD obtained through kMC simulations in a point-island model and coverage 100% (empty circles) compared to the solution to integral equation (3.11) for diffusion ($\alpha = i + 1$) and deposition driven ($\alpha = i$) nucleation processes, plotted with a full and dotted black line, respectively. On the bottom right panel equation (3.13) is plotted with a green line. Figure taken from Ref. [5].

3.2.1 CZD

The capture zone distribution function can be obtained from the gap size distribution (3.11) through equation (2.23) of the previous section (assuming the neighbouring gap sizes aren't correlated); but it can also be obtained via another DFPE.

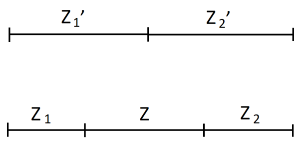

Figure 3.4: The sizes of capture zones. Capture zones of sizes z_1' and z_2' were split into three zones, smaller z_1 and z_2 and the new z.

The capture zone z (scaled to average) on Figure 3.4 can be viewed as a part of a previously larger zone z_1' on the left, and a part of z_2' on the right, that is:

$$z \triangleq \frac{a_1}{2}(z + z_1) + \frac{a_2}{2}(z + z_2). \tag{3.15}$$

With the mean field approximation $z_1 = 1 = z_2$ this becomes:

$$z \triangleq \frac{1}{2}(a_1 + a_2)(1 + z), \tag{3.16}$$

where a_1 and a_2 are both drawn separately from the distribution (3.12).
The corresponding integral equation is:

$$\phi_z(z) = \int_0^{min(z,1)} \phi\left(\frac{z}{a_z} - 1\right) \frac{P_z(a_z)}{a_z} da_z \tag{3.17}$$

where

$$a_z = \frac{a_1 + a_2}{2}. \tag{3.18}$$

Comparison with kMC data and the generalised Wigner surmise is shown on Figure 3.5.

3.3 Non - mean field DFPE model

The DFPE for the GSD: $x \triangleq a(x+1)$ involves a mean field approximation (setting the average neighbouring gap to 1). A non - mean field version is possible:

$$x \triangleq a(x_1 + x_2), \tag{3.19}$$

where x, x_1 and x_2 are all drawn from the same distribution. The corresponding integral equation is (derivation in the Appendix):

$$\phi(x) = \int_0^1 da \int_0^{x/a} dx_1 \cdot \phi\left(\frac{x}{a} - x_1\right) \phi(x_1) \frac{P(a)}{a}. \tag{3.20}$$

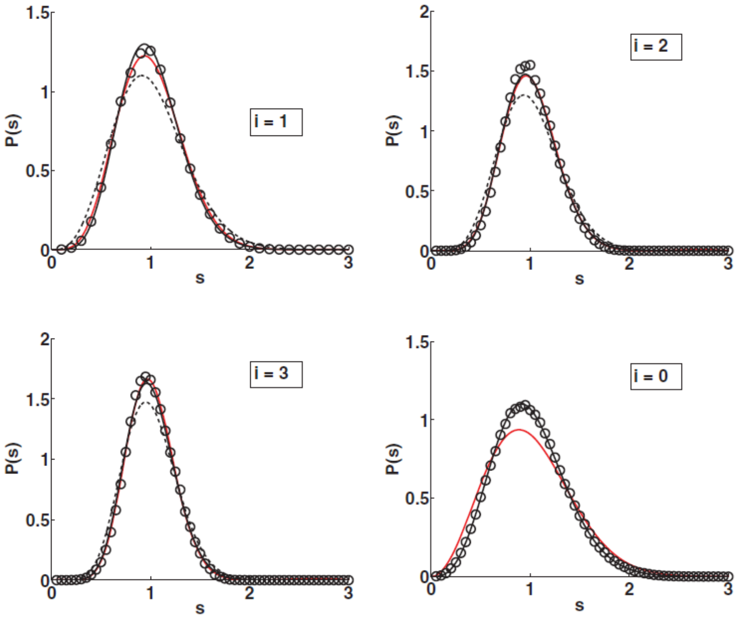

Figure 3.5: CZD from generalised Wigner surmise (red line), DFPE for $\alpha = i + 1$ (full black line) and $\alpha = i$ (dotted black line), and kMC data (empty circles) in point island model, with coverage $\theta = 100\%$. Figure taken from Ref. [5].

While the equation (3.19) moves past the approximation of setting $x_2 = 1$, it does not take into account that not all gaps are chosen with the same probability: the large gaps are more likely to be fragmented. To account for that, it was proposed that the gap x_1 still be drawn from $\phi(x_1)$ but after x_1 is chosen, the gap x_2 needs to be drawn with a bias. Gap of size $(x_1 + x_2)$ is fragmented with probability $(x_1 + x_2)^{2\alpha+1}$ (as in Eqn. (2.26)) so x_2 is not drawn from $\phi(x_2)$ but from the skewed distribution: $(x_1 + x_2)^{2\alpha+1}\phi(x_2)$. The resulting, biased integral equation is then:

$$\phi(x) = \int_0^1 da \int_0^{x/a} \phi\left(\frac{x}{a} - x_1\right) \phi(x_1) P(a) \frac{x^{2\alpha+1}}{a^{2\alpha+2}} dx_1. \tag{3.21}$$

Figure 3.6 shows the difference between the mean field IE (3.11), and non-mean field unbiased and biased Eqns. (3.20) and (3.21), for the values of $\alpha = 1, 2, 3$ and 4. The unbiased Eqn. (3.20) overestimates the number of smaller gaps, which is fixed by by the bias.

The biased Eqn. (3.21) grows closer to the mean field Eqn. (3.11) as α grows, so

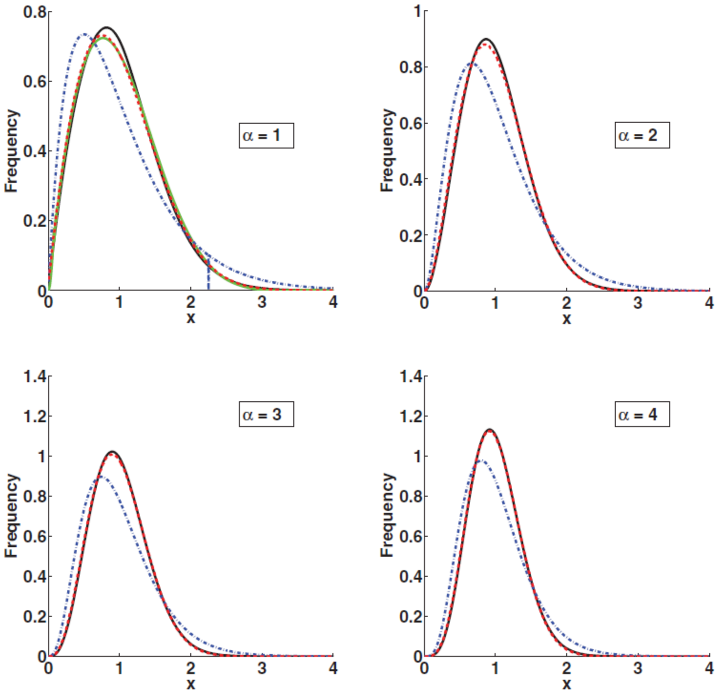

Figure 3.6: Mean field IE (3.11) (full black line), unbiased non-mean filed Eqn. (3.20) (dotted blue) and biased Eqn. (3.21) (dotted red), for $\alpha = 1, 2, 3$ and 4. Upper left panel ($\alpha = 1$) additionally shows Eqn. (3.13) with a full green line. Figure taken from Ref. [5].

the non-mean field refinement of the DFPE will only be a visible improvement to the mean field approximation for lower cases of i.

The mean field DFPE (3.1) (and its corresponding IE (3.11)) gives us two idealized model cases: nucleation which is driven only through diffusion ($\alpha = i + 1$), and only through deposition ($\alpha = i$).

For $i = 0$, setting $\alpha = i = 0$ (the deposition case) in Eqn. (3.12) gives $P(a) = 1$, which leads to the Dickman distribution. Such a $P(a)$ is a very poor physical model; it expects that every monomer on the lattice has the same probability of sticking to the surface (forming an island) regardless of its surroundings. We will nevertheless treat the case of the Dickman distribution as it were a valid deposition model for $i = 0$, mainly because we have no alternative model for this case but also because the distribution itself is an interesting one.

It is important to notice that modelling GSD and CZD with the mean field DFPE and its IE (3.11) and (3.17) includes two separate assumptions: first, that the realistic nucleation process *can* be modelled with the DFPE described in section 3.2. Second, for the GSD, that the $P(a)$ is given with Eqn.(3.12), which is derived from the monomer density (Eqn.(2.21)), independently of the DFPE model. In the case of the CZD, $P_z(a_z)$ which is sampled from the $P(a)$ through (3.18), includes an additional assumption that the neighbouring gaps are uncorrelated.

The non-mean field DFPE (3.19) includes the same assumptions, but not the mean field approximation, which makes it a more accurate model. However, it only makes for a small improvement (as seen on Figure 3.6). We will therefore almost exclusively focus on the simpler mean field model, test its consistency and its possible extension to 2d.

Chapter 4

Simulations and numerical methods

Some of the computational methods we use in this work are self-contained and explained within a single research chapter, and a few methods we use throughout the entire thesis. We shall describe the latter here, so that all of the subsequent research chapters can refer to the same explanation of a calculation (or simulation) method.

4.1 Monte Carlo procedure for obtaining gaps from a DFPE

To create a set of gaps of lengths x that satisfy the DFPE equation $x \triangleq a(1+x)$, we used a Monte Carlo procedure:

First define an array for $M = 10^6$ gap sizes $x(M)$ (the allowed values are real numbers with 9 decimal spaces). Set the first to one and the rest to zero ($x(1) = 1, x(2, ..., M) = 0$).
Make a loop with indices $i \in [2, M]$ and in it perform these two steps $M - 1$ times (from $i = 2$ to $i = M$):

1) Use the random number generator (built-in in the compiler, we use GNU Fortran (gfortran) and Intel's Fortran (ifort) compilers) to select one of the gap sizes by random:

we choose a gap index by random, j_{ran} and then define $x(j_{ran})$.

Built-in random number generators can give random real numbers between $y = 0$ and $y = 1$ (but not including 1), with the probability distribution $P(y) = 1$ (like in the Dickman case). To select a gap size (which is an element in a one-dimensional array with M indices), we need to select a random integer value for an index, so we convert a random real number into an integer. In the first step ($i = 2$) the algorithm can only choose $j_{ran} = 1$ (so $x(1)$ is the chosen gap size), but for $j = 3$ a random number from the interval $[0, 1)$ is mapped to integers 1 or 2 to give $j_{ran} = 1$ or $j_{ran} = 2$; in general the real random number in this step is always mapped onto a set of integers in the interval $[1, i - 1]$ with uniform density.

2) Use the random number generator to select a value for a and then redefine the second element (when $i = 2$) of the gaps array, $x(i) = x(2)$, as:

$$x(i) = a(1 + x(j_{ran})) \tag{4.1}$$

Since the first gap size was $x(1) = 1$, the gap size $x(j_{ran})$ used to redefine $x(2)$ in this step could have only been 1. In the next cycle ($i = 3$), after a random value for a has been randomly chosen, the third element of the array, $x(i) = x(3)$, is redefined as $x(i) = a(1+x(j_{ran}))$. The gap size $x(j_{ran})$ (randomly chosen in step 1) used to redefine $x(3)$ could have been (with equal probability) either 1 (if $j_{ran} = 1$ is chosen in step 1) or the previously updated value of $x(2)$ (if $j_{ran} = 2$).

Next, to incorporate the fact that nucleation fragments a gap into two new gaps with size proportions a and $1 - a$, redefine $x(j_{ran})$:

$$x(j_{ran}) \to (1 - a)(1 + x(j_{ran})). \tag{4.2}$$

This enforces the symmetry $a \leftrightarrow (1 - a)$.

As i increases, so does the number of available gaps to choose from ($j_{ran} \in [1, i - 1]$). This expanding array of 'active' gaps yields DFPE. A large array (following large number of steps) is needed for a good sample and it ensures the stochastic nature of DFPE. After a few steps the system completely forgets the initial conditions (the predetermined length of the first gap size $x(1) = 1$ and the zeroes of the rest). The code block for this procedure is in the Appendix B.

The above described procedure corresponds to the Dickman case. DFPE for the gap size distribution between islands is obtained in the same way, with slight modification that transforms the built-in $P(a) = 1$ of the random number generator into the desired $P(a) = N \cdot a^{\alpha}(1-a)^{\alpha}$, where N is the normalization constant. This is done in two steps:

1. choose a random value of a (call it a_x) and calculate the corresponding value of $P(a)$ (call it y).

2. choose another random number: $t \in [0, 1)$, and multiply it by P_{max} - the maximum possible value of the function $P(t)$ on the interval $[0, 1)$. This way, the interval $[0, 1)$ (from which the random number generator can draw) maps to the interval $[0, P_{max})$ (where the final, multiplied value of t lies).

Now if this $t \in [0, P_{max})$ is smaller than or equal to y from the first step, the value a_x is kept as a. If not, the two steps are repeated until such a t is found for which $t \leq y$. This way, the randomly chosen a is kept (for further use in the algorithm) with a probability $y = P(a)$.

A variant of this procedure is used in Chapter 9 to calculate the DFPEs for the capture zones in 2d.

Once the set of $M = 10^6$ gap sizes $x(M)$ is created, we calculate their size distribution $\phi(x)$ by creating histograms: we divide the x axis into equal intervals (bases of bins) and count the number of gap sizes that fall into each of them; this gives the height of bins. When normalised (each bin divided by the total area) these heights are the distribution $\phi(x)$.

Results of this MC procedure are shown on Figure 4.1 for the Dickman distribution, and for the GSD from DFPE with $\alpha = i+1$, $i = 0$ ($P(a) = 6a(1-a)$) on Figure 4.2.

To better understand the behaviour of the DFPE, for the Dickman case we investigated whether the large (small) gap sizes were created by small or large vales of a. To see the structure in the a vs. x plot, the gap sizes were grouped in intervals of length 0.5 (first interval $x \in [0, 0.5]$, second $x \in [0.5, 2]$ etc). The values of a that created these grouped gaps were located, and histograms for a corresponding to the intervals of x were created. On Figure 4.3, the distribution $P(a)$ that created the gaps of sizes $x \in [0, 0.5]$ is shown with yellow circles (visible on the left); the small-size gaps were created with small-size a. On the opposite end, the large-size gaps were created by large-size a; the distribution $P(a)$ responsible for $x \in [3, 3.5]$ is shown in black circles (zero for $a \in [0, 0.4]$ and then growing to the right). These two $P(a)$ have a pronounced peak, for the first distribution near $a = 0$ and for the second near $a = 1$, and are almost zero otherwise. The values of a that created the mid-size gaps (around $x \simeq 1$) have flatter and wider distributions, so the (averaged) sum of all these distributions is $P(a) = 1$.

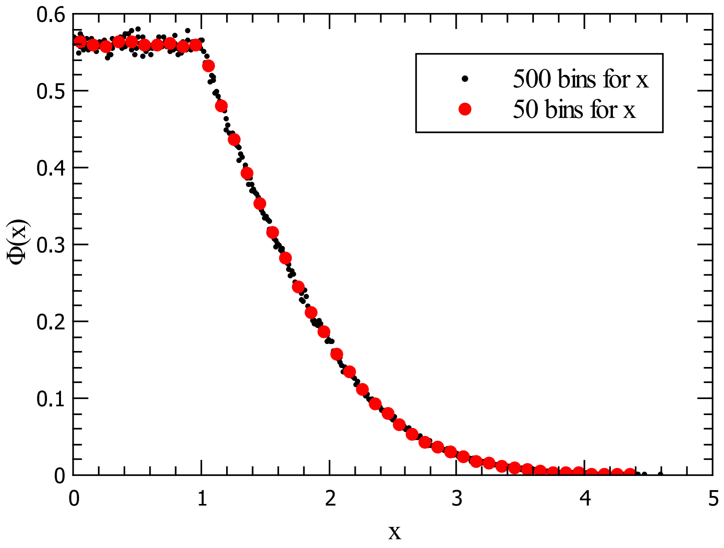

Figure 4.1: The Dickman distribution $\phi(x)$ from the MC procedure, with 50 and 500 bins used to obtain $\phi(x)$.

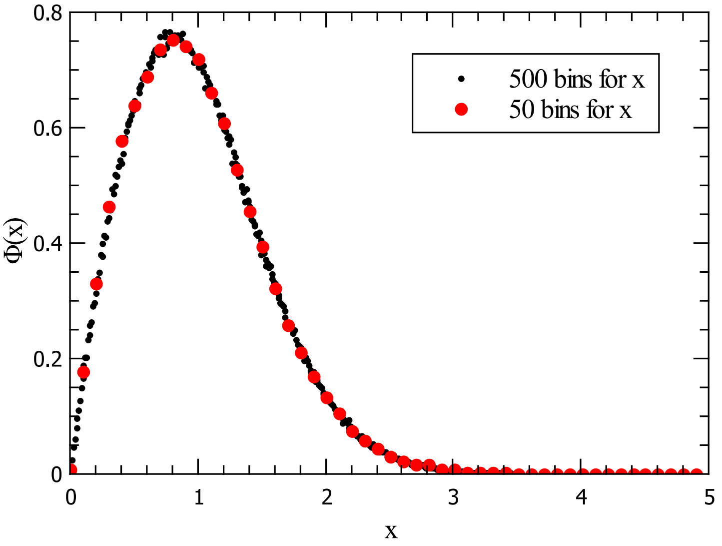

Figure 4.2: GSD $\phi(x)$ from the MC procedure, with $P(a) = 6a(1-a)$, obtained with 50 and 500 bins.

4.2 Numerical calculation of the integral equation

To numerically calculate the integral equation

$$\phi(x) = \int_0^{min(x,1)} \phi\left(\frac{x}{a} - 1\right) \frac{P(a)}{a} da, \tag{4.3}$$

we used an iterative scheme. The probability $P(a)$ can be set to the theoretical expectation:

$$P(a) = Na^{\alpha}(1-a)^{\alpha}, \tag{4.4}$$

where N is the normalizing constant, or to the values obtained from the kMC simulations.

Initial guess for $\phi(x)$ was a rectangular distribution:

$$\phi_0(x) = \begin{cases} 0.5, & x \in [0,2] \\ 0 & \text{elsewhere.} \end{cases}$$

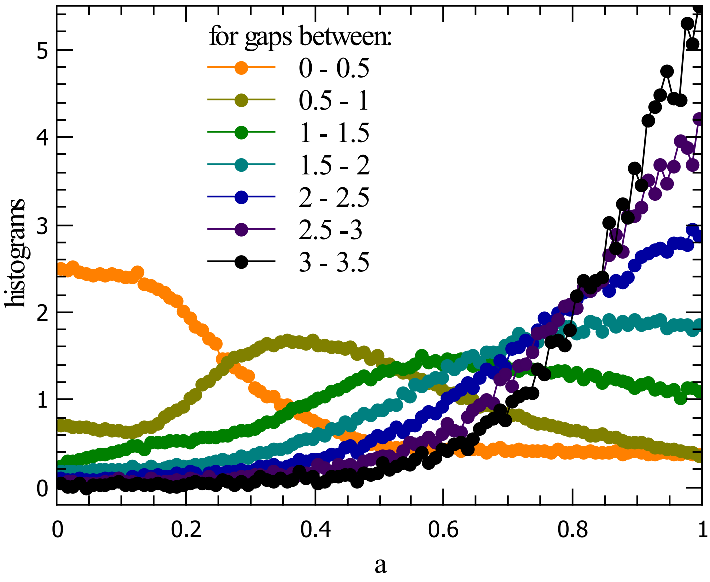

Figure 4.3: Distributions $P(a)$ that created gap sizes grouped in intervals from $x \in [0, 0.5]$ to $x \in [3, 3.5]$.

This was inserted on the right hand side of (4.3) to obtain $\phi_1(x)$, which was then inserted on the right hand side (4.3) to obtain $\phi_2(x)$, and so on. A distribution $\phi_{n+1}(x)$ that does not differ from the previous iteration $\phi_n(x)$ is the solution of (4.3) for the given $P(a)$. When using (4.4), after ten iterations we have $\phi_{10}(x) = \phi_{11}(x)$ up to the first three decimals, and later the routine was always run until the iterations were the same at least up to the first 5 decimals.

Figure 4.4 shows the convergence of the IE solution for the $\alpha = 2$ case.

4.3 Full kMC simulations: one-dimensional lattice

We use a point island model, in which islands occupy a single site on the lattice with sizes recorded and incremented as they capture new monomers. In this model the islands don't coalesce even at large coverage θ, which allows us to collect much more data than we could in the extended island model (where the scaling would quickly break down).

The simulation starts with an empty lattice and loops diffusion steps a certain

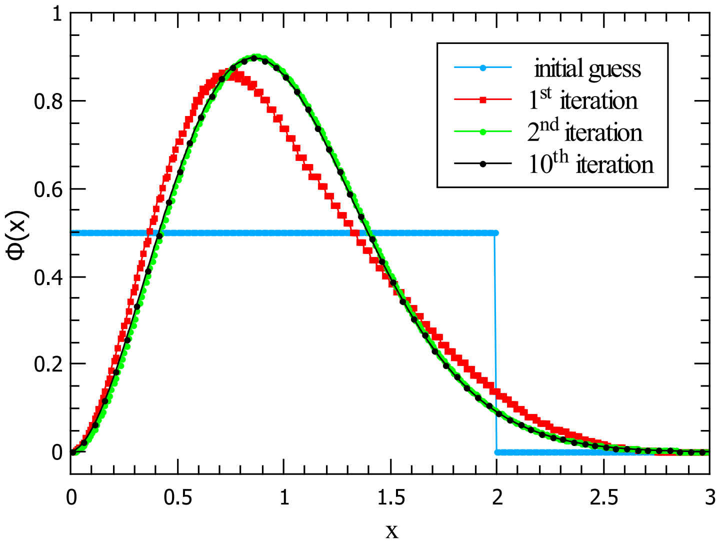

Figure 4.4: Iterations of Equation (4.3), for $\alpha = 2$.

number of times (determined by the desired ratio R) between deposition steps. In a diffusion step, we select a random free monomer on the lattice and move it to either the left or right adjacent lattice site with equal probability. In a deposition step a monomer is placed on a randomly chosen lattice site.

If a monomer arrives (or is deposited) to a position adjacent to a stable island, it will be absorbed: we delete it from the list of free monomers and increment the island's size by one (the island is still occupying a single site on the lattice).

If the monomer arrives next to (or on top of) another cluster of monomers, and the total number of monomers has exceeded i, an island nucleates: the monomers are deleted from the list of free monomers and the new island's size and position is recorded.

We use periodic boundary conditions: if a monomer finds itself on one end of the lattice, it can diffuse to the site on the opposite end.

Schematics of the processes in a point island simulation with $i = 1$ are shown in Figure 4.5. In our kinetic Monte Carlo simulation, we start off with an initially empty lattice with $N = 10^6$ sites and diffusion to deposition ratio $R = 10^7$. We allow monomers to hop on average 20 times before the next deposition event ($R = 0.5 \cdot 20 \cdot N$, where the factor 0.5 reflects the fact that a monomer will, on average, hop to the left

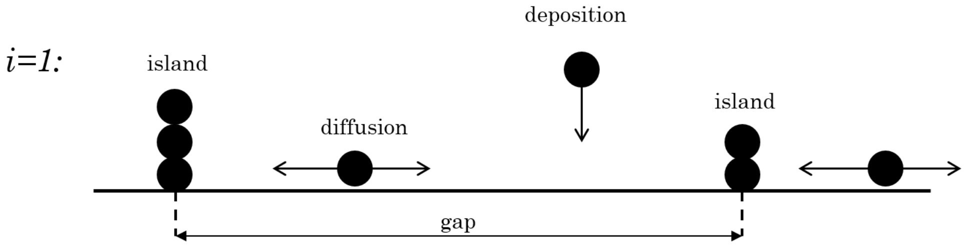

Figure 4.5: Illustration of processes involved in the 1d point island kMC simulation. The sizes of the islands are here indicated by the monomer stacks (for illustration only).

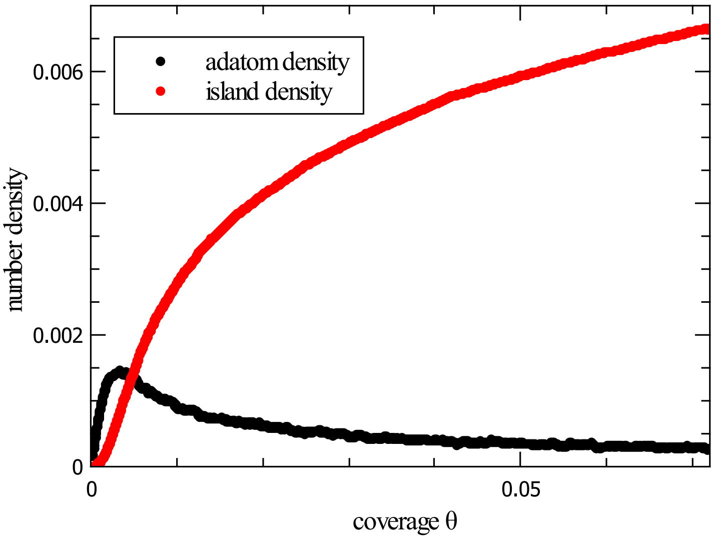

Figure 4.6: Number densities of free monomers and islands vs. coverage θ, for $i = 1$.

(or right) in half of its diffusion moves). In total we deposit $n = 10^6$ monomers to get $\theta = 100\%$ coverage on a lattice with $N = 10^6$ sites (however, not all of the n monomers will be attached, typically at the end of a simulation there is up to a hundred free monomers in $i = 1$ case, and more for higher i). Figure 4.6 shows the number densities of free monomers and number densities of islands as a function of coverage θ in the $i = 1$ case.

In the $i = 0$ case we set the probability that a monomer will permanently stick to the site onto which it hopped or was deposited to be $p = 10^{-7}$.

To get GSDs and CZDs we use outputs at desired coverage θ and average the data over 100 runs. Every time a new island nucleates, we record its position and use that data to create $P_{kMC}(a)$ (built as a histogram). We also record the size of the gap in which the new island nucleation occurs, and the gap's size rank. GSD results for $i = 1$ are shown on Figure 4.7, with true gap sizes, measured in lattice spacings, and on Figure 4.8 with gap sizes scaled to the average gap size at a given coverage.

For the remainder of the thesis, whenever dealing with a one-dimensional substrate, we will be using the GSDs and CZDs described here; with $\theta = 100\%$ coverage (point island model), $R = 10^7$, results averaged over 100 runs (the example GSD case plotted red in Figure 4.8).

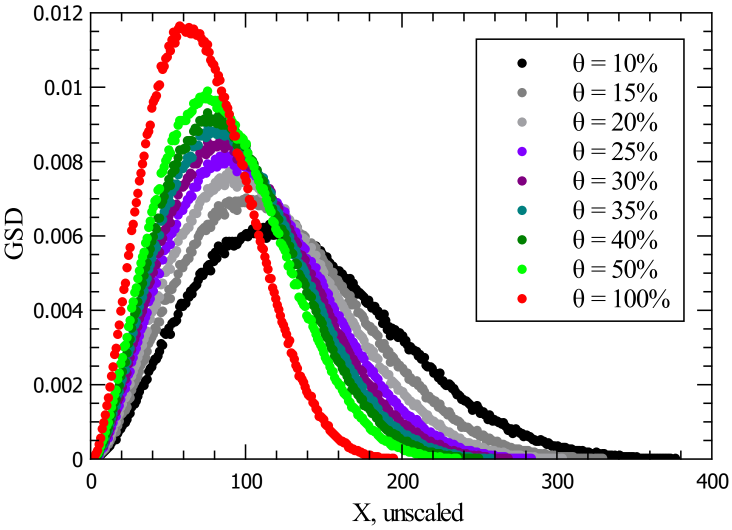

Figure 4.7: GSD for $i = 1$, unscaled, at various coverages θ.

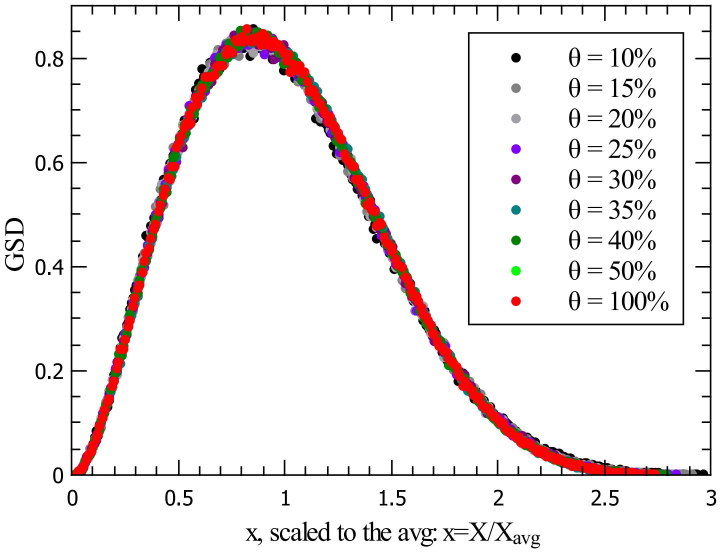

Figure 4.8: GSD for $i = 1$, with gap sizes scaled to the average, at various coverages θ.

Chapter 5

Inverse problem and the Tikhonov regularisation method

The DFPE model for the GSD and CZD can be used to calculate the relevant probability distribution P from a known GSD and CZD (in our case, kMC obtained).

In his chapter, we set out to do this because it will not only be a test for the models self - consistency (ultimately we will compare the calculated P with the one we directly measure during kMC simulations), but also it has implications for situations where P cannot be measured. Developing a good strategy of calculating P from measured size distributions could later be used on experimental data for 1d substrates (for example, nucleation along a step edge).

The Tikhonov regularisation method is a textbook method of solving the inverse problem we are concerned with; we will use in this chapter.

The chapter is structured as follows: we will first cover some of the theoretical basics behind the inverse problem we are dealing with in Section 5.1, before proceeding to explain the theory behind the Tikhonov method in Section 5.2. We will then look into the technical aspects of the inverse problem associated with the gaps, and compare the solutions from two different software algorithms in Sections 5.3 and 5.4. With a chosen algorithm, we will finally solve the inverse problem for the gaps and attempt a few modifications to the standard choice of method parameters, in Sections 5.5 - 5.7.

Lastly, we will solve the inverse problem for the capture zones in Section 5.8, with the approach that worked best for the gaps.

5.1 Inverse problem

We aim to solve the inverse problem of finding $P(a)$ for a given $\phi(x)$ (obtained from kMC) from the integral equation

$$\phi(x) = \int_0^{min(x,1)} \phi\left(\frac{x}{a} - 1\right) \frac{P(a)}{a} da. \tag{5.1}$$

The integral equation (5.1) belongs to the class of (linear) Fredholm integral equations of the first kind, which are ill-posed. An ill-posed problem, in the sense of Hadamard, has a solution that is not unique or it isn't stable, i.e. it doesn't depend continuously on the data (a small perturbation in the data can cause arbitrarily large perturbations in the solution) [73, p.4].

Fredholm equations of the first kind have a general form

$$g(x) = \int_A^B k(x,a) f(a) da, \tag{5.2}$$

where g is the unknown and k is called the kernel function.

It is important to notice that our integral equation (5.1), when compared with the Fredholm equation (5.2), has an additional complication: the function $\phi(x)$ on the left hand side also appears as the kernel function $\phi(x,a)$ under the integral on the right hand side. So, in an inverse problem of finding $P(a)$, any noise in the input data $\phi(x)$ will also propagate in the kernel. Because of that, this is not a standard inverse problem and, as far as we know, there are no recipes for dealing with this complication. In lack of another strategy, we will proceed to treat the integral equation (5.1) as a standard Fredholm equation.

The Fredholm integral equation (5.2) can be written in an operator form:

$$\mathcal{K}f = g, \tag{5.3}$$

where $\mathcal{K}$ is a linear integral operator, $\mathcal{K} : U \to V$, and U, V are subspaces of some normed spaces X, Y. Applying the kernel $\mathcal{K}$ to the function f on the right hand side will in general smooth it, so inversion becomes difficult and the solution is very sensitive to small changes or noise in the input g: a small error in input can result in an arbitrarily large error in the solution.

Ill-posedness of equation (5.3) is a consequence of both the properties of the operator $\mathcal{K} : U \to V$ and the subspaces it works on; a formal mathematical discussion of this can be found in Appendix C. The key result is that $\mathcal{K}$ cannot be inverted to get a good (stable) solution because U is infinite-dimensional; this is a fundamental property of the equation and cannot be avoided. The consequence is this seemingly counter - intuitive behaviour: under normal circumstances, increasing the number of points on the mesh grid (on which the equation is solved numerically) gives better solutions. But for ill-posed equations, the solutions become less reliable as the number of grid points is increased.

5.1.1 Discrete ill - posed problem

When equation $\mathcal{K}f = g$ is discretized with some quadrature rule:

$$\int_a^b \Phi(x)dx \approx \sum_{i=1}^{N} w_i \Phi_i(x), \tag{5.4}$$

it is a matrix equation $Kf = g$ with $K \in \mathbb{R}^{m \times n}$, $f \in \mathbb{R}^n$ and $g \in \mathbb{R}^m$ (or, more generally, in $\mathbb{C}$). Ill-posedness of the continuous operator then translates into ill-posedness of the matrix K, which can be quantified with its condition number; a measure of how much the output changes for a small input change. The matrix condition number grows as the number of grid points on which K is evaluated grows; the discrete $K_{m\times n}$ operating on a finite, n-dimensional space becomes closer to the continuous operator $\mathcal{K}$ operating on an infinite dimensional space.

Generally, with a given matrix equation $Ax = y$, the condition number of the matrix A is defined as the maximum ratio of the relative error in x, δx, and the relative error in y, δy. When y has an attached error δy, the solution x' to the matrix equation is:

$$x' = A^{-1}(y + \delta y) = A^{-1}y + A^{-1}\delta y = x + A^{-1}\delta y, \tag{5.5}$$

which causes an error in x':

$$\delta x = x' - x = A^{-1}\delta y. \tag{5.6}$$

If A is very small, then A^{-1} will be very large and amplify δx. The condition number of A is now defined as:

$$\text{cond}(A) = \max\left(\frac{\|\delta x\|}{\|x\|} / \frac{\|\delta y\|}{\|y\|}\right) = \max\left(\frac{\|\delta x\| \cdot \|y\|}{\|\delta y\| \cdot \|x\|}\right) = \max\left(\frac{\|A^{-1}\delta y\| \cdot \|Ax\|}{\|\delta y\| \cdot \|x\|}\right), \tag{5.7}$$

and because

$$\frac{\|A^{-1}\delta y\| \cdot \|Ax\|}{\|\delta y\| \cdot \|x\|} \leq \frac{\|A^{-1}\| \cdot \|\delta y\| \cdot \|A\| \cdot \|x\|}{\|\delta y\| \cdot \|x\|} = \|A^{-1}\| \cdot \|A\| \tag{5.8}$$

we have:

$$\text{cond}(A) = \|A^{-1}\| \cdot \|A\|. \tag{5.9}$$

Here, $\|A\|$ denotes a norm of A (*any* norm); it is possible to define the condition number of A relative to any norm, although in practise one would most often use the 2-norm ($\|\cdot\|_2$). The 2-norm of a matrix $A_{m\times n}$ is defined as the square root of the sum of the absolute squares of its elements,

$$\|A\|_2 = \sqrt{\sum_{i=1}^{m} \sum_{j=1}^{n} |A_{ij}|^2} \tag{5.10}$$

and $\|x\|_2 = \sqrt{\sum_{i=1}^{n} |x_i|^2}$ for a vector x.

From (5.9), it is clear that the condition number is equal to or greater than one: $\|A^{-1}\| \cdot \|A\| \geq \|A^{-1}A\| = \|I\| = 1$.

If the condition number is too large (more precisely, if its reciprocal is close to the machine's floating point precision [73, p.53]), a matrix is ill conditioned (if the condition number is infinite, it is singular). Well conditioned matrices have condition number close to one.

Singular value decomposition

Singular values σ_i of a matrix $A_{m \times n}$, $m \leq n$, are the positive square roots $\sigma_i = \sqrt{\lambda_i} \geq 0$ of the associated Gram matrix $A^T A$. The corresponding eigenvectors of $A^T A$ are called the singular vectors of A.

Matrix $A^T A$ is symmetric, so it has a property that its eigenvectors v_i form an orthonormal basis. Then, singular value decomposition can be constructed like this: let $u_i = A v_i / \sigma_i$ and then construct 3 matrices:

matrix U has u_i as column vectors,

matrix V has v_i as column vectors,

matrix Σ has σ_i on the diagonal and zeros elsewhere.

Then $U\Sigma$ is a matrix with Av_i as column vectors and when multiplied with V^T, $U\Sigma V^T$ gives $Av_i v_j^T$ but since the eigenvectors v_i are orthonormal the result is A.

Formally, singular value decomposition (SVD) of the real matrix A is defined as [73, p.19]:

$$A = U\Sigma V^T = \sum_{i=1}^{n} u_i \sigma_i v_i^T, \tag{5.11}$$

where $U = (u_1, ..., u_n) \in \mathbb{R}^{m\times n}$, $\Sigma = diag(\sigma_1, ..., \sigma_n) \in \mathbb{R}^{n\times n}$ and $V = (v_1, ..., v_n) \in \mathbb{R}^{n\times n}$. Matrices U and V have orthonormal columns and V, since it is a square matrix, has orthonormal rows too (so it is an orthogonal matrix):

$$U^T U = I, \quad V^T V = I, \quad V V^T = I. \tag{5.12}$$

From the definition (5.11), we have $A^T A = V\Sigma^T U^T U \Sigma V^T = V\Sigma^2 V^T$ and $AA^T = U\Sigma V^T V \Sigma^T U^T = U\Sigma^2 U^T$ so the link of SVD to eigendecomposition of the symmetric matrices $A^T A$ and AA^T is clear; the left singular vectors of A, u_i, are eigenvectors of the matrix AA^T and the right singular vectors of A, v_i, are eigenvectors of $A^T A$.

A very useful additional property of the SVD is that it constructs an orthonormal basis for the nullspace and the range of the matrix.

If there is a matrix equation $Ax = y$ where $x \in X, y \in Y$ are vectors, then the matrix A maps vectors x to vectors y; the range (or image) of A is a subset of Y comprised of these y's. Rank of the matrix A is defined as the dimension of the space spanned by its columns (or, equivalently, rows), so it is just a dimension of the subspace of Y onto which A has mapped elements from X (dimension of the range), $r(A) = \dim(Im(A))$. A necessary (but not sufficient) condition for a matrix $A_{m\times n}$ to be invertible is that it is of full rank ($r(A) = \min(m, n)$). If a matrix doesn't have full rank, it is said to be rank deficient, and it will map some of the elements from X not to Y but to zero; the subspace of X for which $Ax = 0$ is the nullspace or the kernel of a matrix A. (In terms of the definition of an ill-posed equation from Appendix C, the matrix A here is not bijective.) Dimension of the nullspace plus rank are equal to the full rank of A (the rank and nullity theorem, $\dim(Ker(A_{m\times n})) + \dim(Im(A_{m\times n})) = \min(m, n)$).

Columns of V corresponding to singular values equal to zero are an orthonormal basis for the nullspace, and columns of U that correspond to singular values not equal to zero are an orthonormal basis for the range [6, p.53]. So the rank of A can be calculated as the number of non-zero singular values.

The determinant of A is equal to the product of all of its singular values, so if any of the singular values is zero the determinant is zero - rank deficient matrices are singular. When the 2-norm ($\|\cdot\|_2$) is used, the definition of the condition number of a matrix (5.9) reduces to the ratio of the largest to the smallest singular value in its singular value decomposition:

$$cond(A) = \frac{\sigma_{max}(A)}{\sigma_{min}(A)}, \tag{5.13}$$

so it is clear that singular matrices have infinite condition number.

If A is not full rank, equation $Ax = y$ is a rank deficient problem. Rank deficient problems are characterised by matrices with a well defined gap between the large and the small singular values that cluster around zero [73, p.2]. Then some of the rows (or columns) of A are a linear combination of the others.

Numerical rank of a matrix is equal to the number of its linearly independent columns (or rows), and it can also be calculated as the number of positive singular values. Then, when errors are present (i.e. measurement, approximation or rounding errors) it can happen that otherwise linearly independent columns (or distinct positive singular values) become (almost or completely) linearly dependant (in other words, some or all singular values become indistinguishable). Because of that, a strict definition of numerical rank takes into account a certain tolerance interval ϵ within which the columns are linearly independent. When working with singular values, the numerical rank only makes sense if there is a well – determined gap between the singular values (otherwise it is ill-defined) [73, p.46]:

$$\sigma_r > \epsilon \geq \sigma_{r+1}. \tag{5.14}$$

Discretized Fredholm integral equations typically belong to the class of discrete ill-posed problems, where there is no particular gap in the singular value spectrum and the singular values decrease gradually towards zero. Because there is no gap between the singular values, there is no clear notion of numerical rank [73, p.2].

From the SVD definition (5.11) we have the following relations:

$$Av_i = \sigma_i u_i, \quad \|Av_i\|_2 = \sigma_i, \tag{5.15}$$

$$A^T u_i = \sigma_i v_i, \quad \|A^T u_i\|_2 = \sigma_i. \tag{5.16}$$

From this, it is clear that if some singular values σ_i are small enough, the matrix A is nearly rank deficient and the corresponding v_i are the numerical nullvectors of A, and the u_i of A^T [73, p.21].

5.2 Tikhonov regularization: theoretical background

The matrix equation $Kf = g$ discussed in the previous chapter, is in most practical applications contaminated with noise in the input g: (typically, g represents measured data so it has an error)

$$g = g_0 + e, \tag{5.17}$$

where g_0 is the true, error free input and e is noise. Ideally, the bound for the error norm is known:

$$\|e\|_2 \leq \delta_e. \tag{5.18}$$

The goal (since the error free solution f_0 isn't available) is to solve the 'perturbed' equation $Kf = g$. The Tikhonov regularisation method replaces this problem - the problem of minimizing

$$\min_f \|Kf - g\|_2^2 \tag{5.19}$$

with the following:

$$\min_f \{\|Kf - g\|_2^2 + \lambda \|Lf\|_2^2\}. \tag{5.20}$$

Here $\lambda > 0$ is the regularisation parameter and L the regularisation operator, typically the identity operator, a discrete approximation of some derivation operator, or a diagonal weighting matrix [73, p.12] [74]. The regularisation parameter determines how much weight is given to minimizing $\|Lf\|_2$ relative to the residual norm $\|Kf - g\|_2$. For a chosen value of λ, the standard form of a matrix equation associated to (5.20) to be solved is

$$(K^T K + \lambda L^T L)f = K^T g. \tag{5.21}$$

If the matrix K is ill - conditioned, with an ill-determined rank, the addition of the regularisation operator L should make the problem well posed and [73, p.22] [75]:

$$\mathcal{N}(K) \cap \mathcal{N}(L) = \{0\} \tag{5.22}$$

(where $\mathcal{N}(K)$ is the nullspace of K; discussed in the previous section), so then Equation (5.21) has a unique solution f_λ for all λ. These solutions are less sensitive to error than the solutions of the original problem.

We can write the equation $Kf = g$ in terms of the singular value decomposition (SVD) [73, p.19]: $\sum_i u_i \sigma_i (v_i^T f) = g$. From this we have:

$$\sum_i v_i^T f = \sum_i \frac{u_i^T g}{\sigma_i}. \tag{5.23}$$

Then the solution f only exists if $u_i^T g$ (the expansion coefficients of g with respect to the orthonormal u_i) decrease faster than σ_i. Matrix K can be of full rank, but numerically rank deficient if some of the singular values σ_i are small enough. The small σ_i can give an arbitrarily large norm $\|f\|_2^2 = \sum (u_i^T g / \sigma_i)^2$ unless g is in the range of K, that is unless $|u_i^T g| < \sigma_i$ (singular vectors u_i span the range of K).

The Picard condition: If g satisfies:

$$\sum_i \left| \frac{u_i^T g}{\sigma_i} \right|^2 < \infty, \quad \sigma_i \neq 0, \tag{5.24}$$

then the solution of $Kf = g$ (or $\min_f \|Kf - g\|_2$) is:

$$f = \sum_i \frac{u_i^T g}{\sigma_i} v_i. \tag{5.25}$$

The Picard condition is always satisfied for a finite-dimensional problem, unless noise is present; then it is very unlikely that it will be satisfied [73, p.49].

5.2.1 Generalized SVD

In the minimization (5.20) we have a pair of matrices, (K, L) for which we can define generalized singular value decomposition (GSVD). Assuming that (5.22) holds and that L is full -rank, for $K \in \mathbb{R}^{m\times n}$ and $L \in \mathbb{R}^{p\times n}$ the GSVD is defined as [73, p.22]:

$$K = \tilde{U} \begin{pmatrix} \tilde{\Sigma}_p & 0 \\ 0 & I_{n-p} \end{pmatrix} X^{-1}, \quad L = \tilde{V} \begin{pmatrix} M_p & 0 \end{pmatrix} X^{-1}, \tag{5.26}$$

where $\tilde{U} \in \mathbb{R}^{m\times n}$ and $\tilde{V} \in \mathbb{R}^{p\times p}$ are orthonormal (so $\tilde{U}^T\tilde{U} = I_n$ and $\tilde{V}^T\tilde{V} = I_p$) and $X \in \mathbb{R}^{n\times n}$ is a non singular matrix with columns that are K^TK orthogonal, that is, they satisfy the following:

$$X^T K X = \begin{pmatrix} \tilde{\Sigma}_p & 0 \\ 0 & I_{n-p} \end{pmatrix}, \quad X^T L^T L X = \begin{pmatrix} M_p & 0 \\ 0 & 0 \end{pmatrix}. \tag{5.27}$$

The matrices $\tilde{\Sigma}_p$ and M_p are diagonal,

$$\tilde{\Sigma}_p = diag(\tilde{\sigma}_i), \quad M_p = diag(\mu_i) \tag{5.28}$$

and their elements are

$$0 \leq \tilde{\sigma}_1 \leq ... \leq \tilde{\sigma}_p \leq 1, \quad 1 \geq \mu_1 \geq ... \geq \mu_p > 0, \tag{5.29}$$

and they satisfy

$$\tilde{\sigma}_i^2 + \mu_i^2 = 1. \tag{5.30}$$

The generalized singular values γ_i of the pair (K, L) are:

$$\gamma_i = \frac{\tilde{\sigma}_i}{\mu_i} > 0, \quad i = 1, ..., p. \tag{5.31}$$

Matrices $\tilde{U}, \tilde{\Sigma}, \tilde{V}$ of the GSVD of (K, L) are in general different from the matrices U, Σ, V of the SVD of K. The are identical if the regularisation operator L is chosen to be I_n. Then $X^{-1} = M^{-1}\tilde{V}$ and $K = \tilde{U}(\tilde{\Sigma}M^{-1})\tilde{V}^T$, so then the generalized singular values of (K, L), γ_i, are related to the ordinary singular values of K, σ_i, by: $\sigma_i = \gamma_{n-i+1}$. The solution to Equation (5.21), equivalent to (5.25), in terms of GSVD, is [76]:

$$f_\lambda = \sum_{i=1}^{p} \frac{\gamma_i^2}{\gamma_i^2 + \lambda^2} \frac{\tilde{u}_i^T g}{\tilde{\sigma}_i} x_i + \sum_{i=p+1}^{n} (\tilde{u}_i^T g) x_i. \tag{5.32}$$

Here $\gamma_i^2/(\gamma_i^2 + \lambda^2)$ are the filter factors that filter out the contributions to f that come from the terms with small singular values γ_i. Since the small singular values were the main generators of large oscillations of f in non-regularized case (5.25), solutions of the regularized problem will now be less sensitive to perturbation (i.e. error in input g).

5.2.2 Choosing the regularisation parameter

If the error (5.18) is known and if only the right hand side of $Kf = g$ is perturbed, a popular and simple method of choosing the regularisation parameter λ is given by the so-called discrepancy principle [76]: λ that gives the residual norm equal to the upper norm of the errors, $\|Kf_\lambda - g\|_2 = \delta_e$. If, additionally, error in K is also present (and known), this expands into the generalised discrepancy principle. This method however will (especially when errors in K are present) typically oversmooth the real solution [76].

If the error is unknown, a frequently used method is the generalized cross - validation [77] [73, p.187], where λ is chosen as the one that minimizes the GCV function:

$$GCV = \frac{\|Kf_\lambda - g\|_2^2}{(Tr(I - KK^{-1}))^2}. \tag{5.33}$$

Another option is the (relatively new) L-curve criterion.

Since minimization (5.20) involves a trade - off between minimizing the residual norm $\|Kf - g\|_2$ (agreement between data and the solution) and minimizing the semi-norm (the regularisation term's norm) $\|Lf\|_2$ (smoothness and stability of the solution), it is convenient to plot those two against each other. This is the L - curve:

$$\textit{L-curve} = \left\{ (\chi(\|Kf_\lambda - g\|_2^2), \chi(\|Lf_\lambda\|_2^2) : \lambda > 0 \right\}, \tag{5.34}$$

where χ is a monotonically increasing function, most often $\chi(x) = x$, $\chi(x) = \log(x)$ or $\chi(x) = \sqrt{x}$ [78] (we will use $\chi(x) = x$ for our L - curve plots). The L - curve, as a function of λ, always [76] has a shape of the letter L (hence the name). With these standard choices of χ, $\|Kf_\lambda - g\|_2^2$ is an increasing function of λ and $\|Lf_\lambda\|_2^2$ a decreasing one.

All of the solutions of (5.20) are above the L - curve or lie on it, that is, for a given f_λ:

$$\chi(\|Kf_\lambda - g\|_2^2) \leq \chi(\|Kf - g\|_2^2), \quad \forall f \in \mathbb{R}^n \quad \text{such that } \chi(\|Lf\|_2^2) \leq \chi(\|Lf_\lambda\|_2^2) \tag{5.35}$$

(a proof is provided in [78]).

The L-curve has a corner where the solution f_λ changes from being dominated by regularisation errors (oversmoothing) to being dominated by the errors of the right hand side g. The value of λ on the corner is therefore taken to be the optimal.

5.3 Calculation of $P_\lambda(a)$ from the GSD

When solving our inverse problem; that is, when solving the IE:

$$\phi(x) = \int_0^{min(x,1)} \phi\left(\frac{x}{a} - 1\right) \frac{P(a)}{a} da \tag{5.36}$$

for P where ϕ is the known, we use the zeroth order regularisation. Then the matrix equation to be solved is

$$(K^T K + \lambda I^T I)P = K^T \phi, \tag{5.37}$$

where the matrix K is given as a discretized integral $\int \phi(\frac{x}{a} - 1)\frac{da}{a}$ where ϕ is taken as the height of the bin used to create the GSD as a histogram from the kMC data:

$$K = \sum_{j=1}^{100} \phi_j(\frac{x_j}{a_j} - 1)\frac{da}{a_j} \tag{5.38}$$

All of the GSDs were originally created with 500 bins, and the size of the interval they cover varies for different i (because each is scaled to the average and the average gap size differ) - for example, for $i = 1$ it is $[0, 6.9321]$, giving $dx = 6.9321/500 = 0.0138$. This interval and the number of points x_j is then rescaled to a 100 points where the expression (5.38) is evaluated, $x_j \in [0, 6.9321/100]$ giving $dx = 0.069321$.

The interval for the variable a, $[0, 1]$, is also divided into 100 points where a_j is evaluated, so $da = 0.01$ and $K_{100\times100}$.

With this K and a chosen parameter λ, matrices $(K^T K + \lambda I^T I)$ and $K^T\phi$ (where ϕ is again taken to be the bin heights ϕ_j that created GSD from kMC data) are written as a product of a lower and upper triangular matrix (LU decomposition) using routines from the "Numerical recipes" handbook [6], allowing the solution P of (5.37) to be simply calculated; the matrix equation when using LU decomposition comes down to the final stage of the Gaussian elimination method.

5.3.1 Regularity of the problem matrix K for $i = 1$ case

In this section, we illustrate the regularity issues of the K matrix on the example dataset: $i = 1$ case of the $KP = \phi$ inverse problem, where the input GSD is averaged from a 100 runs of kMC simulations.

MATLAB calculates the rank of the matrix $K_{100\times 100}$ to be 100, so K is full rank. It also reports that all of the singular values are nonzero (it calculates rank as the number of nonzero singular values), but when they are written out in a format which rounds up a real number to 15 decimal places, many of them turn out to be zero. When ordered by size from the largest to the smallest, after the 62nd all of the singular values are the same and equal to $2.9 \cdot 10^{-17}$ (this is still larger than the smallest single precision floating point number, which in MATLAB is of the order 10^{-38}). So this is a nearly rank – deficient matrix (or numerical-rank deficient).

Also (and because of this), the determinant of K is 0, both calculated as a product of all of the singular values (where the rounding causes it) and from the LU decomposition ($det(K) = det(L) \cdot det(U)$, the determinants are: $det(L) = 1, det(U) = 0$ and all of the elements on the diagonal of U are 0).

The regularised matrix $(K^T K + \lambda I^T I)$ with $\lambda = 0.001$ is full rank and has singular values that are, after the 36th by size, all equal to 0.001 (singular values previously equal to or close to zero are increased by the value of λ). The determinant of this matrix, calculated as a product of nonzero singular values, is 4.7972×10^{-288} (smallest double precision floating point is of the order 10^{-308}), which is equal to the determinant that is calculated from LU decomposition, $det(L) = -1$ and $det(U) = -4.7972 \times 10^{-288}$.

The first 50 singular values (in decreasing order from the largest) of the regularised matrix are shown on the Figure 5.1, along with the singular values of the original matrix K; visually, after the 20th value they are hard to distinguish (the regularised are lifted only by 0.001).

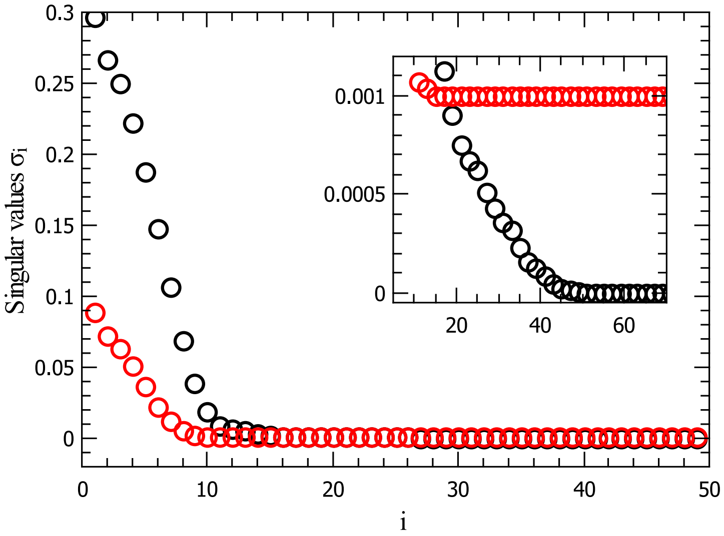

Figure 5.1: First 50 singular values for the matrix K given by (5.38), shown in black circles. Red circles are the singular values of the regularised matrix $(K^TK + \lambda I^TI)$, with $\lambda = 0.001$. The inset (zoom-in) shows the elevation of these singular values above the singular values of the original matrix.

5.4 "Numerical recipes" routine vs. MATLAB

A Tikhonov regularisation package is available in MATLAB (under the name "regtools" [79]). It calculates the L - curve, finds the point of maximum curvature and uses its corresponding λ as the optimal parameter. It makes use of singular value decomposition of the equations' matrices (as opposed to the LU decomposition algorithm from the "Numerical recipes" - Ref. [6]).

MATLAB's resulting L-curve for $i = 1$ (again, the kMC GSD as the input ϕ) is shown on Figure 5.2, along the L-curve we obtained by using the "Numerical recipes" algorithm. The "Numerical recipes" handbook suggests using $\lambda = Tr(K^TK)/Tr(I^TI)$ as an initial guess [6, p.802], which then one increases and decreases to map out the L - curve. For the case $i = 1$, this initial guess is equal to $\lambda = 3.46 \cdot 10^{-3}$.

The L - curves from the two different algorithms correspond. However, MATLAB's corner - locating algorithm fails to find the real corner (the best λ), and instead just picks the furthest right point. The resulting $P_\lambda(a)$, for this λ and the next two corner values ($\lambda = 5.445 \cdot 10^{-7}$ and 0.012376) from the Figure 5.2, are shown on Figure 5.3 and the left panel of Figure 5.4. All three cases of $P_\lambda(a)$ give the (almost) same $\phi_\lambda(x)$, shown on the right panel of Figure 5.4. It is clear that, in this case, we need to look for a solution in the furthest right corner, with $\lambda \approx 0.01$ (and larger, since the solution for $\lambda = 0.012376$ on the left panel of Figure 5.4 still needs to be smoothed out).

To find inverse problem solutions in the rest of the thesis, we will proceeded with the "Numerical recipes" [6] algorithm.

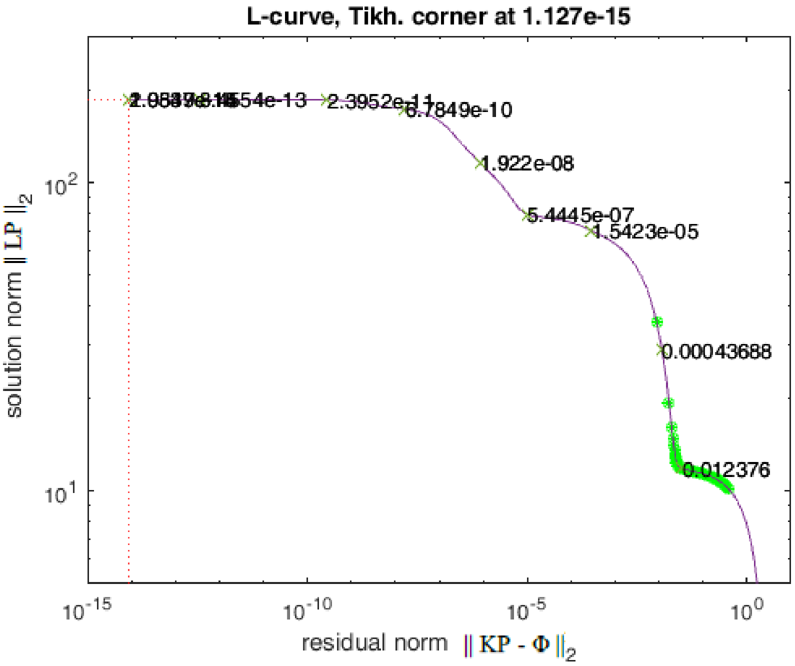

Figure 5.2: MATLAB's "regtool" package result for $i = 1$. Corners of the curve are marked on the graph, with the corresponding values of λ. The optimal λ is identified as the Tikhonov corner, $\lambda = 1.127 \cdot 10^{-15}$ (also visually marked with dotted lines in the left right corner). The L - curve that was calculated with an algorithm from "Numerical recipes" [6] is shown with green dots.

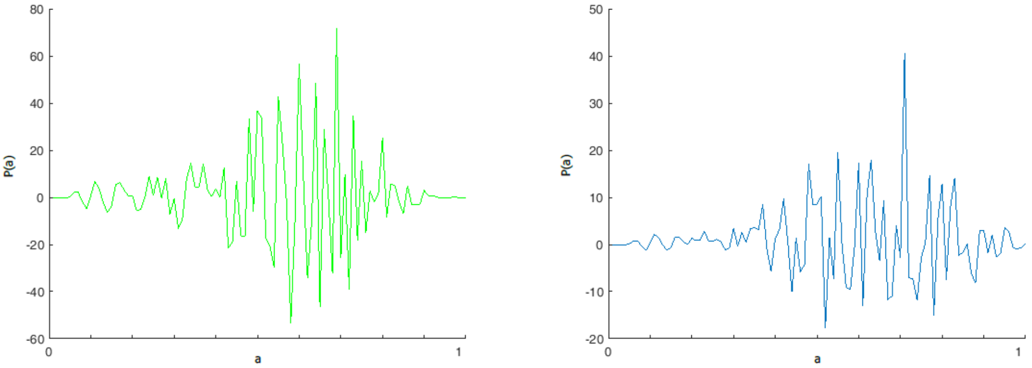

Figure 5.3: MATLAB's solutions: Left: $P_\lambda(a)$ with the "regtool" package suggested $\lambda = 1.127 \cdot 10^{-15}$.
Right: $P_\lambda(a)$ from the first corner; $\lambda = 5.445 \cdot 10^{-7}$.

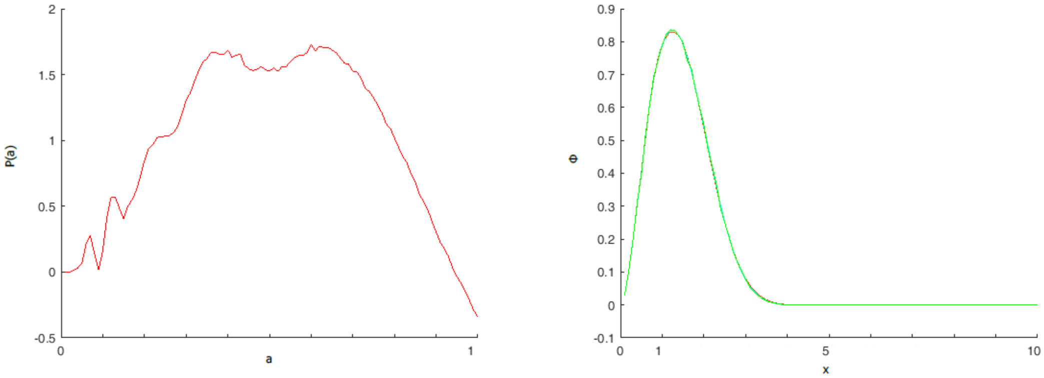

Figure 5.4: MATLAB's solutions: Left: $P_\lambda(a)$ with the second corner; $\lambda = 0.012376$.
Right: Resulting $\phi_\lambda(x)$ for all three cases; $\lambda = 1.127 \cdot 10^{-15}$, $\lambda = 5.445 \cdot 10^{-7}$ and $\lambda = 0.012376$.

5.5 Regularisation with the identity operator

Before we proceed to calculate $P_\lambda(a)$ from the kMC obtained GSD for the four cases of i, we can test the "Numerical recipes" algorithm on a known problem: we use $P(a) = 6a(1-a)$ (corresponding to the diffusion model $P(a)$ for $i = 0$ $(\alpha = i + 1)$) to solve the IE (5.36), then invert the resulting $\phi(x)$ to see if we can get the exact P back. The L - curve for this problem is shown on Figure 5.5. There is no clear choice of a corner point; as we look closer (or stretch the scale), the corner becomes bow - shaped, and its 'sharpness' depends on the number of points we use to plot the L - curve graph. There is a level of subjectivity in choosing the value of λ; so every time we look for the P_λ solution, we plot a couple of solutions with values of λ visually in the corner of the L - curve. We then choose the solution that is smoothest while its error isn't too large (at the very least, the corresponding ϕ_λ shouldn't visibly differ from the input ϕ).

On Figure 5.5, we choose four values of λ (marked with green dots) for which we show the solutions P_λ in Figure 5.7. When these solutions are used again to solve the IE (5.36) to obtain ϕ_λ, they overlap each other and the original ϕ perfectly, as shown on Figure 5.6.

The errors listed are the square mean errors ($err = \|KP - \phi\|_2^2$, read off the L - curve plot) - the same as the ones used in the Fourier reconstruction method in the previous chapter (Eqn. (6.17)).

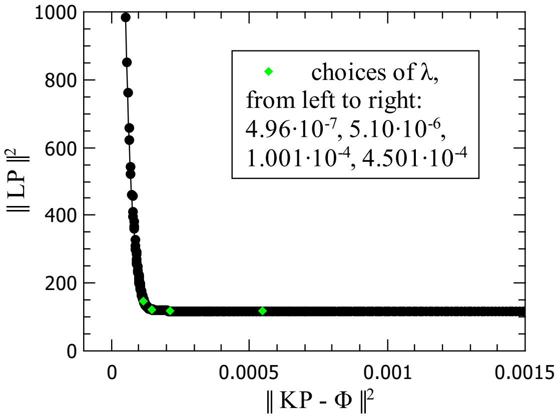

Figure 5.5: L - curve for the test case of the inverse problem: inversion of $\phi(x)$ (Eqn. (5.36)) which was obtained with $P(a) = 6a(1-a)$. Four chosen values of λ are marked green; the corresponding solutions are shown on Figure 5.6.

As can be seen from the Figure 5.7, the first two λ choices are still too small - the solutions P_λ oscillate around the true $P(a)$. The third choice, $\lambda = 0.0001$ would be the optimal choice. The fourth choice of λ is already leaving the corner area; the corresponding solution P_λ is showing small signs of oversmoothing around $a = 0.8 - 1$ (here, P_λ is a straight line).

Since the Tikhonov regularisation relies only on minimizing the $\|\cdot\|_2$ norm;

$$\|P\|_2 = \int_0^1 |P(a)|^2 da, \tag{5.39}$$

it does nothing to preserve symmetry, positivity or the $\|\cdot\|_1$ norm:

$$\|P\|_1 = \int_0^1 |P(a)| da. \tag{5.40}$$

The best solution on Figure 5.7 (dark blue) is positive for all x (unlike the solution with the smallest λ; plotted red), and it is roughly symmetric, with $\|P_\lambda\|_1 \simeq 0.99990$. The loss of symmetry, positivity and the norm will continue to follow us through all the particular cases of the inverse problem. However, from the behaviour of the chosen few solutions P_λ with λ values from the corner of the L - curve, it is clear that the best solutions tend to be (the most) symmetric, positive and with $\|P_\lambda\|_1$ close to 1.

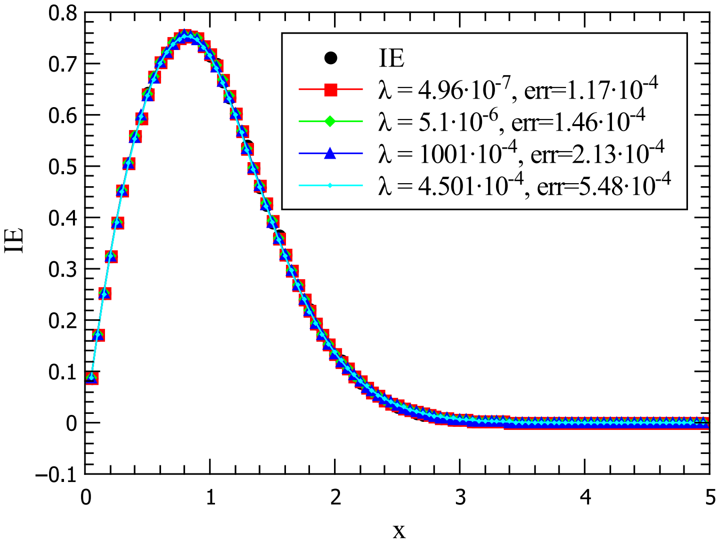

Figure 5.6: The input ϕ (calculated from $P(a) = 6a(1-a)$) in black, and the inverse problem solutions $\phi_\lambda(x)$ for all cases of λ.

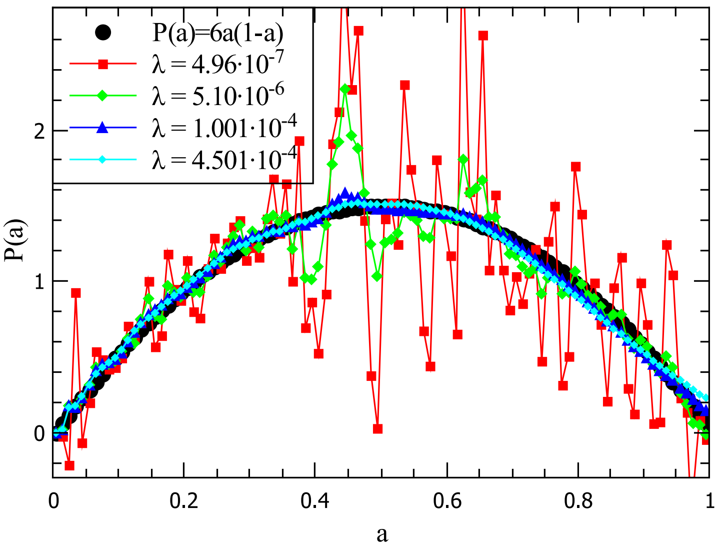

Figure 5.7: The inverse problem solutions $P_\lambda(a)$ for four choices of λ, plotted on top of the original $P(a) = 6a(1-a)$ (in black).

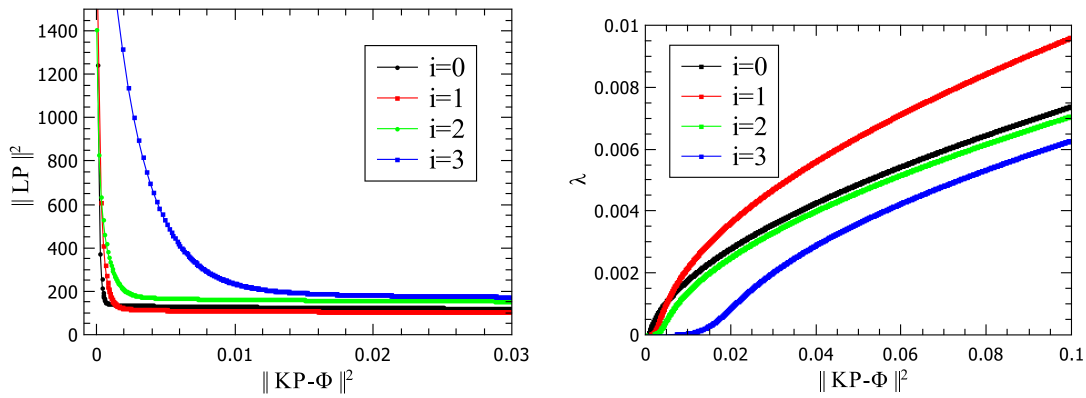

Figure 5.8: Left: L - curve for the $i = 0, 1, 2$ and 3 case of the inverse problem of finding P_λ from the kMC obtained GSD.
Right: λ vs. error $\|KP - \phi_\lambda\|_2^2$.

5.5.1 $P_\lambda(a)$ results for the kMC obtained GSD

L - curves for the inverse problem of calculating $P_\lambda(a)$ from the kMC obtained GSD (in Eqn. (5.37) we set ϕ to $\phi = \phi_{kMC}$) are shown on the left panel of Figure 5.8. The curves for $i = 1, 2$ and 3 (and, more notably, their corner regions) each in turn increase their the smallest possible error and regularisation term norm as the corners move away from the origin for increasing i. The reason for this is that, as i increases, so do the noise levels in the kMC data. This trend in the L - curves graphs shows us that, for higher i, we cannot hope to obtain as good a solution: a larger 'amount' of regularisation is needed yet we are still left with a larger error between the kMC GSD and ϕ_λ.

The regularisation parameter λ increases from left to right on the L - curve plots (it grows with the error $\|KP - \phi_{kMC}\|_2^2$); the right panel of Figure 5.8 shows how fast it grows with the error.

Figures 5.9 and 5.18 show these L - curves separately, with the chosen values of λ marked green. We plot the P_λ for these λ values on Figures 5.11, 5.13, 5.15 and 5.17 (for $i = 1, 2, 3$ and 0 case, respectively). We also show the model diffusion and deposition case of $P(a) = Na^\alpha(1-a)^\alpha$ (N being the normalization constant); these are plotted in light and dark blue on all of the graphs. Their corresponding IE (5.36) solutions are

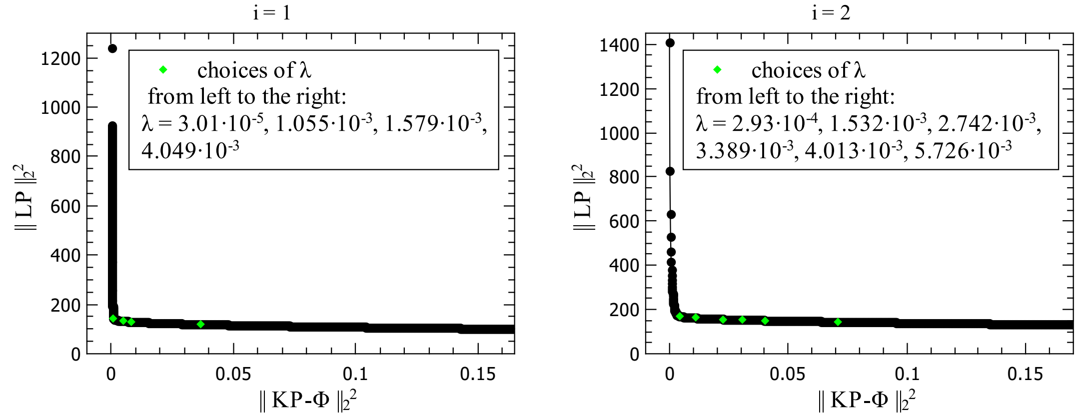

Figure 5.9: Left: L - curve for the $i = 1$ case, with chosen λ points (green).
Right: L - curve for the $i = 2$ case, with chosen λ points (green).

again plotted light and dark blue, in Figures 5.10, 5.12, 5.14 and 5.16. These figures also show the kMC obtained GSD (used as the input ϕ in Eqn. (5.37)). When the solutions P_λ are integrated again according to the IE (5.36), we get the shown ϕ_λ.

In all of the graphs the best solutions are plotted green; they are chosen as the ones having as small a λ as they can before the error becomes too large (the ϕ_λ graph visibly slides below the kMC GSD) and the $\|\cdot\|_1$ norm drops towards 0.95 (the norms $\|\cdot\|_1$, listed in the legends, decrease as λ increases). For the $i = 2$ and 3 case the best solutions plunge below 0 in a small region near $a = 1$, so they couldn't be renormalized. This is why we left the solutions as they were, un - normalized, in all of the cases of i.

In Chapter 7, we compare the best solutions P_λ with the kMC results and the Fourier reconstructed solutions P_F from the previous chapter.

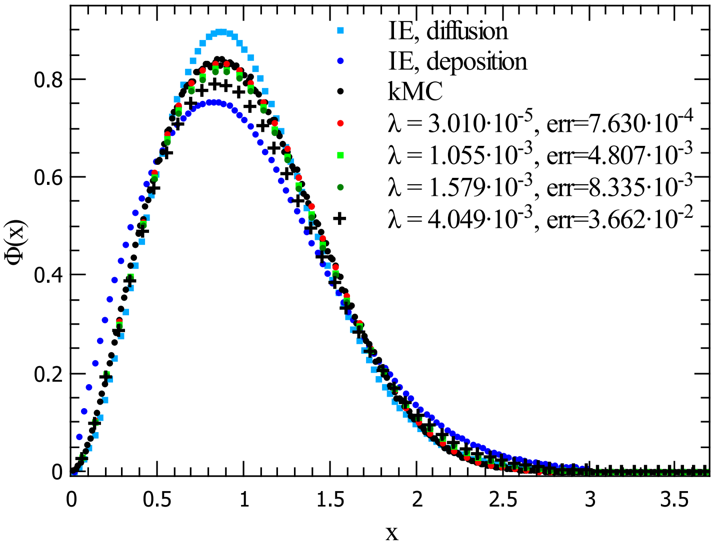

Figure 5.10: $i = 1$ case: the kMC GSD (black circles) used to calculate P_λ and the resulting ϕ_λ, shown with the diffusion and deposition case of the DFPE model (light and dark blue).

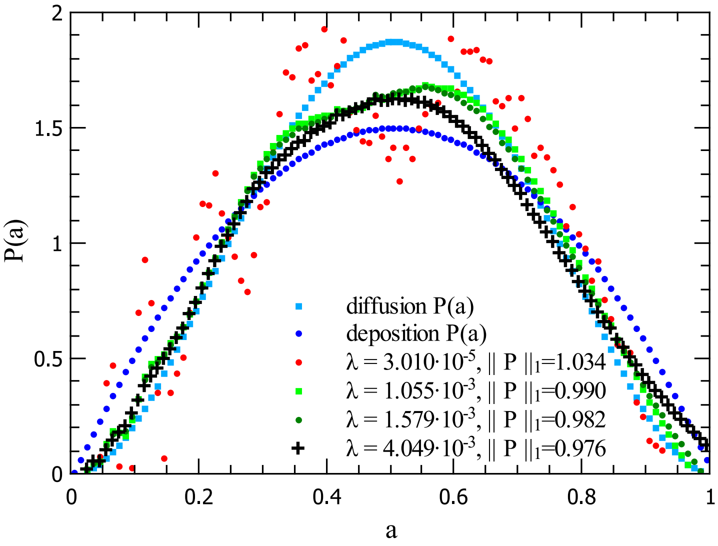

Figure 5.11: $i = 1$ case: solutions P_λ for the choices of λ marked green on the L - curve (Figure 5.9, left panel), shown with the diffusion and deposition case of the model $P(a)$ (light and dark blue).

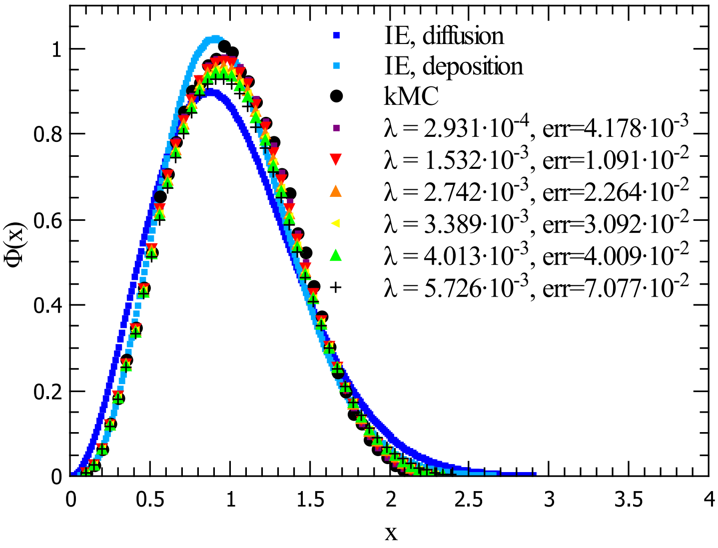

Figure 5.12: $i = 2$ case: the kMC GSD (black circles) used to calculate P_λ and the resulting ϕ_λ, shown with the diffusion and deposition case of the DFPE model (light and dark blue).

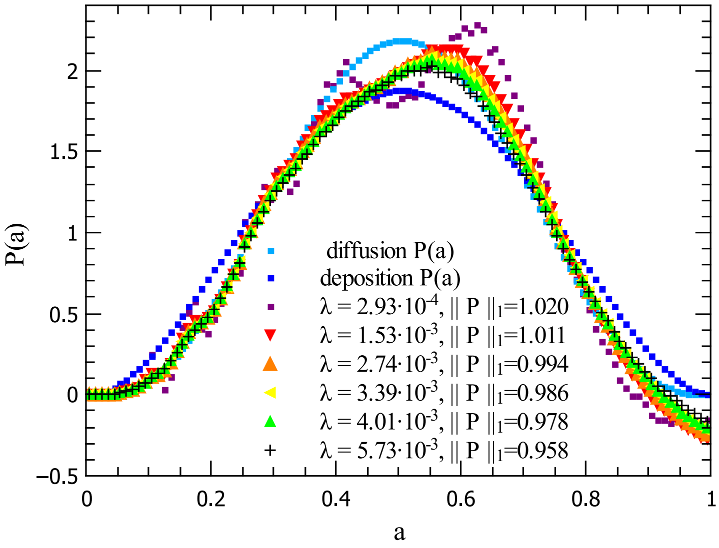

Figure 5.13: $i = 2$ case: solutions P_λ for the choices of λ marked green on the L - curve (Figure 5.9, right panel), shown with the diffusion and deposition case of the model $P(a)$ (light and dark blue).

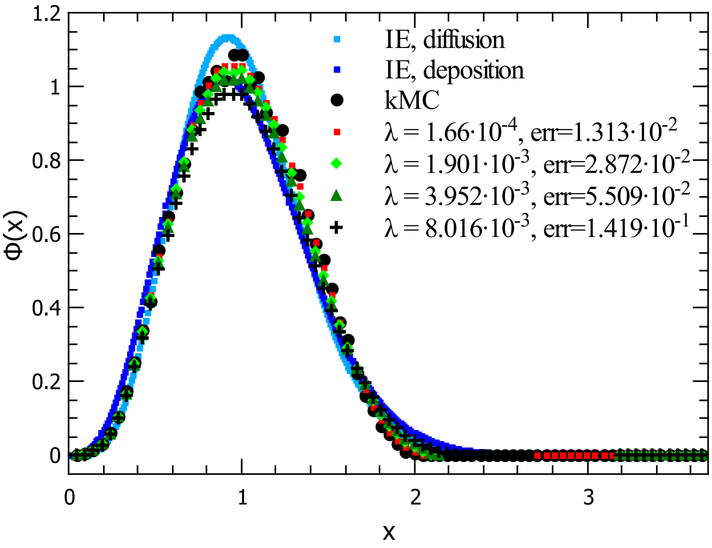

Figure 5.14: $i = 3$ case: the kMC GSD (black circles) used to calculate P_λ and the resulting ϕ_λ, shown with the diffusion and deposition case of the DFPE model (light and dark blue).

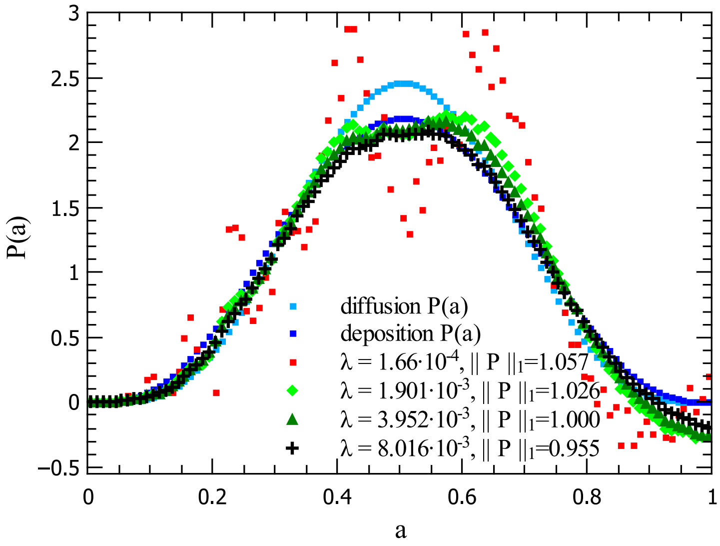

Figure 5.15: $i = 3$ case: solutions P_λ for the choices of λ marked green on the L - curve (Figure 5.18, left panel), shown with the diffusion and deposition case of the model $P(a)$ (light and dark blue).

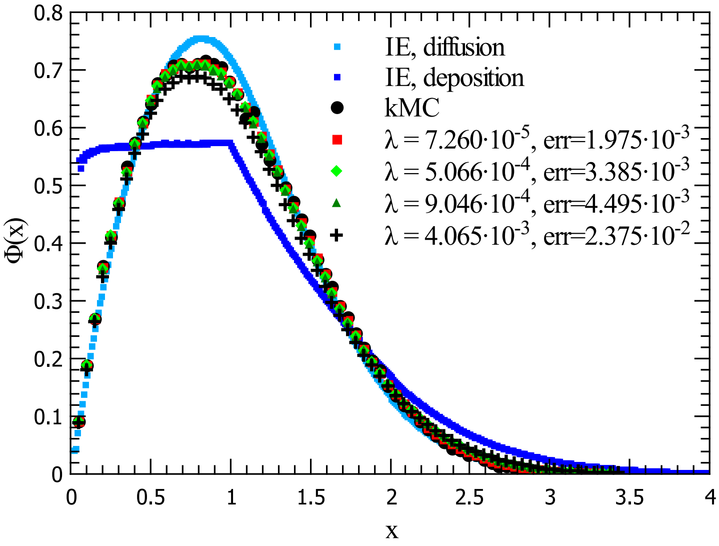

Figure 5.16: $i = 0$ case: the kMC GSD (black circles) used to calculate P_λ and the resulting ϕ_λ, shown with the diffusion and deposition case of the DFPE model (light and dark blue).

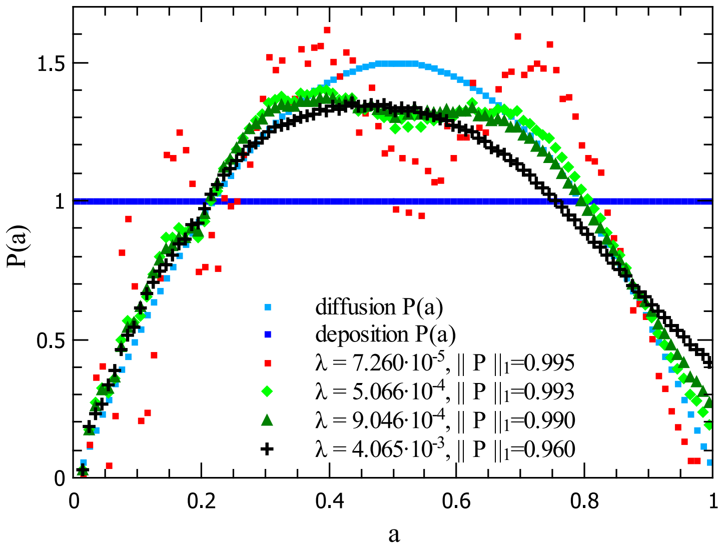

Figure 5.17: $i = 0$ case: solutions P_λ for the choices of λ marked green on the L - curve (Figure 5.18, right panel), shown with the diffusion and deposition case of the model $P(a)$ (light and dark blue).

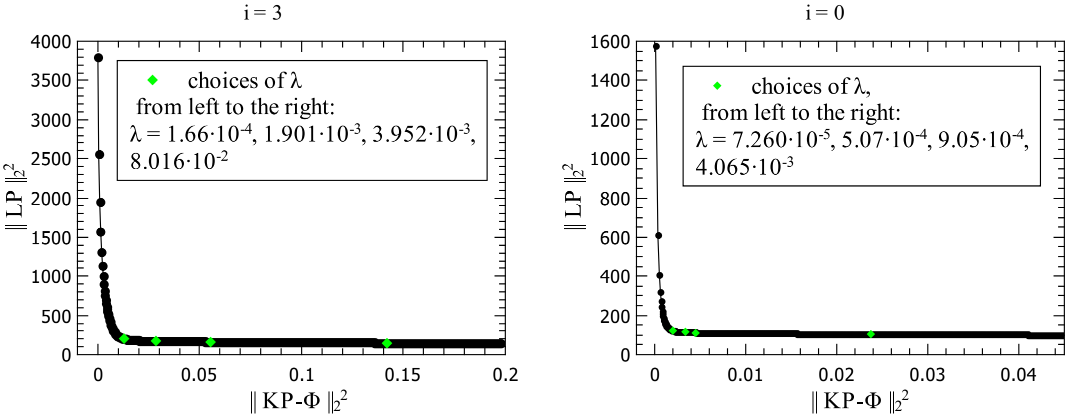

Figure 5.18: Left: L - curve for the $i = 3$ case, with chosen λ points (green). Right: L - curve for the $i = 0$ case, with chosen λ points (green).

5.6 The second differential operator as the regularisation operator

Instead of the identity operator, a differential operator can be used as a regularisation operator. Since we want to damp the oscillations of P_λ, the most logical choice is the second differential operator. Its corresponding matrix is also listed in the "Numerical recipes" handbook [6]. Apart from changing the operator L, everything in the procedure is the same as before.

After some testing, we didn't find the differential operator to be a valuable improvement for our case: it gave similar results as the simpler choice of the identity operator. We show here the case $i = 3$, with kMC GSD as the input ϕ. Figure 5.19 (left panel) shows the L - curve with marked choices of λ; the last one (furthest to the right) gives a reasonably good solution. It is comparable to the $\lambda = 0.0019$ choice (second λ from the left in Figure 5.18, left panel) that we used with the identity operator in the previous section; both result in an error of the order $\|KP_\lambda - \phi_{kMC}\|_2^2 \sim 0.01$ and their P_λ graphs similar.

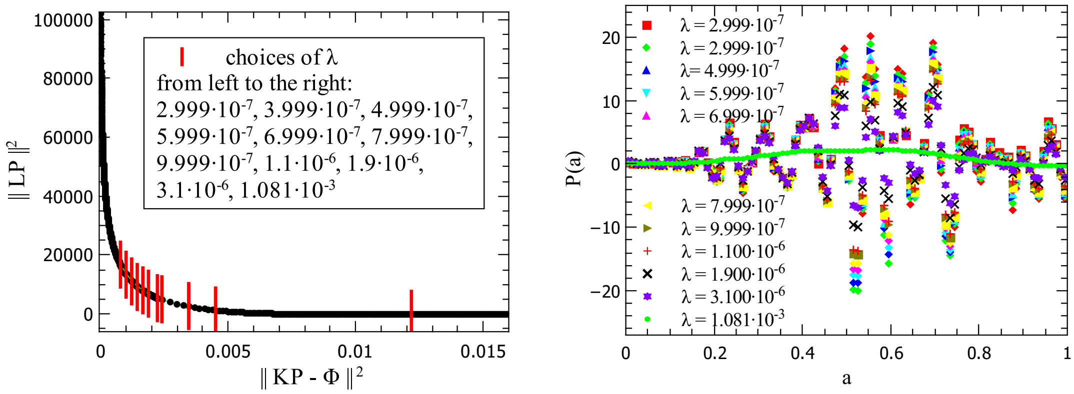

Figure 5.19: Left: L - curve for the $i = 3$ case of the inverse problem with the second differential operator and kMC GSD as an input ϕ in Eqn. (5.37).
Right: The solutions $P_\lambda(a)$ for the chosen values of λ.

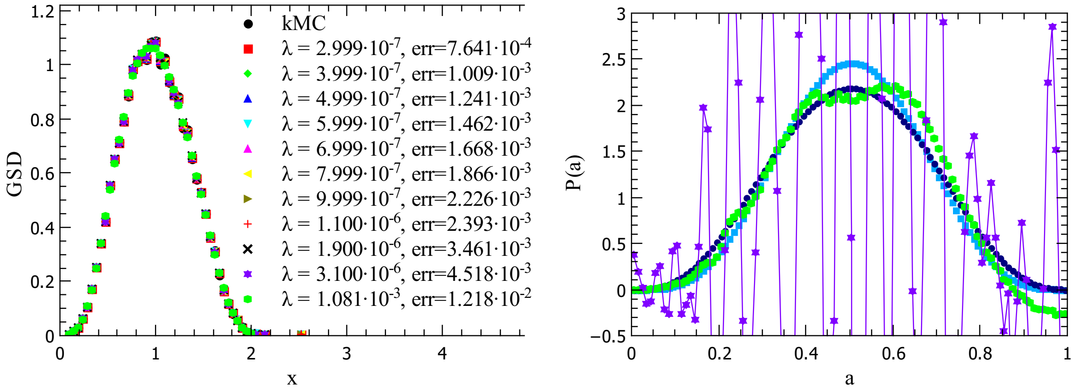

Figure 5.20: Left: The original GSD and the ϕ_λ for the chosen values of λ.
Right: Three solutions $P_\lambda(a)$; for the 3 largest values of λ from Figure 5.19 (zoom - in).

5.7 Symmetrization operator

Because we know that P needs to be symmetric, we can modify the regularisation procedure for our problem by adding a term that penalizes asymmetry. We replace the minimization problem:

$$\|KP - \phi\|_2^2 + \lambda\|LP\|_2^2 \tag{5.41}$$

with the minimization problem:

$$\|KP - \phi\|_2^2 + \lambda\|LP\|_2^2 + \lambda_S\|P(a) - P(1-a)\|_2^2. \tag{5.42}$$

The added term amplifies the asymmetry $P(a) - P(1-a)$ when λ_S increases, so minimizing for P means finding the solution P for which $P(a) - P(1-a) \simeq 0$.

This translates to the matrix equation (analagous to Eqn. (5.21)):

$$(K^T K + \lambda L^T L + \lambda_S S)P = K^T \phi \tag{5.43}$$

where P is a one-column matrix, $P = (P_1, P_2, ..., P_n)$, and S is a matrix such that

$$SP = \sum_{i=1}^{n}(P_i - P_{n-i+1}) \tag{5.44}$$

(in our case, $n = 100$). The matrix S that forces the opposite elements of P to cancel out as in (5.44) is a square matrix with zeroes everywhere except on the diagonals:

$$S = \begin{pmatrix} 1 & 0 & 0 & \dots & 0 & 0 & -1 \\ 0 & 1 & 0 & \dots & 0 & -1 & 0 \\ 0 & 0 & 1 & \dots & -1 & 0 & 0 \\ \vdots & \vdots & \vdots & \ddots & \vdots & \vdots & \vdots \\ 0 & 0 & -1 & \dots & 1 & 0 & 0 \\ 0 & -1 & 0 & \dots & 0 & 1 & 0 \\ -1 & 0 & 0 & \dots & 0 & 0 & 1 \end{pmatrix} \tag{5.45}$$

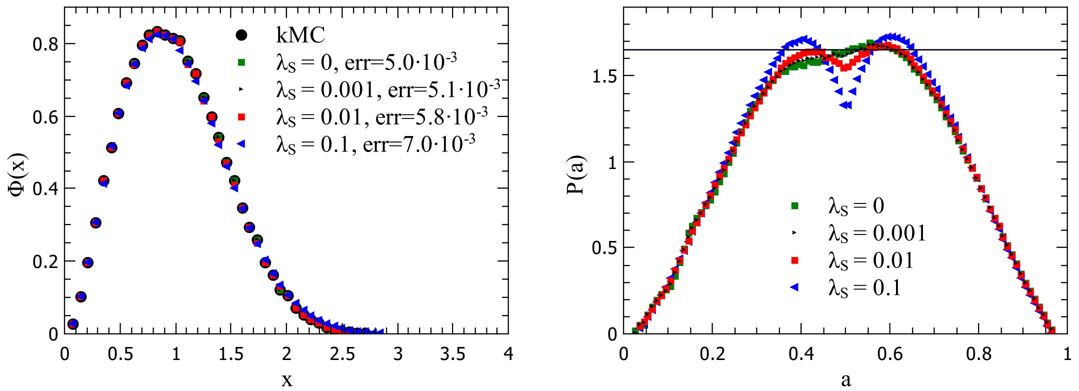

Figure 5.21: Left: the kMC GSD for $i = 1$ case (black circles) used to calculate $P_{\lambda,S}$ from Eqn. (5.43) with $\lambda = 0.001$, and the resulting $\phi_{\lambda,S}$.
Right: Solutions $P_{\lambda,S}$ with $\lambda = 0.001$ and varying λ_S.

With our $P_{1\times100}$ we then get $SP = (P_1 - P_{100}) + (P_2 - P_{99}) + ... + (P_{99} - P_2) + (P_{100} - P_1)$.

We solved Eqn. (5.43) for the $i = 1$ case and kMC GSD as an input ϕ. With the identity operator as the identity operator, $L = I$, we took the value of λ to be fixed at $\lambda = 0.001$. This is the value that gives a good solution to the original problem $(K^T K + \lambda I^T T)P = \phi$ (in the previous section, Figure 5.10 shows the best solutions as the ones with $\lambda = 0.001055$ and $\lambda = 0.001579$). With a fixed λ, we tried a few solutions for different λ_S; the results are shown on the right panel of Figure 5.21. The straight black line is drawn as a visual aid. It is easy to see, relative to the line, that the third solution ($\lambda_S = 0.01$, plotted red) still isn't symmetric, but it already starts to assume the M - shape (drops at $a = 0.5$). With higher λ_S the solutions become symmetric but the M - shape deformation also becomes more prominent.

Clearly, we cannot simply enforce symmetry on the best solution we found by just strengthening the symmetrization term while keeping λ fixed. Equation (5.43) would require its version of the L - curve plotted in a 3-dimensional coordinate system, where we would find the optimal (λ, λ_S) point; equivalent of the old L - curve corner.

Since this would extend the workload significantly, while it is still not clear how (if even possible with the equation form like (5.43)) we could enforce positivity, we abandoned this search.

5.8 Calculation of $P_{z,\lambda}(a_z)$ from the kMC CZD

Here we apply the same methodology to find the inverse problem solution of the DFPE for capture zones, rather than gaps.

Finding $P_{z,\lambda}$ from the IE:

$$\phi_z(z) = \int_0^{min(z,1)} \phi_z\left(\frac{z}{a_z} - 1\right) \frac{P_z(a_z)}{a_z} da_z, \tag{5.46}$$

where ϕ_z is the known CZD, translates into solving the matrix equation:

$$(K_z^T K_z + \lambda L^T L) P_z = K_z^T \phi_z, \tag{5.47}$$

with the matrix K_z calculated as the discretized integral $\int \phi_z(\frac{z}{a_z} - 1)\frac{da_z}{a_z}$ and again the discrete values of ϕ_z are taken to be the heights of the bins used to create the CZD as histograms of the kMC data averaged from a 100 runs ($\theta = 100\%$).

In light of the previous sections, we used the identity operator (zeroth order regularisation); $L = I$ and chose as the best solutions those from the corner region of the L - curve, which were smooth without having their $\phi_{z,\lambda}$ visually differ from kMC CZD (too large error), and with a $\|\cdot\|_1$ norm as close to 1 as possible without sacrificing the smoothness of the solution.

Qualitatively, the behaviour of the solutions (as we test λ from smaller to higher value) is the same as with the kMC GSD in Section 5.5.1. We show the L - curves with chosen values of λ on Figures 5.22 and 5.23. The corresponding solutions $P_{z,kMC}$ are shown in Figures 5.25, 5.27, 5.29 and 5.31 for $i = 1, 2, 3$ and 0 case, respectively. Figures 5.24, 5.26, 5.28 and 5.30 show the corresponding $\phi_{z,\lambda}$.

We use the same color coding as with the kMC GSD graphs: the best solutions $P_{z,kMC}$ are plotted green, input kMC CZD is black and the diffusion and deposition theoretical models are light and dark blue (where the model $P_z(a_z)$ is sampled from the corresponding GSD's $P(a) = Na^\alpha(1 - a)^\alpha$).

Again the best solutions for $i = 2, 3$ have a few negative points, around $a_z = 0.8$. In Chapter 7 we will again plot the best solutions $P_{z,\lambda}$ (against the Fourier reconstructed

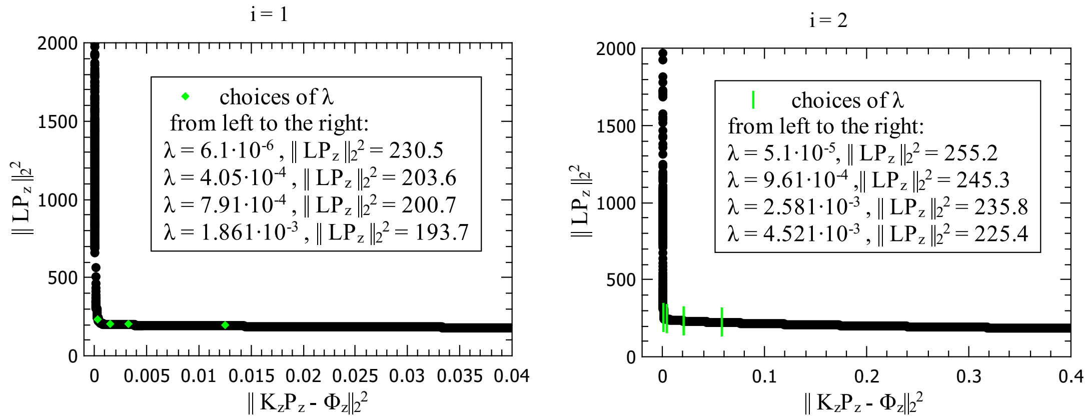

Figure 5.22: Left: L - curve for the $i = 1$ CZD case, with chosen λ points (green). Right: L - curve for the $i = 2$ CZD case, with chosen λ points (green).

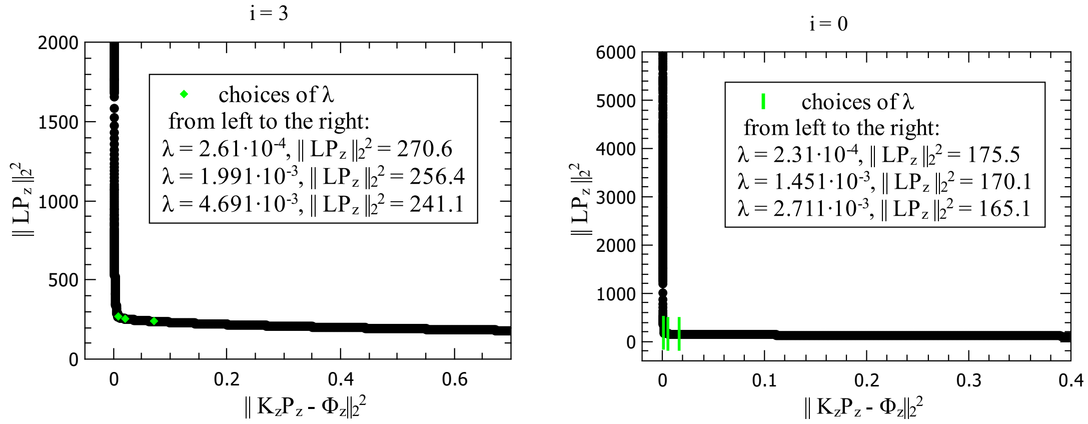

Figure 5.23: Left: L - curve for the $i = 3$ case, with chosen λ points (green). Right: L - curve for the $i = 0$ case, with chosen λ points (green).

solutions $P_{z,F}$ which we will describe in the following chapter).

To summarize the key results of this chapter; we have (after covering the necessary theoretical background) tested the Tikhonov regularisation method on the inverse problem of finding $P(a)$ from the GSD, where we have chosen the L-curve criterion for determining the best solution.

We tested the identity operator and the second derivative operator as the regularisation operator, and found that the identity gives better results.

To try and address the problem of the lack of symmetry in solutions, we devised a second regularisation operator, to be added to the identity operator. This transforms the minimization problem from a one-parameter to a two-parameter minimization (finding a minimum of a function of 2 variables). Since it seriously complicates the inverse problem, and still leaves the problem of negative solutions open, we concluded that the standard Tikhonov regularisation method with the identity operator is the best choice.

In Sections 5.5.1 and 5.8 we have presented the solutions for the gaps and capture zones, P and P_z, respectively, with the identity operator.

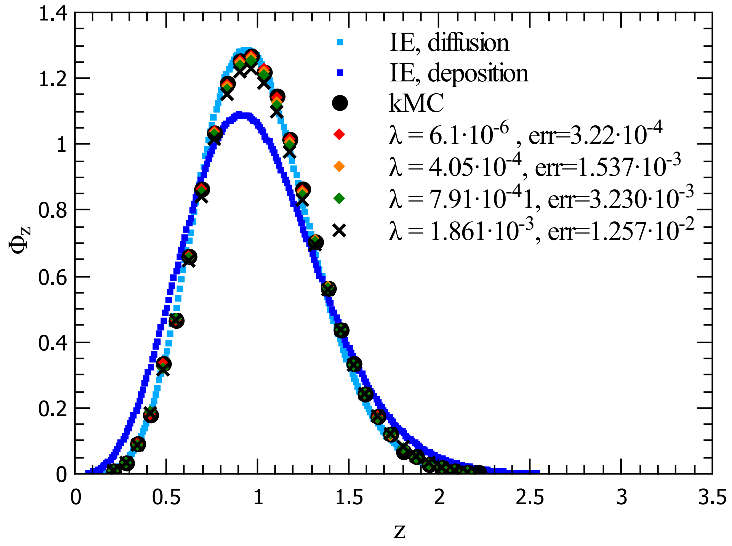

Figure 5.24: $i = 1$ case: the kMC CZD (black circles) used to calculate $P_{z,\lambda}$ and the resulting $\phi_{z,\lambda}$, shown with the diffusion and deposition case of the DFPE model (light and dark blue).

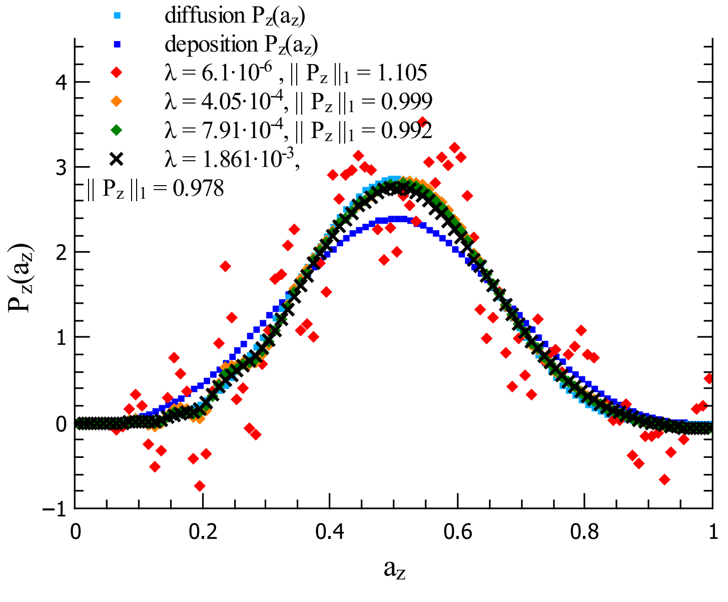

Figure 5.25: $i = 1$ case: solutions $P_{z,\lambda}$ for the choices of λ marked green on the L - curve (Figure 5.22), shown with the diffusion and deposition case of the model $P_z(a_z)$ (light and dark blue).

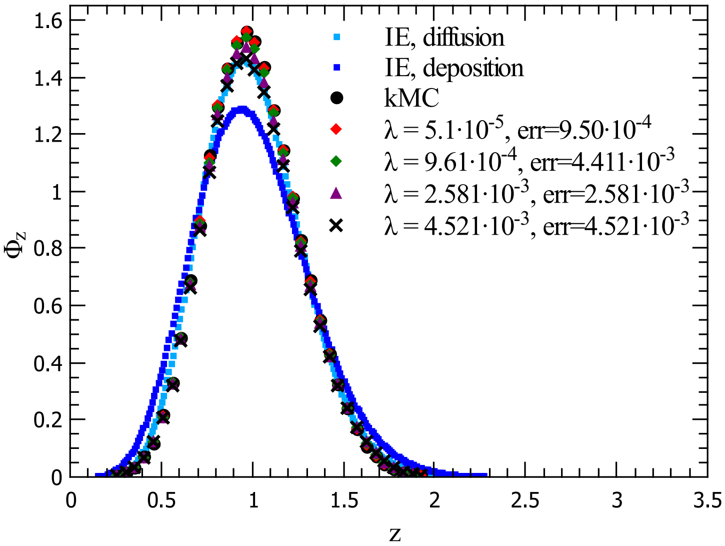

Figure 5.26: $i = 2$ case: the kMC CZD (black circles) used to calculate $P_{z,\lambda}$ and the resulting $\phi_{z,\lambda}$, shown with the diffusion and deposition case of the DFPE model (light and dark blue).

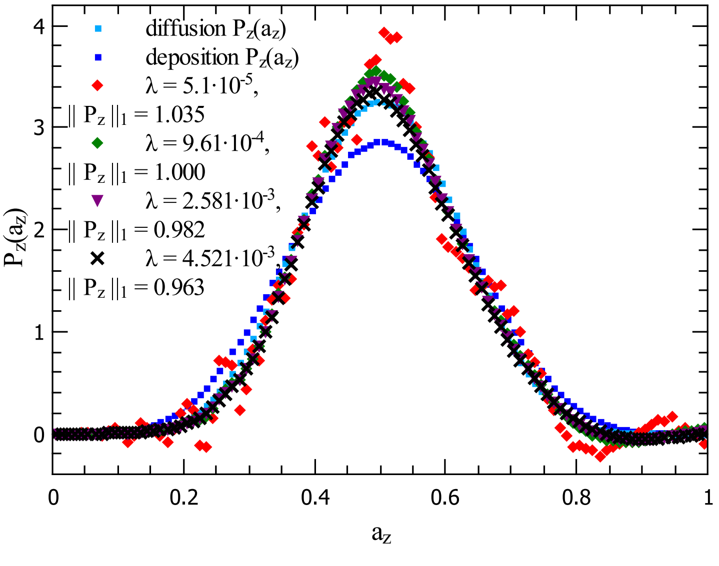

Figure 5.27: $i = 2$ case: solutions $P_{z,\lambda}$ for the choices of λ marked green on the L - curve (Figure 5.22), shown with the diffusion and deposition case of the model $P_z(a_z)$ (light and dark blue).

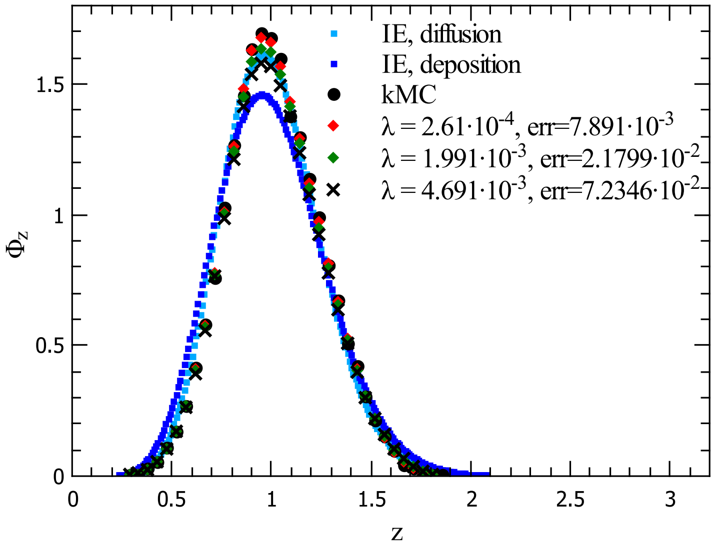

Figure 5.28: $i = 3$ case: the kMC CZD (black circles) used to calculate $P_{z,\lambda}$ and the resulting $\phi_{z,\lambda}$, shown with the diffusion and deposition case of the DFPE model (light and dark blue).

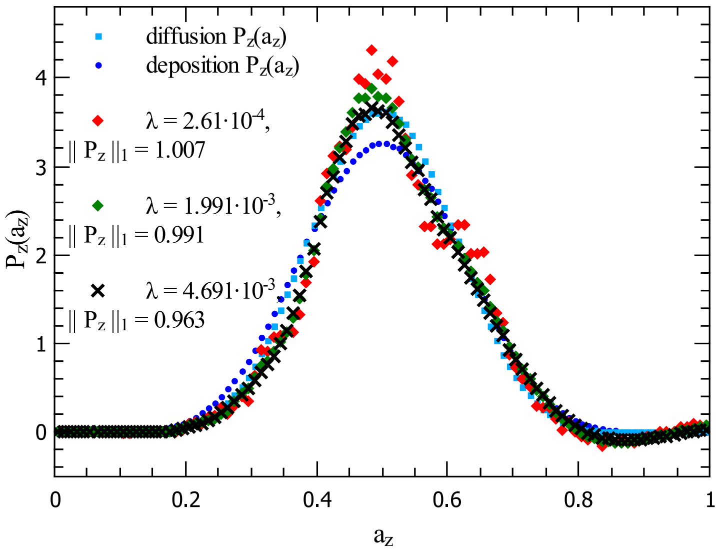

Figure 5.29: $i = 3$ case: solutions $P_{z,\lambda}$ for the choices of λ marked green on the L - curve (Figure 5.23), shown with the diffusion and deposition case of the model $P_z(a_z)$ (light and dark blue).

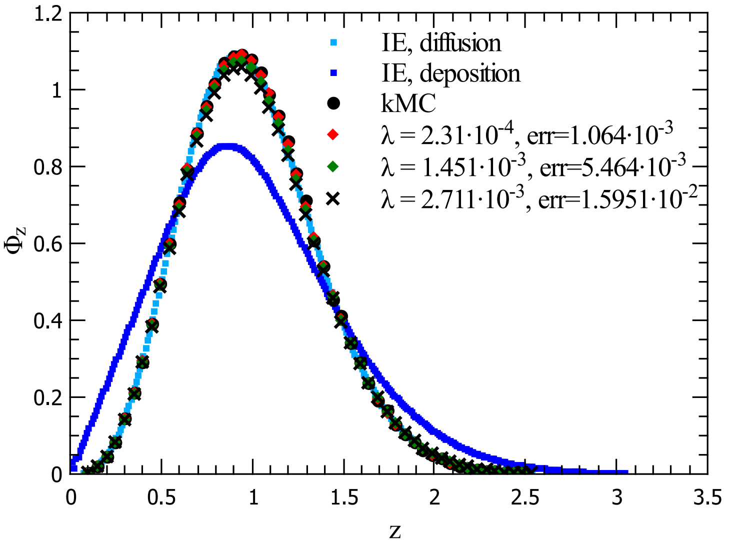

Figure 5.30: $i = 0$ case: the kMC CZD (black circles) used to calculate $P_{z,\lambda}$ and the resulting $\phi_{z,\lambda}$, shown with the diffusion and deposition case of the DFPE model (light and dark blue).

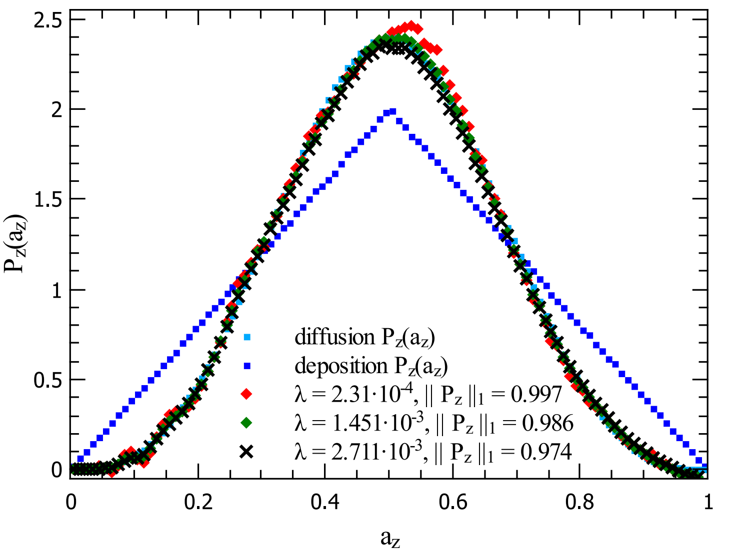

Figure 5.31: $i = 0$ case: solutions $P_{z,\lambda}$ for the choices of λ marked green on the L - curve (Figure 5.23), shown with the diffusion and deposition case of the model $P_z(a_z)$ (light and dark blue).

Chapter 6

Inverse problem and the Fourier reconstruction

In the previous chapter we have seen that the standard (Tikhonov) method of calculating $P(a)$ and $P_z(a_z)$ from a known (kMC obtained) GSD and CZD gives results that aren't entirely symmetric or positive. In this chapter, we will work out a way of finding positive and symmetric solutions.

As we have briefly mentioned before, ill-posedness of the Fredholm integral equation stems from the fact that the (sub)space U on which $K : U \to V$ operates is infinite-dimensional (the mathematical reasons for this are explained in the Appendix C). Consequently, reducing the dimensions of U is a form of regularisation. A practical application is apparent: often, in various calculation, it is convenient to represent a function as an expansion in some orthonormal basis (i.e. the Taylor series expansion). Given the shape of $P(a)$, the Fourier series is probably the most convenient choice.

The sines and cosines constitute an orthonormal basis, spanning an infinite-dimensional space over $\mathbb{R}$. A truncated expansion (cutting off all higher harmonics after some finite number N) will be in an N-dimensional space. We will use this as a way of ensuring stable solutions: with a good choice of N we should be able to get good solutions P, P_z. This is the core concept of this chapter.

We will also need to employ the Fourier series in such a way that the positivity is enforced, and the solutions have a $\|\cdot\|_1$ norm equal to 1.

To that end, we will explore 2 approaches: one that uses moments of the distribution in Section 6.1, and a second one in Section 6.2, using a simulated annealing procedure with a Fourier reconstruction.

6.1 Method of moments

Having introduced the core of regularisation via a dimension reduction, we are ready to attempt solving the inverse problem posed by the model IE (5.1).

Assuming that we know the distribution of gaps of size x, $\phi(x)$, we can calculate the moments of $\phi(x)$:

$$\langle x^n \rangle = \int_0^\infty x^n \phi(x) dx. \tag{6.1}$$

We wish to determine the corresponding distribution of a, $P(a)$. We can write it as a sum of the Fourier series. We use sines but not cosines so it is guaranteed that $P(a) = 0$ at $a = 0, 1$. By using only the sines with odd wave numbers, $k = 1, 3, 5...$, the representation of $P(a)$ is symmetric around $a = 1/2 : P(a) = \sum A_k \sin(k\pi a)$, $0 \leq a \leq 1$. With this the moments of $P(a)$, $\langle a^n \rangle$, are:

$$\langle a^n \rangle = \int_0^1 da \cdot a^n \sum_k A_k \sin(k\pi a), \tag{6.2}$$

or (with the additive property of Riemann integral):

$$\langle a^n \rangle = \sum_k A_k M(k, n), \tag{6.3}$$

where

$$M(k, n) = \int_0^1 a^n \sin(k\pi a) da. \tag{6.4}$$

Now to determine $P(a)$ we just need to find the coefficients A_k - we need to determine $\langle a^n \rangle$ and then solve (6.3).

From the DFPE $x \triangleq a(1+x)$ and with the use of binomial theorem we have [80]:

$$\langle x^n \rangle = \langle (a(1+x))^n \rangle = \langle a^n \rangle \sum_{i=0}^{n} \binom{n}{i} \langle 1^{n-i} \rangle \langle x^i \rangle = \langle a^n \rangle \sum_{i=0}^{n} \frac{n!}{i!(n-i)!} \langle x^i \rangle. \tag{6.5}$$

Side note: from this, if $\langle a^n \rangle$ (that is, $P(a)$) are known, we can build the moments $\langle x^n \rangle$ through

$$\langle x^n \rangle = \frac{\langle a^n \rangle}{1 - \langle a^n \rangle} \sum_{i=0}^{n-1} \frac{n!}{i!(n-i)!} \langle x^i \rangle \tag{6.6}$$

by defining the zeroth moment $\langle x^0 \rangle = 1$.

Moments $\langle a^n \rangle$ were calculated from (6.5), where the moments $\langle x^i \rangle$ were obtained in two ways:

a) from the simple MC procedure (DFPE) described in the previous chapter. The (normalised) heights of bins that previously created histograms were used as $\phi(x)$. We got best results when taking the interval $x \in [0, 10]$ and 1000 bins (of base width 0.01). We ran the MC program that creates gaps a thousand times, calculated the moments $\langle x^i \rangle$ and $\langle a^n \rangle$ for each run and then took the average values of $\langle a^n \rangle$ as the final result.

b) from the integral equation, with $P(a) = Na^\alpha(1-a)^\alpha$. It was solved with the iterative procedure to obtain $\phi(x)$, which was then used to integrate (6.1) numerically.

We calculated the moments for the case of diffusion driven nucleation ($\alpha = i + 1$) with critical island size $i = 0$ and for the Dickman distribution. The results are presented in Table 6.1, with the accurate moments for comparison:

$$\langle a^n \rangle = \int_0^1 a^n P(a) da = 6 \int_0^1 a^n a(1-a) da = \frac{6}{n+2} - \frac{6}{n+3}, \tag{6.7}$$

and for the Dickman case:

$$\langle a^n \rangle = \int_0^1 a^n P(a) da = \int_0^1 a^n da = \frac{1}{n+1}. \tag{6.8}$$

$P(a) = 6a(1-a)$ (crit.isl.size $i = 0$)				Dickman case, $P(a) = 1$			
n	accurate $\langle a^n \rangle$	from MC	from IE	n	accurate $\langle a^n \rangle$	from MC	from IE
0	1.000000	1.000000	1.000000	0	1.000000	1.000000	1.000000
1	0.500000	0.500000	0.499961	1	0.500000	0.500001	0.499806
2	0.300000	0.300003	0.299962	2	0.333333	0.333332	0.332631
3	0.200000	0.200006	0.199969	3	0.250000	0.249998	0.249033
4	0.142857	0.142864	0.142834	4	0.200000	0.199996	0.198874
5	0.107143	0.107149	0.107125	5	0.166667	0.166656	0.165436
6	0.083333	0.083338	0.083320	6	0.142857	0.142835	0.141553
7	0.066667	0.066669	0.066656	7	0.125000	0.124960	0.123640
8	0.054545	0.054543	0.054537	8	0.111111	0.111044	0.109708
9	0.045455	0.045446	0.045448	9	0.100000	0.099891	0.098563
10	0.038462	0.038444	0.038456	10	0.090909	0.090735	0.089444
11	0.032967	0.032936	0.032962	11	0.083333	0.083054	0.081845
12	0.028571	0.028522	0.028567	12	0.076923	0.076470	0.075414
13	0.025000	0.024921	0.024996	13	0.071429	0.070692	0.069901
14	0.022059	0.021935	0.022056	14	0.066667	0.065486	0.065122
15	0.019608	0.019414	0.019605	15	0.062500	0.060666	0.060937
16	0.017544	0.017247	0.017541	16	0.058824	0.056099	0.057239
17	0.015789	0.015347	0.015787	17	0.055556	0.051703	0.053944
18	0.014286	0.013653	0.014283	18	0.052632	0.047443	0.050985
19	0.012987	0.012122	0.012985	19	0.050000	0.043322	0.048305
20	0.011858	0.010729	0.011856	20	0.047619	0.039358	0.045857

Table 6.1: Comparison of moments calculated in different ways

Now to obtain the Fourier coefficients A_k from equation (6.3) we only need the moments of harmonics:

$$M(k, n) = \int_0^1 a^n \sin(k\pi a) da. \tag{6.9}$$

By integrating (6.9), we get a formula for odd n:

$$M(k, n_o) = \frac{1}{k\pi} + \sum_{m=1}^{(n-1)/2} \frac{(-1)^m}{(k\pi)^{2m+1}} \frac{n!}{(n-2m)!} \tag{6.10}$$

and for even n:

$$M(k, n_e) = \frac{1}{k\pi} + \sum_{m=1}^{(n-2)/2} \frac{(-1)^m}{(k\pi)^{2m+1}} \frac{n!}{(n-2m)!} + (-1)^{n/2} \frac{n!}{(k\pi)^n} \frac{2}{k\pi}. \tag{6.11}$$

So now the system (6.3) is split into two systems, for odd and even n (n_o or n_e), and $n = k$ (otherwise the problem is under or over-imposed).

The end goal was to solve (6.3) for $\langle x^{n_{o/e}} \rangle$ calculated from kMC data through (6.5), that is, to solve two sets of equations

$$\langle x^{n_{o/e}} \rangle \left(\sum_{i=0}^{n_{o/e}} \frac{(n_{o/e})!}{i!(n_{o/e}-i)!} \langle x^i \rangle \right)^{-1} = \sum_k A_k M(k, n_{o/e}), \tag{6.12}$$

but first we tested this method by solving (6.3) with $\langle a^n \rangle$ calculated from a known distribution, $P(a) = N a^i (1-a)^i$ where N is the normalization factor.

We used a subroutine from [6] to solve (6.3), one that solves a system of $n \times n$ linear equations $Mx = A$ with the use of LU decomposition:
here the $n \times n$ matrix is decomposed into a product of 2 triangular matrices, $LU = M$, where L has elements only on the diagonal and below and U on the diagonal and above. Decomposition is performed with Crout matrix decomposition algorithm. The system then becomes $Mx = L(Ux) = A$ and it is first solved for a vector y such that $Ly = A$ and then for the vector x which satisfies $Ux = y$. Both systems are of course trivial since L and U are triangular.

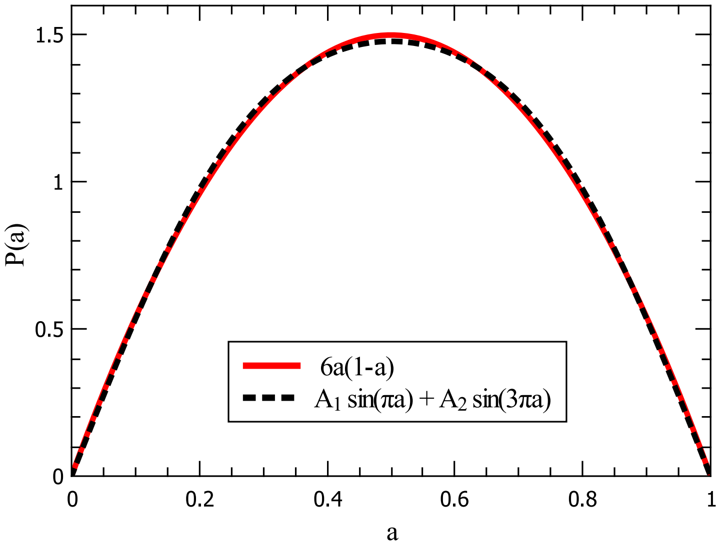

Figure 6.1: Solution of the 2 × 2 problem.

For the 2×2 problem ($k = 1, 3$ and $n = 1, 2$) and the simplest case of critical island size $i = 0$, we got the solutions $A_1 = 1.5477$, $A_2 = 0.0691$. Visual comparison of this Fourier representation and the original $P(a) = 6a(1 - a)$ is quite good, as can be seen on Figure 6.1.

However, on the 3×3 problem this method broke down. The probability distribution became negative and we couldn't impose $P(a) \geq 0$ for $a \in [0, 1]$. Instead of a sequence of decreasing amplitudes from the largest A_1, we got $A_1 = 1.7$, $A_2 = -6.7$ and $A_3 = 10.4$. The solution would rapidly change for extra decimal places in the input matrix elements and moments as shown on Figure 6.2, where the difference between the three solutions is just one extra decimal place of input values. The gap size distribution that results from these $P(a)$ is shown on Figure 6.3.

The equation the solver 'sees' looks like (here rounded to just two digits for sim-

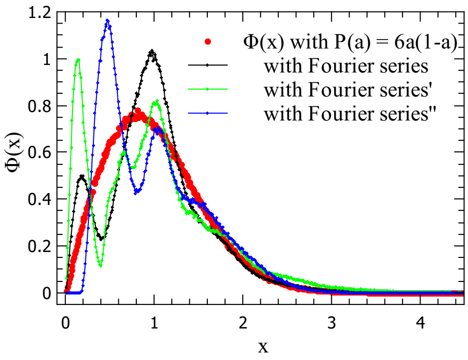

Figure 6.2: Solutions for the 3 × 3 problem, shown with the true $P(a) = 6a(1-a)$.

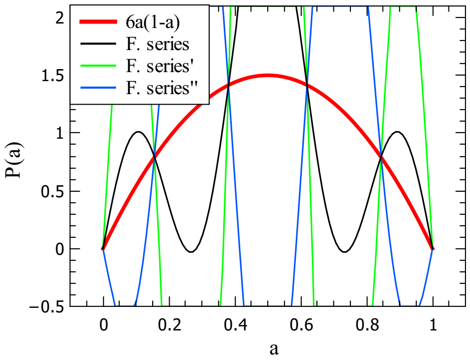

Figure 6.3: The corresponding $\phi(x)$ for the 3 × 3 problem.

plicity):

$$
\begin{aligned}
A_1 \cdot 0.32 + A_2 \cdot 0.11 + A_3 \cdot 6.36 \cdot 10^{-2} &= 0.5 \\
A_1 \cdot 0.19 + A_2 \cdot 0.10 + A_3 \cdot 6.26 \cdot 10^{-2} &= 0.3 \\
A_1 \cdot 0.13 + A_2 \cdot 0.09 + A_3 \cdot 6.21 \cdot 10^{-2} &= 0.2 \qquad (6.13)
\end{aligned}
$$

The matrix containing the moments of sines, $M_{3\times3}$, is here full-rank, has an inverse and a trivial nullspace. But the problem is still ill - posed, so drastically that changing just the number of decimals in the input values (replacing 0.50009 with 0.5001 in the input, for example) results in huge solution oscillations, as seen on Figure 6.2.

We have replaced the original inverse problem with Equation (6.3), but the sources of ill - posedness (the kernel from the IE; discussed in the Appendix C) are now entangled and hidden on the right hand side of the system (6.13). This puts us into a worse situation than we were with the original problem of solving the IE for P and, additionally, there is no satisfying way of ensuring positive solutions, so we have abandened this method.

Finding an optimal solution here meant choosing an optimal number of harmonics to be used in the Fourier expansion so that the solution doesn't exhibit high frequency oscillations. Choosing optimal parameter(s) and solutions is inevitable when dealing with ill-posed problems, however in our case we also need the solutions to be positive.

Since we cannot enforce positivity with this method, much like with the Tikhonov method before, the only way to ensure $P > 0$ is to choose a positive solution (if we can find one) at the very end. The annealing method we will describe in the next section will finally allow us to impose positivity.

6.2 Annealing and the Fourier reconstruction method

In this approach, we aimed to solve the inverse problem by constructing $P(a)$ directly as a Fourier series, with an algorithm that adds random harmonics and tests if this brings us closer to the solution. We started with the numerically integrated IE to develop the method for a known $P(a)$ before applying it to kMC data.

We calculated the IE iteratively with $P(a) = Na^{\alpha}(1-a)^{\alpha}$, N being the normalization constant, as described in Chapter 4.1. For the resultant $\phi(x)$ we want to reconstruct $P(a)$ as a partial sum of the Fourier series, by randomly adding harmonics in a search that minimizes the error defined as the difference between the original $\phi(x)$ and the $\phi_F(x)$ calculated for this Fourier-constructed $P_F(a)$. When applying this method to kMC simulation results, the original $\phi(x)$ is the GSD obtained as a histogram from kMC data and ϕ_F is obtained by numerically integrating IE with the Fourier representation of $P(a)$.

Downhill method

Our algorithm starts by defining $P_{F,old}(a)$ as a single sine:

$$P_{F,old}(a) = N \sin(\pi a) \tag{6.14}$$

where N is the normalization constant, and calculate $\phi_{F,old}(x)$ for it with the iterative procedure. We then calculate the difference between this $\phi_{F,old}(x)$ and the original $\phi(x)$ and define it as the initial error (mean square error):

$$err\_old = \sum_j \left(\phi_{F,old}(x_j) - \phi(x_j)\right)^2 \tag{6.15}$$

Then we randomly (using Fortran's built-in random number generator) choose a harmonic, that is, we choose a random odd integer k (for $\sin k\pi a$). The possible values from which we choose are $k = 1, 3, 5, ..., k_{max}$ where k_{max} is a predefined parameter; we've run the program for various choices of k_{max}.

Next, we choose a random amplitude A for this harmonic (any real number smaller than a predefined A_{max}).

We add $A \sin(k\pi a)$ to $P_{F,old}$:

$$P_{F,new}(a) = P_{F,old} + A \sin(k\pi a) \tag{6.16}$$

and check if $P_{F,new}$ is acceptable as a probability distribution:
If $P_{F,new}(a) < 0$ for $a \in [0, 1]$ we reject this $A \sin(k\pi a)$ and choose another pair of k, A. If $P_{F,new}(a) \geq 0$, we keep it, calculate $\phi_{F,new}(x)$ for $P_{F,new}(a)$ with the iterative procedure, and then calculate the error:

$$err\_new = \sum_j \left(\phi_{F,new}(x_j) - \phi(x_j)\right)^2 \tag{6.17}$$

If $err\_new > err\_old$ we reject this $A \sin(k\pi a)$ and choose another to construct $P_{F,new}$. If $err\_new < err\_old$, then this $P_{F,new}(a)$ and $\phi_{F,new}$ are closer to the true $P(a)$ and $\phi(x)$ than $P_{F,old}(a)$ and $\phi_{F,old}(x)$ are, so we rewrite $P_{F,old}$ in the procedure as $P_{F,new}$:

$$\begin{aligned} &P_{F,new}(a) \rightarrow P_{F,old}(a) \\ &err\_new \rightarrow err\_old \end{aligned} \tag{6.18}$$

and proceed to another random choice of a harmonic that will be added to $P_{F,old}(a)$ to get $P_{F,new}(a)$ according to (6.16) and err_new according to (6.17). The predefined number of these cycles is the third parameter of the method.

The idea was to find the optimal values of the parameters for the known IE ϕ and $P(a)$, and then run the procedure with the kMC obtained $\phi(x)$; however we have only been able to reconstruct the true $P(a) = Na^{\alpha}(1-a)^{\alpha}$ for critical island sizes $i = 0, 1, 2$

(in a diffusion driven nucleation, $\alpha = i + 1$) so a refinement of the method was needed.

Simulated anneal

Unlike the downhill method where we accepted $P_{F,new}$ if its error was smaller than in the previous attempt ($err\_new < err\_old$), here we accept $P_{F,new}(a)$ with the probability:

$$p = e^{-(err\_new - err\_old)\beta} \tag{6.19}$$

where the inverse 'temperature' β is initially set to $\beta = 1$. To achieve this, we use the random number generator to choose a real number $R \in [0, 1]$; if $R < p$ we accept $P_{F,new}$ and rewrite $P_{F,old}$ with it according to (6.18). If $R > p$ we reject it and choose another $P_{F,new}$.

After a predetermined number m of such cycles, we increase β by one and repeat the m cycles.

After the inverse 'temperature' β has been increased M times, the program stops.

This procedure alone has not given satisfactory results, but following it with the downhill method, we have reproduced the original $P(a)$.

Figure 6.4 illustrates why the downhill method shouldn't be used alone: the constraint $err\_new < err\_old$ means that we can get trapped in a local minimum in the $error(A, k)$ landscape. Allowing the harmonics to increase the error according to (6.19), it is possible to escape these local minima (illustrated with blue arrows) and reach a global minimum. After this, the downhill method corrects $P_{F,new}$; that is, we slide into the global minimum (green arrow).

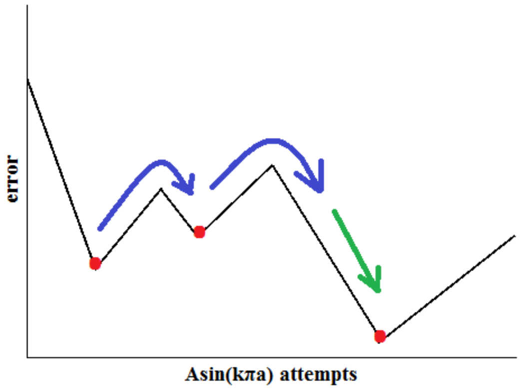

Figure 6.4: Illustration of the search of $P_{F,new}$ for which the error is minimal.

6.2.1 GSD results

Just like in the previous method with moments of the distribution, adding higher harmonics resulted in oscillations of the reconstructed $P(a)$ around its true shape: on Figure 6.5, right panel, we show solutions P_F built with different numbers of harmonics (the solutions with higher harmonics contributions are the ones that oscillate more around the true shape of P). The left panel shows the result of integrating those P_F solutions: ϕ_F, all lying perfectly on top of each other.

The reason for this is that increasing the accuracy of the numerical approximation of a continuous kernel $\kappa : U \to V$ where $\dim(U) = \infty$, that is, increasing the number of dimensions of the finite - dimensional numerical approximation of U, results in an increase of the condition number of the kernel matrix. In other words, increasing the number of harmonics means increasing the number of base elements spanning U (increasing the dimension of U), which brings us closer to the continuous kernel κ operating on an infinite-dimensional space U, where the problem is *necessarily* ill-posed. The origin of this can be found in the Appendix C (Theorem C.4).

Therefore, to stabilize the solutions we had to limit the maximum number of harmonics to 5 (so, $k = 3, 5, 7, 9, 11$).

With allowed maximum amplitudes $A_{max} = 0.05$ and $k_{max} = 11$ we ran the simulated anneal with $M = 500$ and $m = 30$ (500×30 cycles) and then applied the downhill

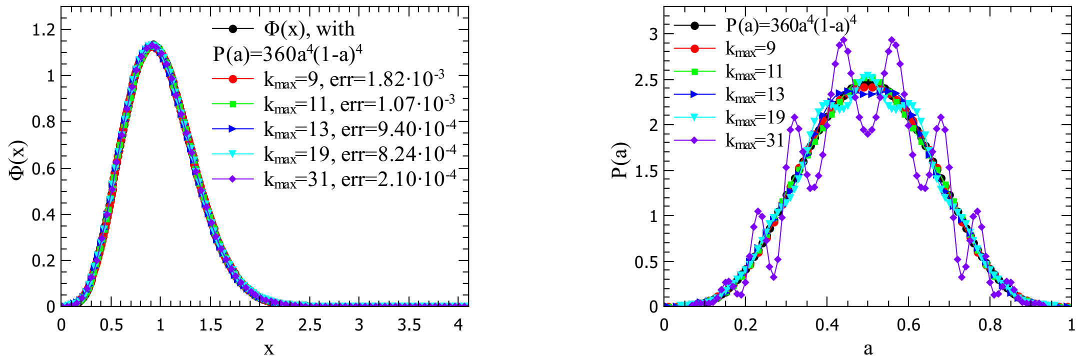

Figure 6.5: Searching for the optimal k_{max}

method with, again, $A_{max} = 0.05$ and $k_{max} = 11$ and up to 300 attempts of finding an improved P_{new}.

The results for the case $i = 1$ are shown on Figures 6.6 and 6.7, both for the IE with $P(a) = Na^{\alpha}(1-a)^{\alpha}$ (ϕ_{IE}) and the GSD obtained from averaging 100 runs of a kMC simulation on a lattice with 10^6 sites, $R = 10^7$ and 100% coverage (ϕ_{kMC}). Reconstructed ϕ_F (integrated from the IE with Fourier constructed $P_F(a)$), both for the kMC data and the IE, match their respective originals very well, but since the original kMC GSD is not smooth the recovered ϕ_F has a larger error. The Fourier construction of $P_F(a)$ for the kMC GSD lies between theoretical $P(a)$ for diffusion and deposition, as we would expect for realistic island growth.

Results of the kMC simulations for the case $i = 2$ have a lot more noise than for the $i = 1$ case, so the recovered ϕ_F deviates visibly from the ϕ_{kMC}; it is in fact lying on top of diffusion ϕ_{IE} rather than on ϕ_{kMC}. So the Fourier constructed $P_F(a)$ also coincides with theoretical $P(a)$ for diffusion. Because of the noise and the fact that the error minimised in the procedure is the sum of distances between recovered ϕ_F and ϕ_{kMC} *squared*, we weren't able to get a recovered ϕ_F that better fits the true ϕ_{kMC}.

The case $i = 3$ is dominated by noise, so the best ϕ_F we recovered has an error three orders of magnitude higher that the relatively noise - free $i = 1$, making this solution's validity questionable.

Reconstruction of the ϕ_{IE} for $P(a) = 1$ (corresponding to deposition, $i = 0, \alpha = i$)

- the Dickman distribution, isn't successful. This case is problematic even as a direct problem - the 'true' $\phi_{IE}(x)$ calculated iteratively with $P(a) = 1$, shown in black on Figure 6.12, is noisy and discontinuous near zero.

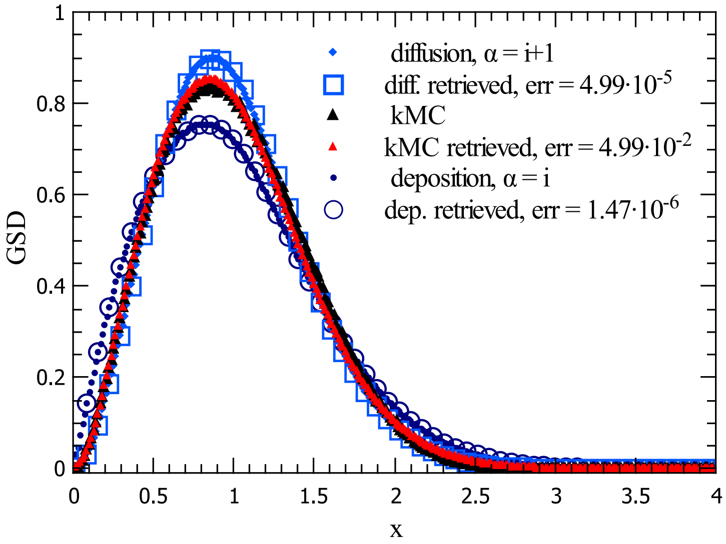

Figure 6.6: GSD from kMC data for $i = 1$ and the reconstructed GSD, shown with IE solutions for deposition and diffusion (original and reconstructed).

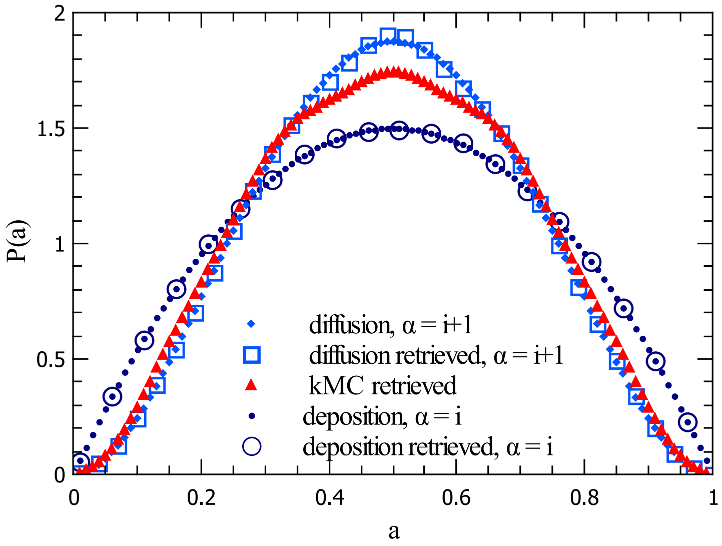

Figure 6.7: The corresponding $P(a)$ for $i = 1$ (original and reconstructed).

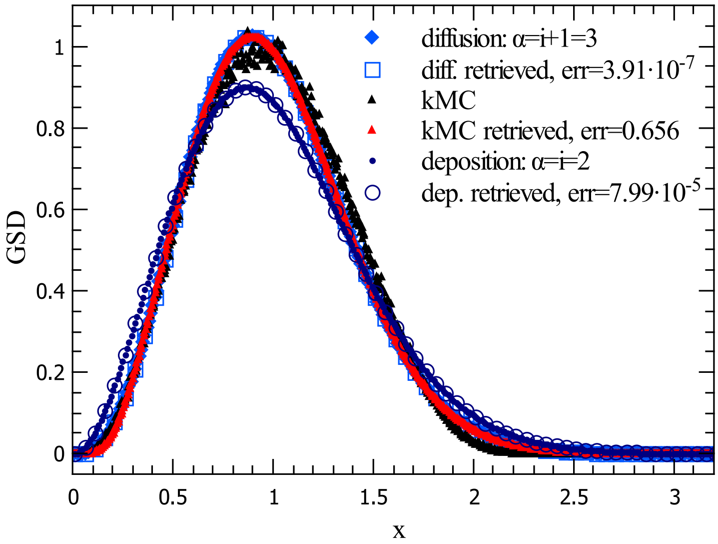

Figure 6.8: GSD from kMC data for $i = 2$ and the reconstructed GSD, shown with IE solutions for deposition and diffusion (original and reconstructed).

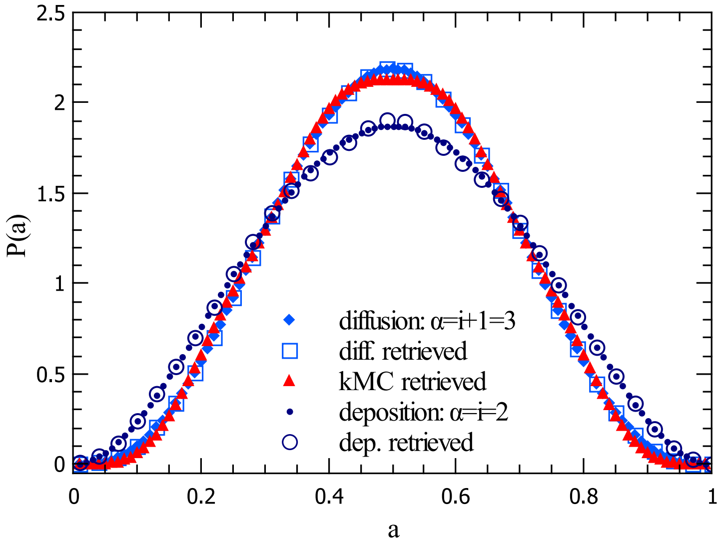

Figure 6.9: The corresponding $P(a)$ for $i = 2$ (original and reconstructed).

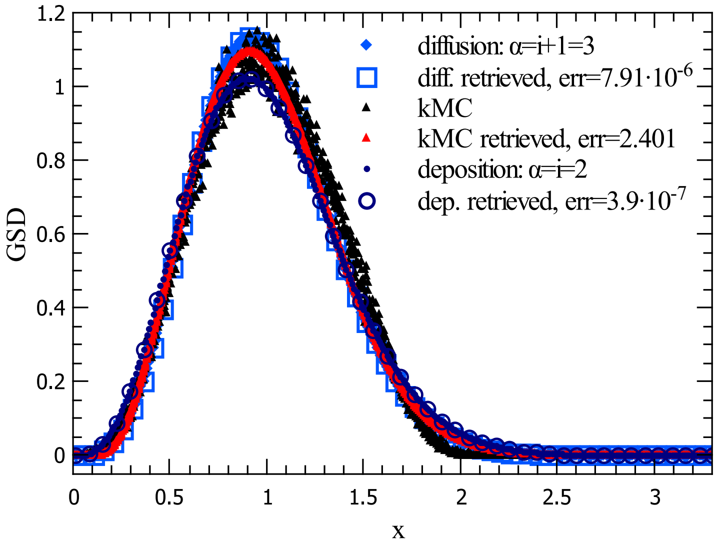

Figure 6.10: GSD from kMC data for $i = 3$ and the reconstructed GSD, shown with IE solutions for deposition and diffusion (original and reconstructed).

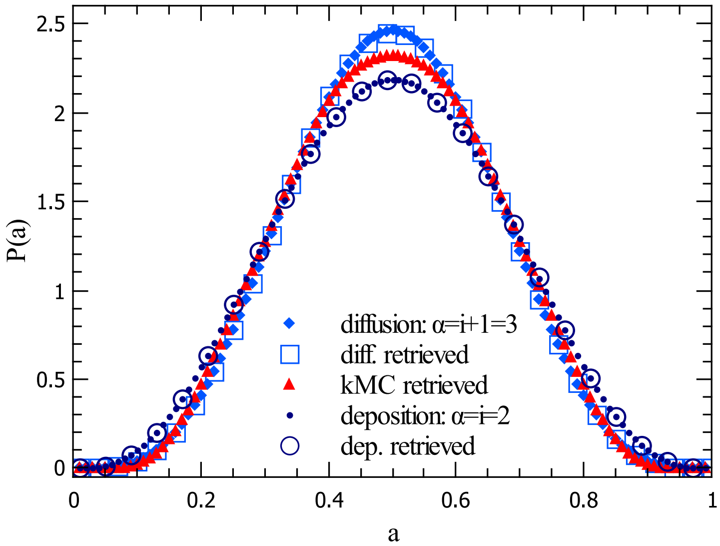

Figure 6.11: The corresponding $P(a)$ for $i = 3$ (original and reconstructed).

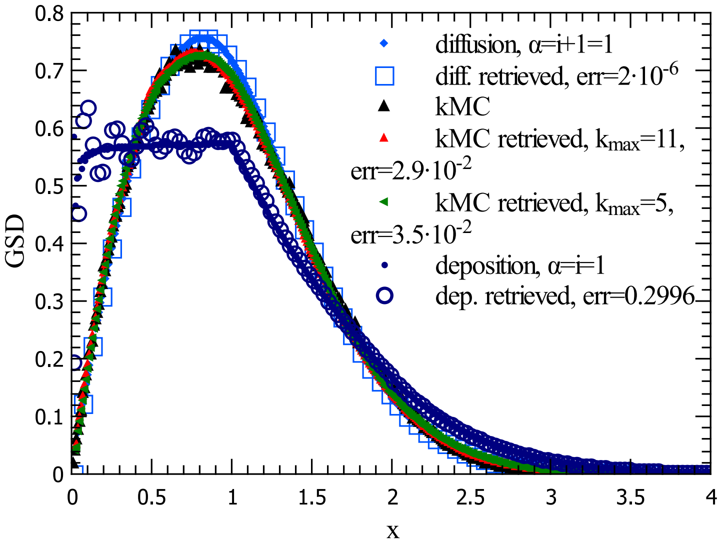

Figure 6.12: GSD from kMC data for $i = 0$ and the reconstructed GSD, shown with IE solutions for deposition and diffusion (original and reconstructed).

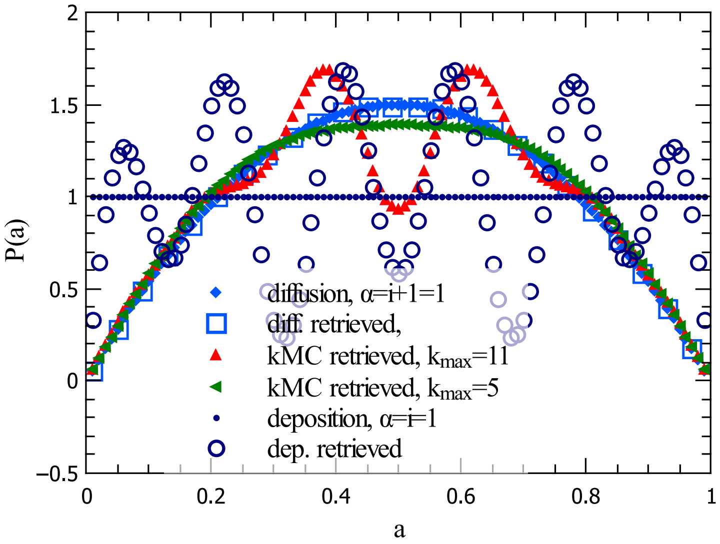

Figure 6.13: The corresponding $P(a)$ for $i = 0$ (original and reconstructed).

Reconstruction of $P(a)$ for the $i = 0$ case of kMC GSD, with the same parameters that gave stable solutions in the previous cases, is shown on Figure 6.12 and 6.13. It deviates more than the other cases from what we expected to get and is very unstable.

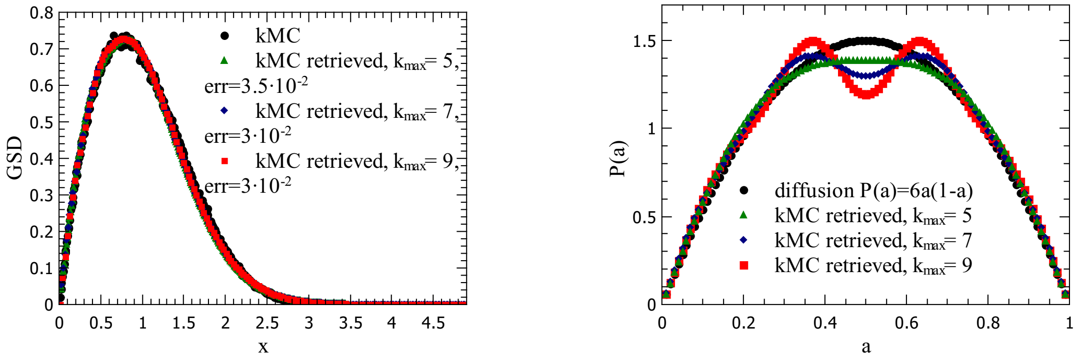

Figure 6.14: Solutions for different k_{max}, for inversion of kMC obtained GSD, $i = 0$.

Allowing the maximum number of harmonics to be $k_{max} = 11$ doesn't restrict this problem enough; this can be seen on Figure 6.14 where we try out solutions for lower number of harmonics. A solution with $k_{max} = 5$ (also shown on Figures 6.12 and 6.13) is chosen as the best one.

6.2.2 CZD results

Capture zone distributions can be calculated from convolutions of the corresponding GSDs (Eqn. (2.23)):

$$A_c(z) = 2\int_0^{2z} \phi(t)\phi(2z-t)dt \tag{6.20}$$

(We assume here that the neighbouring gaps aren't correlated.) Alternatively, CZDs can be obtained directly from kMC simulation. Since we assume that CZDs are modelled by the DFPE:

$$z \triangleq \frac{1}{2}\left(a_1 + a_2\right)\left(1 + z\right) \tag{6.21}$$

we applied the annealing algorithm to CZDs obtained from the kMC simulations (also averaged over 100 runs) just like for the GSDs before, and compared the results with the ones integrated from GSDs according to Equation (6.20). Here we also show the generalized Wigner surmise (GWS, Equation (2.17)): $A_\beta(z) = a_\beta z^\beta e^{-b_\beta z^2}$.

We expected to get the Fourier - constructed $P_F(a_z)$ that lies between the theoretical $P_z(a_z)$ for diffusion and deposition. These two were calculated as histograms from a sample of $5 \cdot 10^6$ values $\frac{1}{2}(a_1 + a_2)$, where a_1 and a_2 were drawn from $P(a) = Na^{\alpha}(1-a)^{\alpha}$.

Results for $i = 0, 1$ were obtained with the same set of parameters as the $i = 1, 2, 3$ GSDs before: with allowed maximum amplitudes $A_{max} = 0.05$ and $k_{max} = 11$ the simulated anneal ran with $M = 500$ and $m = 30$ (500×30 cycles) and then the downhill method was used with, again, $A_{max} = 0.05$ and $k_{max} = 11$ and up to 300 attempts of finding an improved $P_{F,new}$.

For higher critical island sizes a higher inverse 'temperature' was needed, and for $i = 3$, to smooth out the otherwise too noisy kMC results, histograms that give CZD were created with double the bin base width. So, for $i = 2, 3$, with allowed maximum amplitudes $A_{max} = 0.05$ and $k_{max} = 11$ we ran the simulated anneal with $M = 500$ and $m = 70$ (500×70 cycles) and then applied the downhill method ($A_{max} = 0.05$ and $k_{max} = 11$) with up to 700 attempts of finding an improved $P_{F,new}$.

Results of the annealing procedure are shown with the original kMC obtained CZDs in Figures 6.15, 6.17, 6.19 and 6.21. Additionally, CZDs obtained as convolutions (6.20) from the corresponding kMC GSDs are shown, alongside the GWS.

In Figures 6.16, 6.18, 6.20 and 6.22, Fourier reconstructed $P_F(a_z)$ are shown, with the assumed theoretical $P_z(a_z)$ distributions for diffusion and deposition, calculated as histograms from $\dfrac{1}{2}(a_1 + a_2)$ samples.

All of the CZDs calculated as convolutions from kMC GSDs fall slightly below the true CZDs (the kMC CZDs). Convolution (6.20) is based on an assumption that there is no correlation between neighbouring gap sizes; the discrepancy between the two plots suggests that there might be some correlation between the adjacent gaps.

Interestingly, GWS for $i = 1, 2$ lies on top of the convolution curves, rather than on the true kMC CZDs. It makes an excellent fit for the kMC data only in the $i = 3$ case.

The reconstructed $P_F(a_z)$ is consistently higher than the upper, diffusion limit. This is most likely a result of the fact that convolution of GSD doesn't agree completely with the kMC measured CZD.

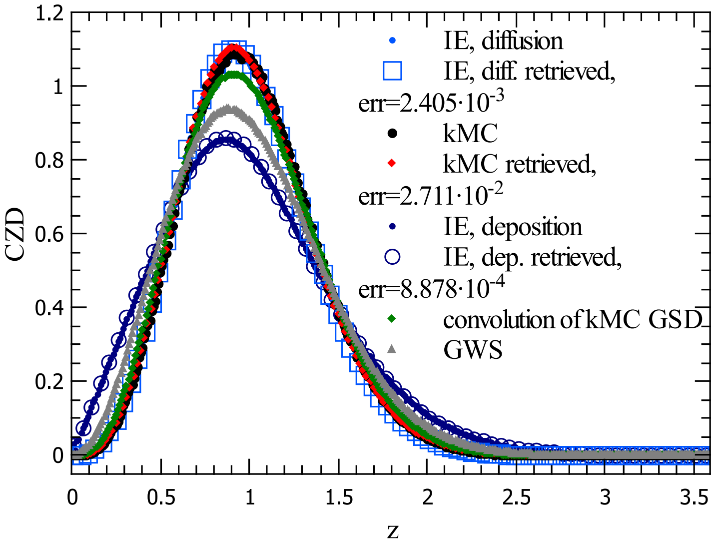

Figure 6.15: CZD from kMC data for $i = 0$ (dark green) and the reconstructed CZD (light green), shown with CZD obtained by integrating kMC GSD (Equation (6.20), shown in gray) and GWS (light blue). Shown within the diffusion (pink) and deposition (black) theoretical predictions; retrieved diffusion and deposition solutions are plotted on top (blue, red).

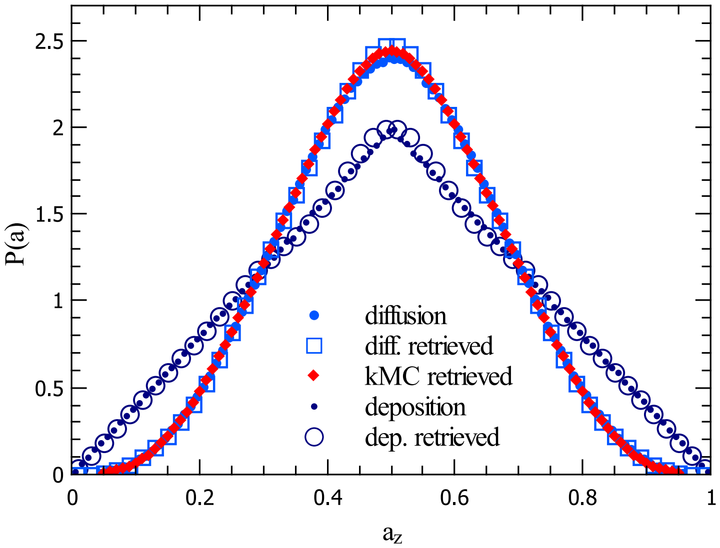

Figure 6.16: Reconstructed $P_F(a_z)$ (light green) shown with theoretical $P_z(a_z)$ for diffusion (pink) and deposition (black) (from (6.21)).

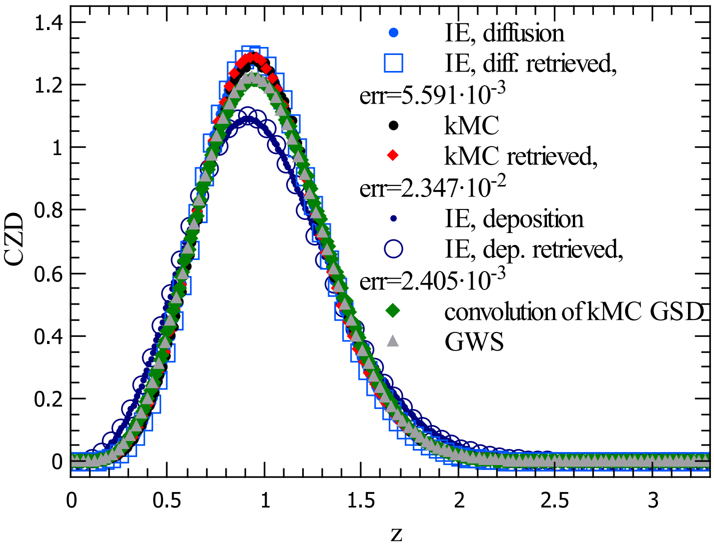

Figure 6.17: CZD from kMC data for $i = 1$ (dark green) and the reconstructed CZD (light green), shown with CZD obtained by integrating kMC GSD (Equation (6.20), shown in gray) and GWS (light blue). Shown within the diffusion (pink) and deposition (black) theoretical predictions; retrieved diffusion and deposition solutions are plotted on top (blue, red).

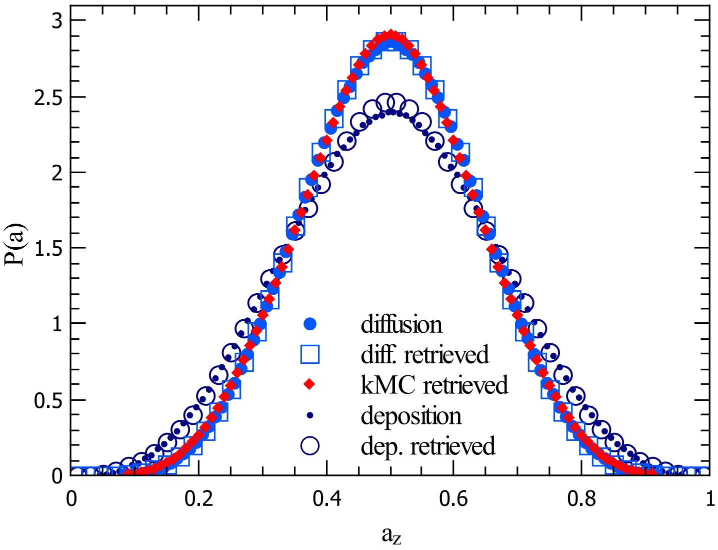

Figure 6.18: Reconstructed $P_F(a_z)$ (light green) shown with theoretical $P_z(a_z)$ for diffusion (pink) and deposition (black) (from (6.21)).

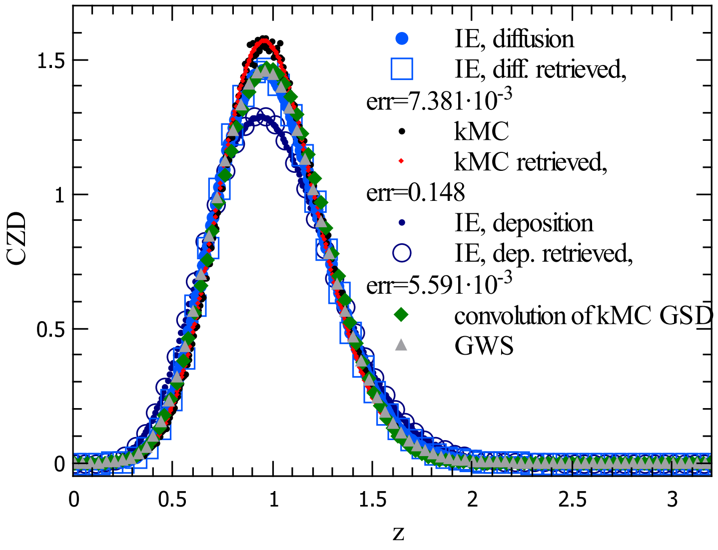

Figure 6.19: CZD from kMC data for $i = 2$ (dark green) and the reconstructed CZD (light green), shown with CZD obtained by integrating kMC GSD (Equation (6.20), shown in gray) and GWS (light blue). Shown within the diffusion (pink) and deposition (black) theoretical predictions; retrieved diffusion and deposition solutions are plotted on top (blue, red).

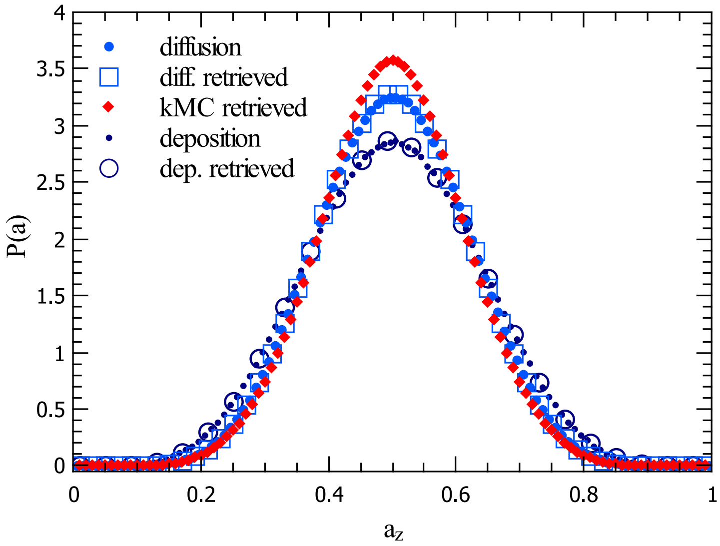

Figure 6.20: Reconstructed $P_F(a_z)$ (light green) shown with theoretical $P_z(a_z)$ for diffusion (pink) and deposition (black) (from (6.21)).

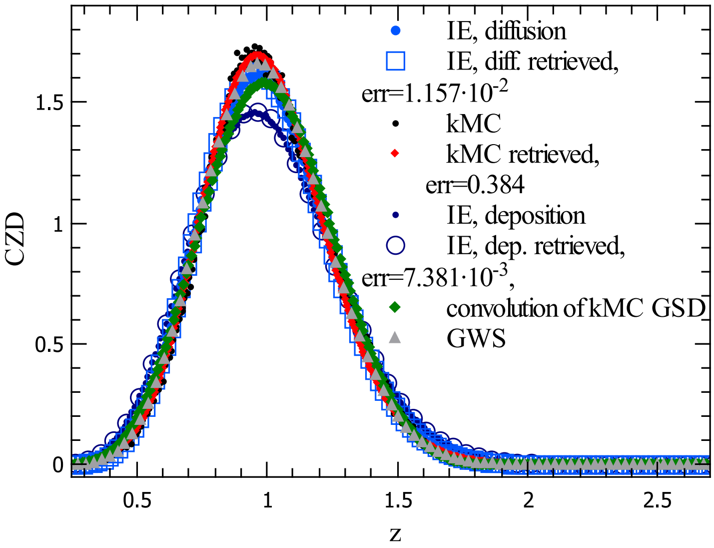

Figure 6.21: CZD from kMC data for $i = 3$ (dark green) and the reconstructed CZD (light green), shown with CZD obtained by integrating kMC GSD (Equation (6.20), shown in gray) and GWS (light blue). Shown within the diffusion (pink) and deposition (black) theoretical predictions; retrieved diffusion and deposition solutions are plotted on top (blue, red).

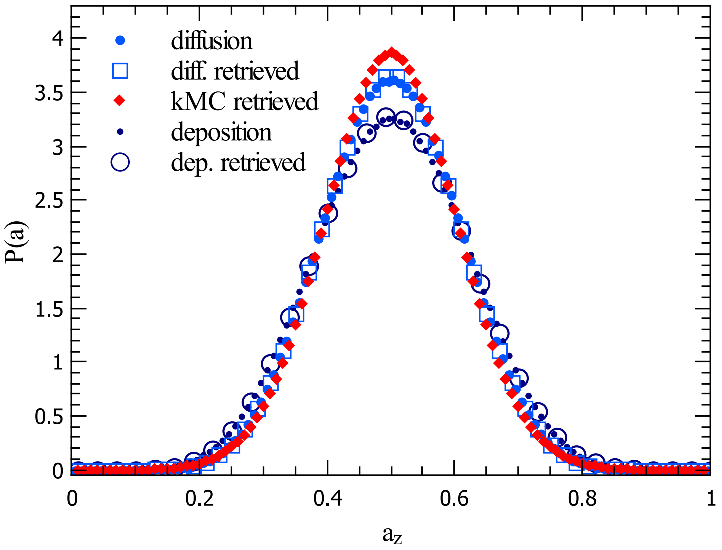

Figure 6.22: Reconstructed $P_F(a_z)$ (light green) shown with theoretical $P_z(a_z)$ for diffusion (pink) and deposition (black) (from (6.21)).

In this chapter, we have set out to devise a method of solving the inverse problem which ensures positivity, symmetry and the preservation of the 1-norm of the solutions.

We developed and tested two methods: first, one that uses the idea that the distribution $P(a)$ can be reconstructed from its moments. While it did give symmetric solutions, the method of moments didn't enforce positivity: positive solutions can only be chosen post-calculation, like before with the Tikhonov regularisation.

In the second method, we reconstruct the wanted solutions P directly as a Fourier series, and then keep rebuilding it until the final, true solution is found. This method allows us to immediately eliminate possible negative solutions, which finally brings us to our goal. From a practical standpoint, when comparing the Fourier reconstruction with the Tikhonov regularisation of the previous chapter, the Tikhonov method is easier to use (just one parameter which needs to be optimized), and the runtime is much shorter. So it would be a preferred choice when just a rough solution is needed quickly. For finding good solutions that satisfy all of the physical system requirements, the Fourier reconstruction method has to be used.

Chapter 7

Comparison of the inverse problem solutions and the kMC obtained $P(a)$

In the previous two chapters we have explored the Tikhonov regularisation method and the Fourier reconstruction for solving the inverse problem: calculating $P(a)$ from the corresponding integral equation when the GSD (or CZD) is known. In this chapter we will compare the solutions from the two methods against each other, and the true (kMC obtained) results. Partly, this chapter is a collection of the best results of Chapters 5 and 6, but there is also something new to be added: we can, only for the case of the gaps, measure $P(a)$ directly from kMC simulations; call it $P_{kMC}(a)$.

We will therefore first revisit the kMC simulations and explain the procedure for measuring P_{kMC}, and then check how well do the inverse problem solutions for the gaps match it.

For the case of the capture zones, we aren't able to obtain $P_z(a_z)$ directly from the kMC simulations in any way, so in the second part of this chapter we will only show the best inverse problem solutions of Chapters 5 and 6, plotted together for comparison.

7.1 Gap size distributions

7.1.1 $P_{kMC}(a)$ measured from the kMC simulations

To determine P_{kMC} from kMC simulations, we collected datasets from a 100 kMC simulation runs (as described in Section 4.3) and averaged the results.

During each simulation run, after every nucleation event the position inside the gap (and capture zone) where the new nucleation happened is recorded. We also record the size of the gap that was fragmented, and the sizes of all the other gaps on the lattice: this way, we know how often are the largest gaps fragmented, how often the second largest etc. – we know the frequency of fragmenting a gap of a certain size rank.

The procedure is then as follows: during the simulation, each time a gap is fragmented, we check what was its size rank – if it was the largest gap on the lattice, we note that a gap of rank 1 ($R = 1$) was fragmented at the appropriate coverage, if it was the second largest we note ($R = 2$) was fragmented etc. At each fragmentation event, there is some total number of different sizes of gaps residing on the lattice; the smallest gap has the maximum rank at that timestep (kMC algorithm step), R_{max}. Therefore R_{max} is also a number of different sizes of gaps and it changes during the simulation.

At first, R_{max} grows rapidly – this is the initial phase: simulation starts with the empty lattice (equivalent to a single gap, so the first $R_{max} = 1$) and then the new nucleations increase the total number of (mainly) different gap sizes on the lattice, until a large pool of gaps of different sizes is created. Here R_{max} is at its peak; new nucleations will then slowly start to remove some of the present sizes of gaps (starting with the largest) so R_{max} will start to decrease. However, since at every simulation step a unique gap of a certain size can be fragmented into two gaps that have the exact sizes already present on the lattice (this reduces R_{max} by one and increases the overall number of gaps), R_{max} doesn't grow or decrease monotonically. The general trend can be seen on Figure 7.1 (left panel), where we show R_{max} as a function of the total number of islands on the lattice, n_{is}. We used a single run of the $i = 1$ case to plot it. For all the other cases of i the behaviour of R_{max} is qualitatively similar. Since coverage θ (not the here relevant n_{is}) is the measure of elapsed time, we also plot θ vs.

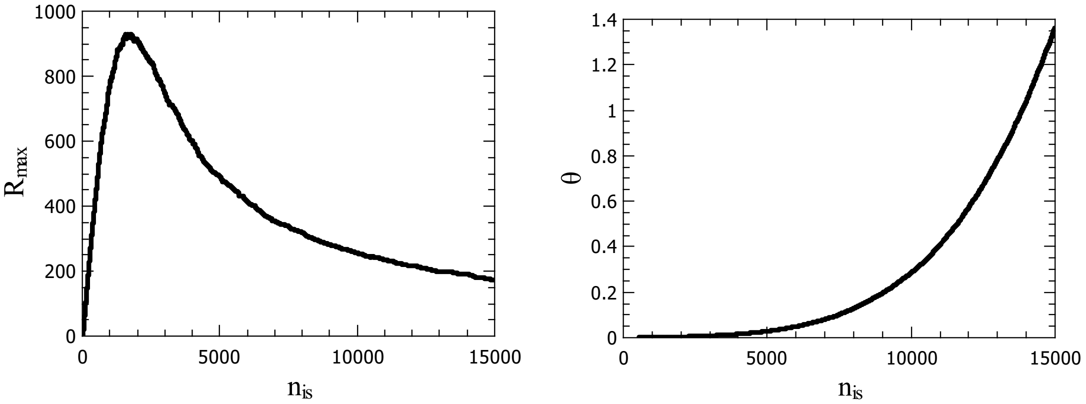

Figure 7.1: Left: R_{max} (number of different gap sizes on the lattice) vs. n_{is} (total number of islands), for $i = 1$, in a single kMC run.
Right: coverage θ vs. n_{is} for the same dataset.

n_{is} (Figure 7.1, right panel), for the same simulation run.

Coverage on which R_{max} starts to drop roughly corresponds to the onset of the scaling regime (the $P_{kMC}(a)$ measured at those coverages stabilizes and becomes coverage independent, for all the cases of i).

Since R_{max} varies, it can happen that in one nucleation event, a gap of rank (for example) $R = 5$ is fragmented, and at that timestep the total number of different gap sizes is $R_{max} = 300$. In another nucleation event, again a gap of rank $R = 5$ is fragmented, but at that timestep there are $R_{max} = 900$ different gap sizes. It is therefore necessary to scale the ranks of the fragmented gaps.

We divide the rank of the fragmented gap with the current R_{max}, to get a scaled set of ranks, $r = R/R_{max} \in [0, 1]$. Then we group these data sets within some coverage intervals corresponding to n_{is} intervals and make histograms of the scaled ranks r (we use a 100 runs and average the results). We use the same intervals to create $P_{kMC}(a)$ graphs which are shown on the right panels of Figures 7.2, 7.3 and 7.4 for $i = 0, 1$ and 2, respectively. The histograms that show the frequency of breaking gaps of some rank r (within a coverage interval) are normalized, giving the probability of fragmenting a gap of a certain size rank. These are shown on the left panels of Figures 7.2, 7.3 and 7.4. The intervals of n_{is} in which the data is grouped are chosen in such a way that

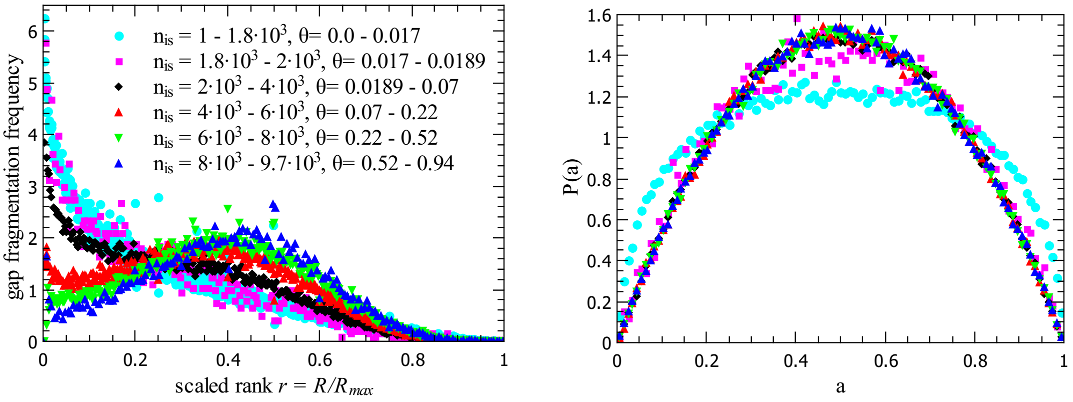

Figure 7.2: Left: frequency of fragmentation of gaps of certain (scaled) size ranks $r = R/R_{max}$ within intervals of total island numbers n_{is} (or the corresponding coverage intervals). Case of $i = 0$.
Right: $P_{kMC}(a)$ obtained from the same intervals, for $i = 0$.

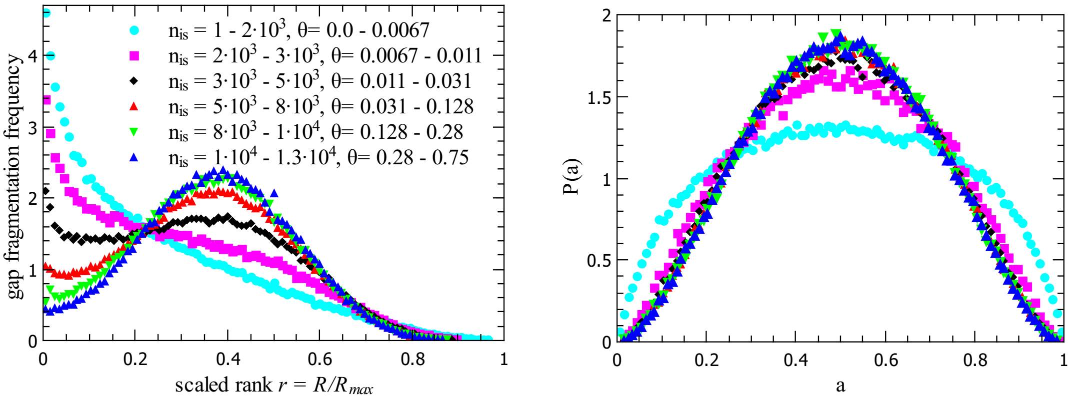

Figure 7.3: Left: frequency of fragmentation of gaps of certain (scaled) size ranks $r = R/R_{max}$ within intervals of total island numbers n_{is} (or the corresponding coverage intervals). Case of $i = 1$.
Right: $P_{kMC}(a)$ obtained from the same intervals, for $i = 1$.

(for every i) the first interval covers (roughly) the initial part with fast growing R_{max} (shown with light blue symbols on the graphs), the second interval contains the peak (pink) and the third interval (black symbols) has R_{max} steadily decreasing. All the higher intervals are within the scaling regime and are chosen arbitrarily.

We see that initially the vast majority of the gaps that get fragmented are the largest gaps, but this starts to change as coverage grows: initially the largest gaps were

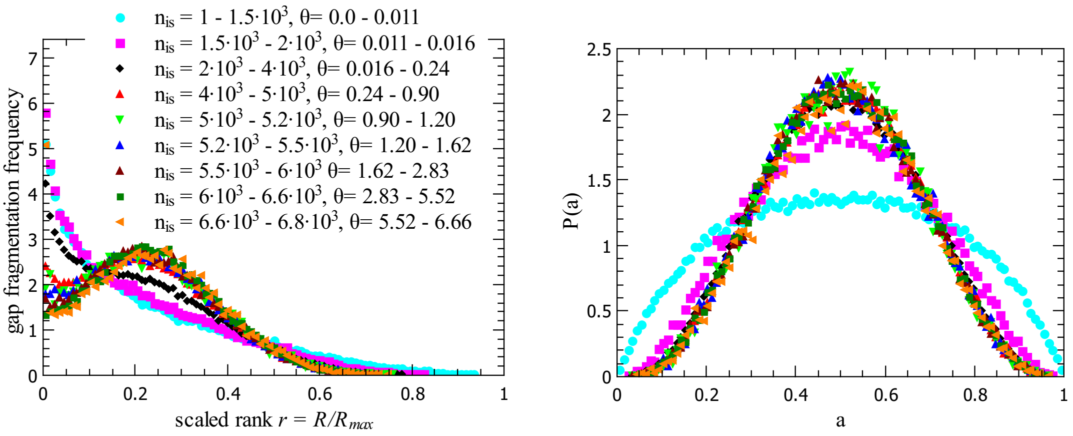

Figure 7.4: Left: frequency of fragmentation of gaps of certain (scaled) size ranks $r = R/R_{max}$ within intervals of total island numbers n_{is} (or the corresponding coverage intervals). Case of $i = 2$.
Right: $P_{kMC}(a)$ obtained from the same intervals, for $i = 2$.

being fragmented, but as time passed the large gaps got "used up" (but some small number of these large gaps remained) leaving a large pool of smaller gaps which then started to be fragmented at an increasing frequency. In order to observe this behaviour for $i = 2$, we had to run the simulations up to higher coverages; for a fixed coverage θ the total number of nucleations n_{is} decreases as i increases. Figure 7.5 shows θ vs. n_{is} plot for all i; there is a clear trend of decreasing n_{is} for $i = 1, 2$ and 3 but the case of $i = 0$ does not follow this rule; the algorithm for this case has a different rule for island nucleation (each monomer has the same probability of attaching irreversibly to the lattice). On Figure 7.6 we show only the $P_{kMC}(a)$ for $i = 3$ reaching steady state.

Right panels of Figures 7.2, 7.3, 7.4 and Figure 7.6 show (in black symbols) $P_{kMC}(a)$ entering the scaling regime at around $\theta = 0.0189$ for $i = 0$, $\theta = 0.011$ for $i = 1$, $\theta = 0.016$ for $i = 2$ and $\theta = 0.21$ for $i = 3$. The reason for such a large difference in θ for $i = 3$ case be seen on Figure 7.5. The scaling regime was found to start around $n_{is} \sim 2 \cdot 10^3$ for all the cases of i, and for $i = 3$ the coverage starts to grow rapidly just around this value of n_{is}.

The functional form of $P(a)$ is derived from the saturated monomer density n_1 (Eqn. (2.21)), which is obtained as a solution of the steady state ($\partial n_1/\partial t \simeq 0$) diffusion equation (Eqn. (2.20)). As shown with single gap simulations in Ref. [68], in very large

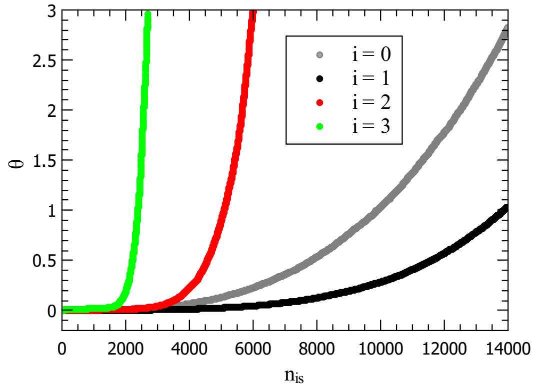

Figure 7.5: Coverage θ vs. total number of islands on the lattice n_{is} for $i = 0, 1, 2$ and 3.

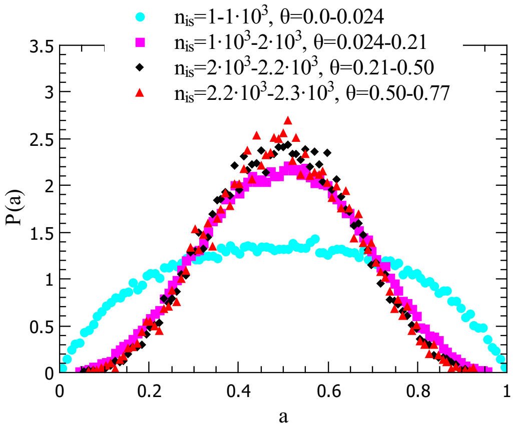

Figure 7.6: $P_{kMC}(a)$ for $i = 3$. In the third interval of n_{is} (θ) $P_{kMC}(a)$ has reached the scaling regime; R_{max} here decreases.

gaps nucleations are too frequent so the monomer densities don't have time to reach its saturated form. For different kMC simulation parameters we then expect to find different values of the gap size that behave as a threshold under which the monomer densities and $P(a)$ enter the steady state (scaling regime).

With $n_{is} = 2 \cdot 10^3$, an average gap on the lattice (we used a lattice with 10^6 sites) stretches across 500 lattice sites, which is here clearly sufficiently small to enter the scaling regime.

7.1.2 Comparison of $P(a)$ obtained from kMC simulations and as solutions of the inverse problem

With the scaling regime of $P_{kMC}(a)$ identified, we can compare it to the $P_F(a)$ obtained as a Fourier series representation of a solution of the inverse problem, and to the Tikhonov regularisation solution $P_\lambda(a)$. These are all shown on Figures 7.8, 7.10, 7.12 and 7.14, together with the diffusion ($\alpha = i + 1$) and deposition ($\alpha = i$) case of the model $P(a)$ given with:

$$P(a) = \frac{(2\alpha+1)!}{(\alpha!)^2} a^\alpha (1-a)^\alpha. \tag{7.1}$$

We also use P_{kMC} to solve the direct problem; that is, to integrate the IE form of the mean field DFPE $x \triangleq a(1+x)$:

$$\phi(x) = \int_0^{min(1,x)} \phi\left(\frac{x}{a} - 1\right) \frac{P(a)}{a} da. \tag{7.2}$$

The non-mean field DFPE, $x \triangleq a(x_1 + x_2)$, has an IE form (with a bias, Eqn. (3.21)):

$$\phi(x) = \int_0^1 \int_0^{x/a} \phi\left(\frac{x}{a} - x_1\right) \phi(x_1) P(a) \frac{x^{2\alpha+1}}{a^{2\alpha+2}} da dx_1, \tag{7.3}$$

where again $\alpha = i + 1$ or $\alpha = i$, depending on the mode of nucleation. In Figures 7.7, 7.9, 7.11 and 7.13 we show diffusion and deposition theoretical limits given with Eqn. (7.2) (where $P(a)$ is given by Eqn. (7.1)), the kMC obtained GSD (ϕ_{kMC}), the solutions of Eqn. (7.2) with $P = P_{kMC}(a)$ and also with P obtained as a solution of the inverse problem, $P = P_F$ and $P = P_\lambda$. Additionally, we show solutions of non-mean field Eqn. (7.3) with $P = P_{kMC}$, for both cases of α.

When looking at the inverse problem solutions P_F and P_λ, for the $i = 1$ and 2 cases (Figures 7.10 and 7.12) both the Fourier and the Tikhonov method gave good results, but in the $i = 2$ case we start to see the effect of increased noise in the input ϕ_{kMC} relative to the $i = 1$ case: P_λ is noticeably negative near $a = 1$. In the $i = 3$ case (Figure 7.14) the situation is even worse, so here Tikhonov solution is more of a guideline for the behaviour of the true $P(a)$. The case of $i = 0$ (Figure 7.8) is problematic for both methods, with the solutions slightly undershooting the true P_{kMC}.

In all of the cases of i we got better results with the Fourier reconstruction approach, which makes this a preferred method, especially if preservation of symmetry and $\|\cdot\|_1$ norm is required. The downside however is the relative difficulty of optimizing the method parameters (and their larger number); the Tikhonov method is perfectly adequate when a fast calculation is needed.

When we use P_{kMC} to integrate Eqn. (7.2), the resulting GSD (shown with empty squares in Figures 7.7, 7.9, 7.11 and 7.13) fits the kMC obtained GSD (ϕ_{kMC}) quite well for all the i cases, but it doesn't match it perfectly. Especially in the $i = 0$ and $i = 1$ case it is easy to see the limitations of the mean field approximation as the solutions of Eqn. (7.2) overshoot the peaks of the kMC data. Given the shortcomings of the mean field approximation, it is impossible to say to what extent the misalignment of the presented inverse problem solutions and the true P_{kMC} are a result of the mean field approximation itself, as opposed to being poorly calculated solutions of the ill posed problem.

Solutions of the non-mean field Eqn. (7.3) with P_{kMC} are also shown on Figures 7.7 - 7.13, both the $\alpha = i + 1$ (dark green line) and the $\alpha = i$ (orange line) case. As we already expect from the mean field model experience, the $\alpha = i + 1$ (corresponding to diffusion) case is a (here just slightly) better fit. The deposition case fails completely only in the $i = 0$ case; however the deposition limit we have been using makes little physical sense when applied to the $i = 0$ case.

The non-mean field solutions are a visible improvement to the mean field approximation in all the cases of i. However, the (relative) simplicity and the possibility of calculating P from a known GSD are the unique features of the mean field DFPE model.

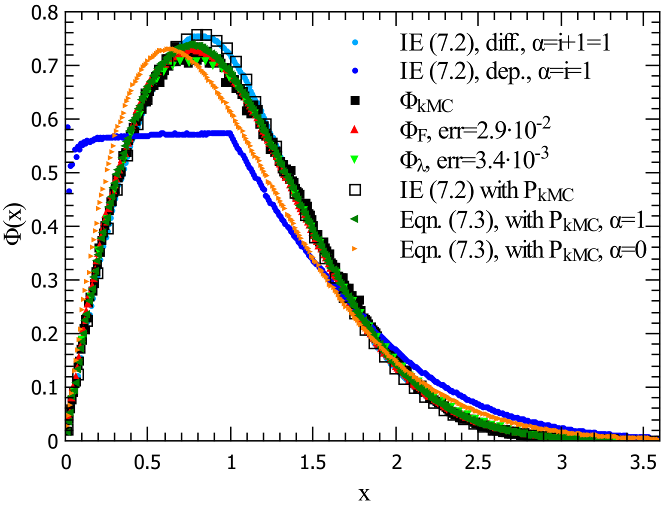

Figure 7.7: Case $i = 0$: Solutions of the IE (7.2) with P given by diffusion and deposition case of Eqn. (7.1) (light and dark blue), ϕ_F and ϕ_λ shown red and light green (Eqn. (7.2) where we use the inverse problem solutions P_F and P_λ; mean square errors (relative to ϕ_{kMC} are listed) and ϕ_{kMC} (black). Shown with the solutions of IE (7.2) with P_{kMC} (empty black squares) and of the non-mean field Eqn. (7.3) (dark green for $\alpha = i + 1$ and orange for $\alpha = i$).

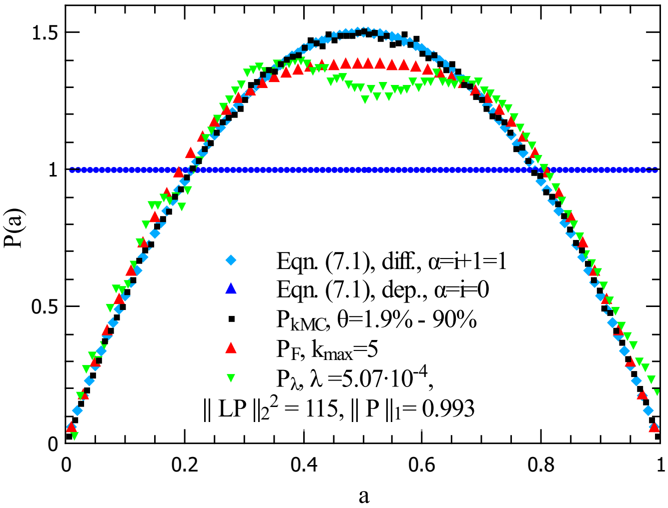

Figure 7.8: Case $i = 0$: Diffusion and deposition case of Eqn. (7.1) (light and dark blue), P_{kMC} (black) and the inverse problem solutions: P_F in red (Fourier reconstructed, with the maximum wave number k_{max}) and P_λ in light green (Tikhonov solution, the squared $\| \cdot \|_2$ norm of the regularisation term LP_λ and the $\| \cdot \|_1$ norm of P_λ are listed).

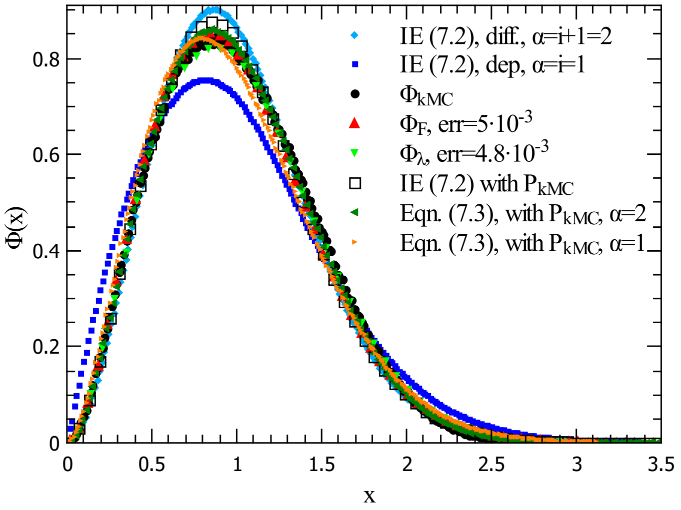

Figure 7.9: Case $i = 1$: Solutions of the IE (7.2) with P given by diffusion and deposition case of Eqn. (7.1) (light and dark blue), ϕ_F and ϕ_λ shown red and light green (Eqn. (7.2) where we use the inverse problem solutions P_F and P_λ; mean square errors (relative to ϕ_{kMC} are listed) and ϕ_{kMC} (black). Shown with the solutions of IE (7.2) with P_{kMC} (empty black squares) and of the non-mean field Eqn. (7.3) (dark green for $\alpha = i + 1$ and orange for $\alpha = i$).

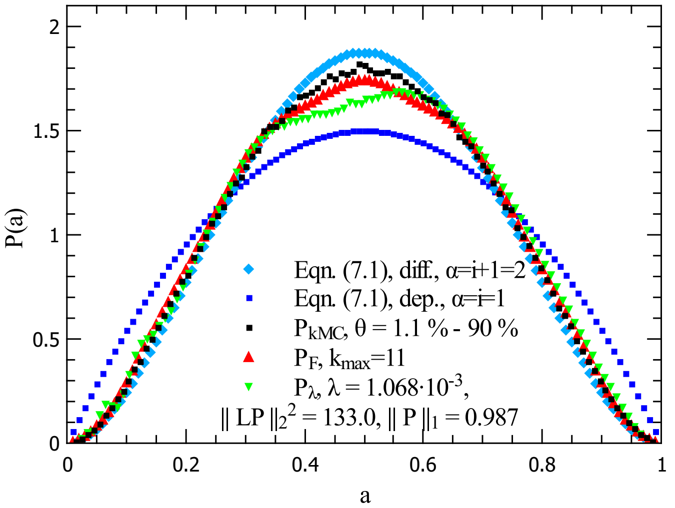

Figure 7.10: Case $i = 1$: Diffusion and deposition case of Eqn. (7.1) (light and dark blue), P_{kMC} (black) and the inverse problem solutions: P_F in red (Fourier reconstructed, with the maximum wave number k_{max}) and P_λ in light green (Tikhonov solution, the squared $\|\cdot\|_2$ norm of the regularisation term LP_λ and the $\|\cdot\|_1$ norm of P_λ are listed).

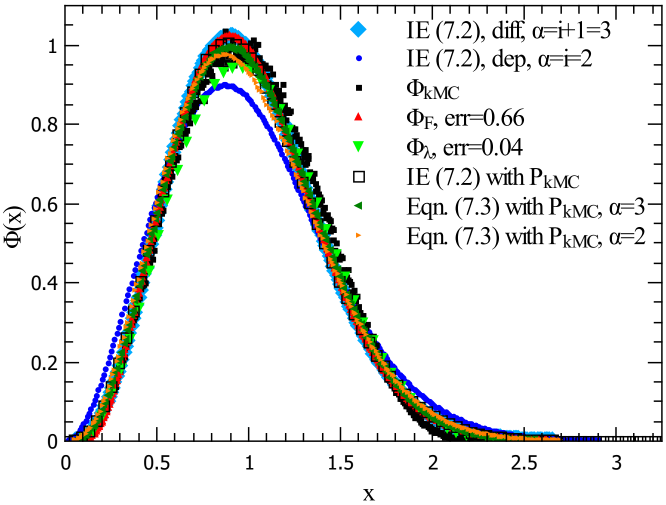

Figure 7.11: Case $i = 2$: Solutions of the IE (7.2) with P given by diffusion and deposition case of Eqn. (7.1) (light and dark blue), ϕ_F and ϕ_λ shown red and light green (Eqn. (7.2) where we use the inverse problem solutions P_F and P_λ; mean square errors (relative to ϕ_{kMC} are listed) and ϕ_{kMC} (black). Shown with the solutions of IE (7.2) with P_{kMC} (empty black squares) and of the non-mean field Eqn. (7.3) (dark green for $\alpha = i + 1$ and orange for $\alpha = i$).

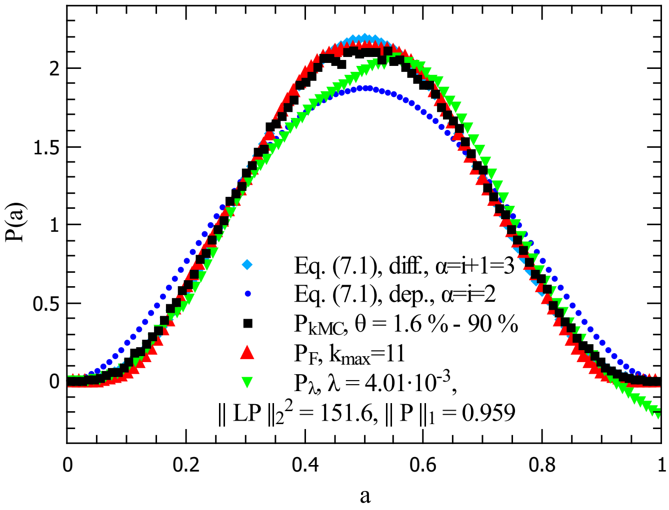

Figure 7.12: Case $i = 2$: Diffusion and deposition case of Eqn. (7.1) (light and dark blue), P_{kMC} (black) and the inverse problem solutions: P_F in red (Fourier reconstructed, with the maximum wave number k_{max}) and P_λ in light green (Tikhonov solution, the squared $\| \cdot \|_2$ norm of the regularisation term LP_λ and the $\| \cdot \|_1$ norm of P_λ are listed).

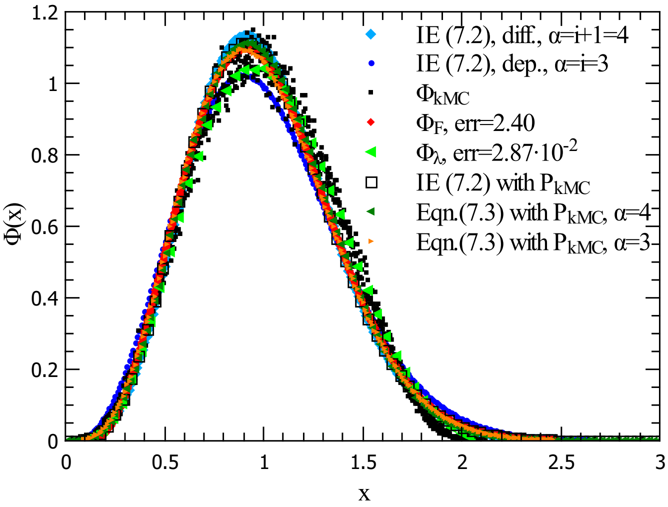

Figure 7.13: Case $i = 3$: Solutions of the IE (7.2) with P given by diffusion and deposition case of Eqn. (7.1) (light and dark blue), ϕ_F and ϕ_λ shown red and light green (Eqn. (7.2) where we use the inverse problem solutions P_F and P_λ; mean square errors (relative to ϕ_{kMC} are listed) and ϕ_{kMC} (black). Shown with the solutions of IE (7.2) with P_{kMC} (empty black squares) and of the non-mean field Eqn. (7.3) (dark green for $\alpha = i + 1$ and orange for $\alpha = i$).

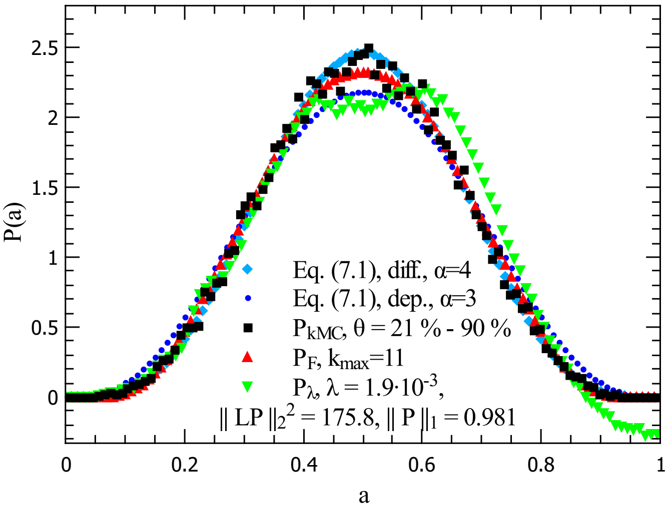

Figure 7.14: Case $i = 3$: Diffusion and deposition case of Eqn. (7.1) (light and dark blue), P_{kMC} (black) and the inverse problem solutions: P_F in red (Fourier reconstructed, with the maximum wave number k_{max}) and P_λ in light green (Tikhonov solution, the squared $\|\cdot\|_2$ norm of the regularisation term LP_λ and the $\|\cdot\|_1$ norm of P_λ are listed).

Since we assume that the realistic processes, modelled with the kMC simulations, are a mixture of the diffusion and deposition driven nucleation, we can quantify the level of those contribution for different i. We first express P_{kMC} and ϕ_{kMC} as a convex combination of the diffusion and deposition cases of Eqn. (7.1) and (7.2) (light and dark blue curves on the previous graphs):

$$P_{kMC} = \beta P^{diffusion}_{\alpha=i+1} + (1-\beta) P^{deposition}_{\alpha=i}, \tag{7.4}$$

$$\phi_{kMC} = \gamma \phi^{diffusion}_{\alpha=i+1} + (1-\gamma) \phi^{deposition}_{\alpha=i}. \tag{7.5}$$

Now the parameters β and γ can be calculated with the least squares method (we did this in MATLAB). We show the results in Table 7.1. There is no trend with i or a symmetry between β and γ, but given the limitations of the mean field model and the numerical noise in the kMC data that is not surprising. From the results we can only safely conclude that diffusion is the dominant mechanism of island nucleation.

i	β	γ
0	$0.998 \pm 2.654 \cdot 10^{-3}$	0.912 ± 0.005
1	$0.821 \pm 6.887 \cdot 10^{-3}$	0.728 ± 0.010
2	0.819 ± 0.015	1.015 ± 0.018
3	$0.844 \pm 4.300 \cdot 10^{-2}$	0.714 ± 0.020

Table 7.1: Results of fitting kMC results according to Eqns. (7.4) and (7.5).

7.2 Capture zone distributions

The $P_z(a_z)$ used in the IE for the CZD is a distribution of the random variable $a_z = \frac{1}{2}(a_1 + a_2)$, where a_1 and a_2 are drawn independently from the $P(a)$ for the gaps, Eqn. (7.1). P_z defined in such a way is a mathematical construct that cannot be measured, so we can here only compare the Fourier and Tikhonov solution for P_z.

7.2.1 Comparison of $P_z(a_z)$ obtained as solutions of the inverse problem

The IE we use to model the CZD has the same form as Eqn. (7.2);

$$\phi_z(z) = \int_0^{min(1,z)} \phi\left(\frac{z}{a_z} - 1\right) \frac{P_z(a_z)}{a_z} da_z, \tag{7.6}$$

and a_z is sampled as $\frac{1}{2}(a_1 + a_2)$, with a_1 and a_2 drawn from the diffusion and deposition case of Eqn. (7.1).

The CZD can also be obtained (or, more precisely put, modelled) as a convolution of GSD:

$$\phi_z(z) = 2\int_0^{2z} \phi(y)\phi(2z - y)dy. \tag{7.7}$$

We use the same color coding on the CZD graphs as we did on the equivalent GSD graphs. The diffusion and deposition case of (7.6) are shown in light and dark blue, respectively, on the right panels of Figures 7.15, 7.16, 7.17 and 7.15 ($i = 0, 1, 2$ and 3). Solutions of IE (7.6) with $P_z = P_{z,\lambda}$ and $P_z = P_{z,F}$ are plotted green and red respectively, on the left panels. Again we list the mean square errors (difference between $\phi_{z,\lambda\backslash F}$ and $\phi_{z,kMC}$. The norm $\|P_{z,\lambda}\|_1$ shows the deviation of the Tikhonov solution from the expected normalized distribution, and the squared norm of the regularisation term $\|LP_{z,\lambda}\|_2^2$ is the value from the corresponding L-curve. Additionally, we show the result of integrating the kMC GSD (ϕ_{kMC}) according to Eqn. (7.7) in pink.

Since we don't have a kMC obtained P_z to check against, we can only say that the Fourier reconstruction works better because it is always positive (the Tikhonov

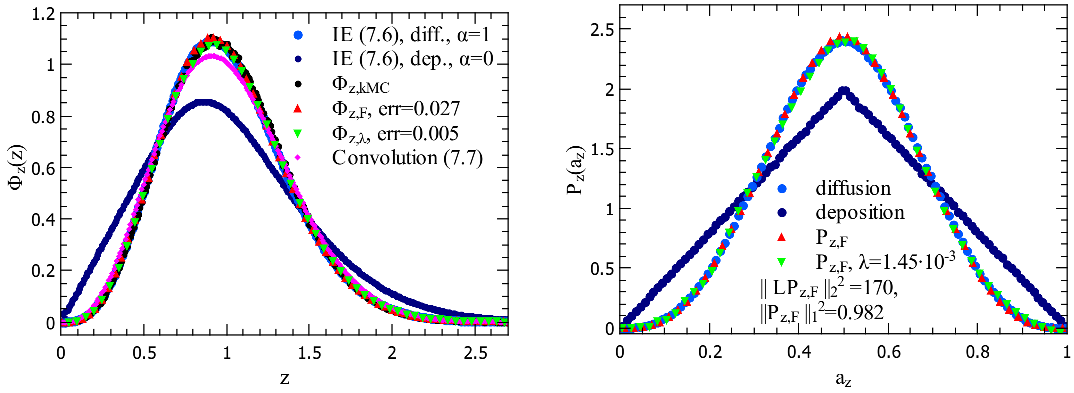

Figure 7.15: case $i = 0$. Left: Diffusion (light blue) and deposition (dark blue) cases of the IE (7.6) (where $P_z(a_z)$ is created by drawing from $P(a)$ (Eqn. (7.1)) for the gaps), $\phi_{z,F}$ (red) and $\phi_{z,\lambda}$ (green) calculated from the IE (7.6) with $P_{z,F}$ and $P_{z,\lambda}$. Their errors are relative to the kMC obtained $\phi_{z,kMC}$ (black). Convolution of the GSD ϕ_{kMC} (Eqn. (7.7)) is plotted pink.
Right: Diffusion and deposition $P_z(a_z)$ (drawn from Eqn. (7.1)) in light and dark blue. Inverse problem solutions $P_{z,F}$ (Fourier reconstructed, plotted red; with $k_{max} = 11$) and $P_{z,\lambda}$ (Tikhonov solution, in green, with the value of λ and the norms listed).

solutions for all $i > 0$ fall slightly below 0 near $a_z = 1$), and it is always symmetric. Those problems aside, both look very similar, lie on top of the diffusion curve for $i = 0, 1$ and overshoot it for $i = 2, 3$. This could be partly due to the mean field approximation failure (we have so far seen that it tends to overestimate the peak).

The solutions of the convolution (7.7) however fall short of the true ϕ_{kMC} in all the cases of i (pink curves on the right panels), pointing to some correlation between the neighbouring gaps. Since the assumption that there is no correlation between the gaps is also weaved into the model DFPE for the CZD, this also affects the solutions. The convolution of the GSD seems to underestimate the $\phi_{z,kMC}$ roughly by the same amount for all the cases of i, so the effects of correlation would act as a sort of a systematic error in the DFPE model.

In conclusion, we have in this chapter presented evidence in favour of the DFPE model, by comparing the inverse problem solutions and the kMC measured P_{kMC} for

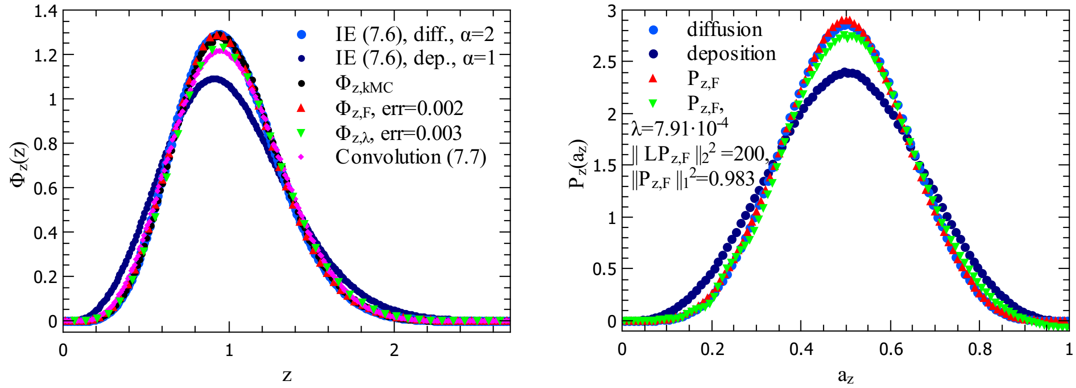

Figure 7.16: case $i = 1$. Left: Diffusion (light blue) and deposition (dark blue) cases of the IE (7.6) (where $P_z(a_z)$ is created by drawing from $P(a)$ (Eqn. (7.1)) for the gaps), $\phi_{z,F}$ (red) and $\phi_{z,\lambda}$ (green) calculated from the IE (7.6) with $P_{z,F}$ and $P_{z,\lambda}$. Their errors are relative to the kMC obtained $\phi_{z,kMC}$ (black). Convolution of the GSD ϕ_{kMC} (Eqn. (7.7)) is plotted pink.
Right: Diffusion and deposition $P_z(a_z)$ (drawn from Eqn. (7.1)) in light and dark blue. Inverse problem solutions $P_{z,F}$ (Fourier reconstructed, plotted red; with $k_{max} = 11$) and $P_{z,\lambda}$ (Tikhonov solution, in green, with the value of λ and the norms listed).

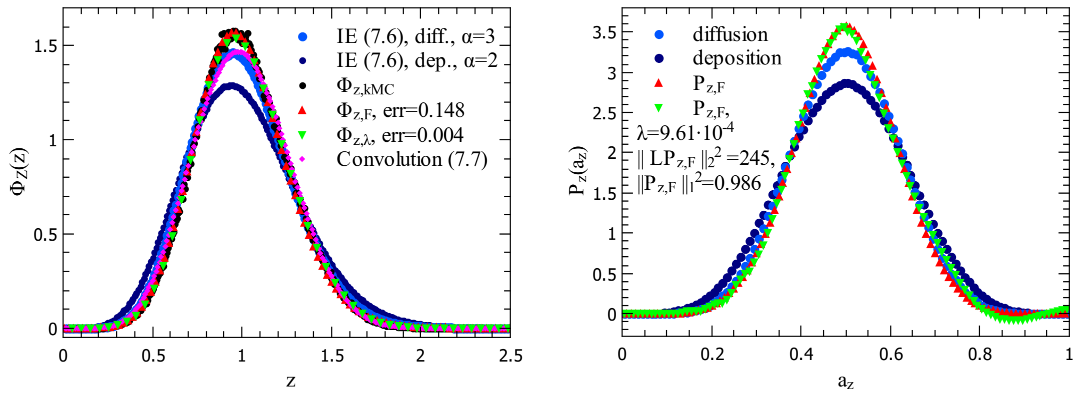

Figure 7.17: case $i = 2$. Left: Diffusion (light blue) and deposition (dark blue) cases of the IE (7.6) (where $P_z(a_z)$ is created by drawing from $P(a)$ (Eqn. (7.1)) for the gaps), $\phi_{z,F}$ (red) and $\phi_{z,\lambda}$ (green) calculated from the IE (7.6) with $P_{z,F}$ and $P_{z,\lambda}$. Their errors are relative to the kMC obtained $\phi_{z,kMC}$ (black). Convolution of the GSD ϕ_{kMC} (Eqn. (7.7)) is plotted pink.
Right: Diffusion and deposition $P_z(a_z)$ (drawn from Eqn. (7.1)) in light and dark blue. Inverse problem solutions $P_{z,F}$ (Fourier reconstructed, plotted red; with $k_{max} = 11$) and $P_{z,\lambda}$ (Tikhonov solution, in green, with the value of λ and the norms listed).

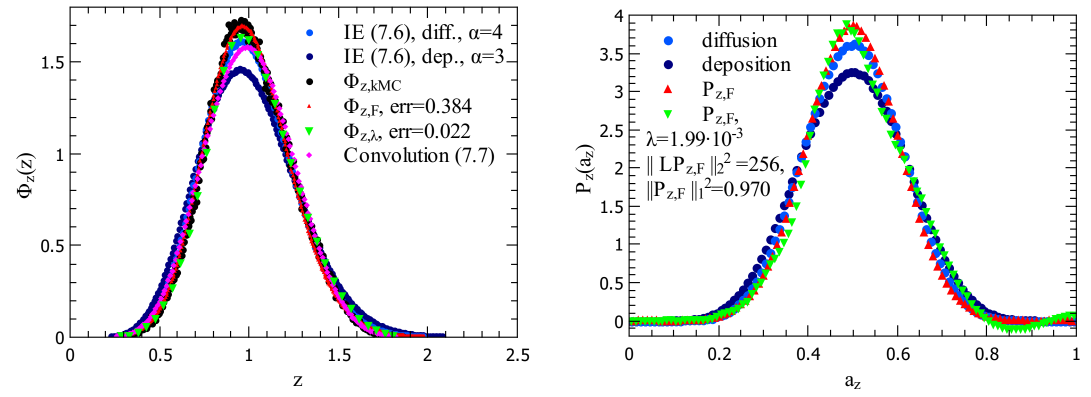

Figure 7.18: case $i = 3$. Left: Diffusion (light blue) and deposition (dark blue) cases of the IE (7.6) (where $P_z(a_z)$ is created by drawing from $P(a)$ (Eqn. (7.1)) for the gaps), $\phi_{z,F}$ (red) and $\phi_{z,\lambda}$ (green) calculated from the IE (7.6) with $P_{z,F}$ and $P_{z,\lambda}$. Their errors are relative to the kMC obtained $\phi_{z,kMC}$ (black). Convolution of the GSD ϕ_{kMC} (Eqn. (7.7)) is plotted pink.
Right: Diffusion and deposition $P_z(a_z)$ (drawn from Eqn. (7.1)) in light and dark blue. Inverse problem solutions $P_{z,F}$ (Fourier reconstructed, plotted red; with $k_{max} = 11$) and $P_{z,\lambda}$ (Tikhonov solution, in green, with the value of λ and the norms listed).

the gaps. We found that the diffusion driven nucleation is the dominant one, with deposition driven nucleation making only a small contribution.

However, this is all we can say: the limitations of the mean field approximation do not allow for any other (stronger) conclusions: checking both the GSD and the associated P graphs independently, we found no trend in diffusion-to-deposition contributions with increasing i.

When using the measured P_{kMC} in the non-mean field DFPE for the gaps, we saw a small improvement in the fit of the resulting ϕ to the kMC GSD, but the non-mean field DFPE is not suitable for the task of calculating P via the inverse problem.

In the case of the capture zones, there is no way of directly observing the distribution $P_z(a_z)$. Because of that, we just presented the best inverse problem solutions from the two approaches, the Tikhonov regularisation and the Fourier reconstruction. We found they both look very similar, but they also slightly overshoot the theoretical predictions, pointing again to the limitations of the mean field approximation.

The reasoning and the procedure of collecting data from the kMC simulations which gave P_{kMC} lead us to measure a similar fragmentation distribution for the capture zones, one that isn't related to the $P_z(a_z)$. In the rest of the thesis we will explore and build on it, leaving $P_z(a_z)$ behind.

Chapter 8

Alternative DFPE for the CZD

We have stated in the previous chapter that $P_z(a_z)$, defined as the probability distribution of the random variable $a_z = \frac{1}{2}(a_1 + a_2)$ where a_1, a_2 are drawn from $P(a)$ for the gaps, cannot be measured. However, a probability distribution defined in another way can be measured in the process of fragmenting capture zones, let us call it $Q(a)$, to be defined below, with the random variable $a \in [0, 1]$. A DFPE, slightly different than the one we have used so far, can be constructed for it. The driving motivation is simple: if it is possible to construct a DFPE model for capture zones with measurable fragmentation probability, we could extend it to two dimensions more easily. We could not only have a way to check the validity of the model as we did for the gaps (comparison of inverse solutions and P_{kMC}) but also it would be a model that doesn't rely on the concept of gaps - a concept that doesn't naturally extend to 2d.

A notation remark: the kMC obtained Q should be called Q_{kMC} for the notation to be consistent with the one used for gaps. However, since the kMC measured Q is the only one we have, we will omit the subscript $_{kMC}$. This will come handy in Chapter 9 as it simplifies the notation.

We will begin this chapter by introducing the capture zone fragmentation probability distribution $Q(a)$. Then, in Section 8.2, we construct a DFPE for it, by taking a retrospective approach that traces the evolution of the reduced (fragmented) zone size; similarly to the DFPE for the gaps we have been using up until now.

In Section 8.3 we will, instead of focusing on the fragmented, old zone, look at the newly created one and, by considering its evolution steps, redefine $Q(a)$ so that it reflects them. Using this redefined Q, we will write an alternative model equation for the CZD and test its results against the kMC obtained CZD.

8.1 $Q(a)$ measured from the kMC simulations

To calculate this new distribution $Q(a)$, we use the results of the same 100 simulation runs (and average over them) which we used in Chapter 7 to calculate P_{kMC} for the gaps.

The capture zones, just like the gaps, fragment with island nucleations. On Figure 8.1 we show the schematics of capture zones after a new island nucleated and the Voronoi network is updated. Initially, we had two islands (black circles) with capture zone sizes Z_1' and Z_2'. Then the new island nucleated (red circle) and the third zone was formed (of the size $Z = dZ_1 + dZ_2$) by taking areas dZ_1, dZ_2 from the older two, leaving them with the reduced sizes Z_1 and Z_2.

Now we can define a_1:

$$a_1 = \frac{Z_1}{Z_1'} = \frac{\text{reduced zone size (post new nucleation)}}{\text{original size}}, \tag{8.1}$$

and similarly $a_2 = Z_2/Z_2'$. We can then construct $Q(a)$ as a histogram of a, within the desired coverage interval.

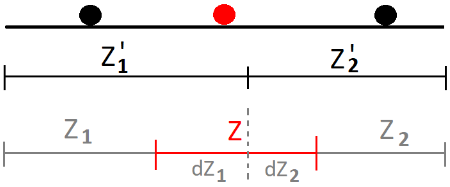

Figure 8.1: Schematics of capture zones after a new nucleation. Originally there were two islands (black circles) with zones Z_1' and Z_2' (upper bar). After a new island nucleated (red circle), a third zone was created, $Z = dZ_1 + dZ_2$ (marked red).

When processing the kMC data, we used the actual zone sizes (in units of lattice

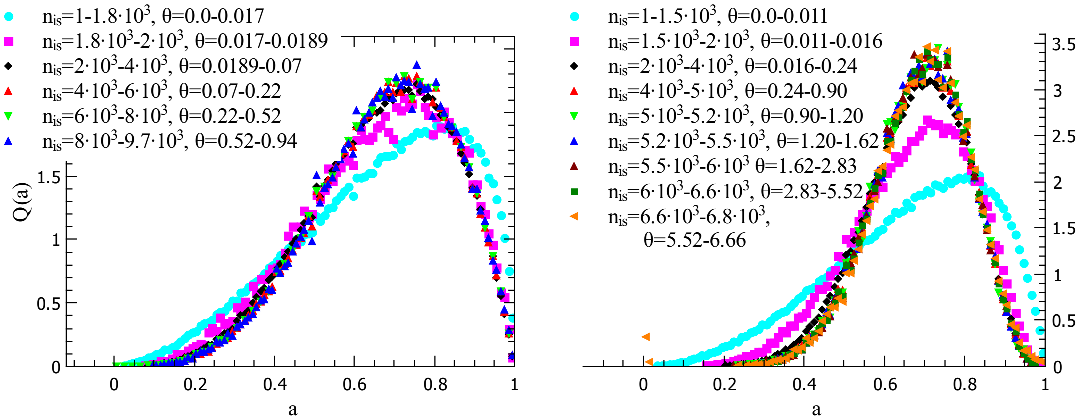

Figure 8.2: Left: $i = 0$ case. $Q(a)$ measured in intervals of the total island size n_{is} (corresponding to coverage θ intervals); the intervals match those of Figures 7.2, 7.3, 7.4 and the color coding is the same.
Right: $Q(a)$ for the $i = 2$ case.

spacings) in (8.1). In theory, using zone sizes scaled to the average is equivalent, but it would introduce (more) rounding errors.

In Figure 8.2 we show $Q(a)$ for $i = 0$ and $i = 2$ reaching the scaling regime. The data sets are taken from the same intervals of total island numbers n_{is} (corresponding to coverages) which we used in section 7.1.1 (for gap ranks and P_{kMC}), and we used the same color coding. $Q(a)$ enters the scaling regime around $n_{is} \sim 2 \cdot 10^3$ just as P_{kMC} did.

8.2 DFPE for $Q(a)$

With $Q(a)$ sampled from the data in the scaling regime, we can construct a DFPE for the CZD with the same logic as in the GSD case.

Looking at the capture zones schematics in Figure 8.1, we can say that the reduced zone of size Z_1 was created when an older zone of size $Z_1 + dZ_1$ was cut at a position $a_1 = Z_1/(Z_1 + dZ_1)$. At the same time Z_2 was created by cutting $Z_2 + dZ_2$ at the proportion $a_2 = Z_2/(Z_2 + dZ_2)$.

The new island's zone (marked red) is of the size $Z = dZ_1 + dZ_2$. If we assume that, on average, $dZ_1 = dZ_2 = Z/2$, we have (on average) $Z_1 = a(Z_1 + Z/2)$ (and $Z_1 = a(Z_1 + Z/2)$). Then we employ the mean field assumption where we set the new zone size Z to 1. By denoting the reduced zone sizes (Z_1, Z_2) by z, we can write the DFPE:

$$z \triangleq a\left(z+\frac{1}{2}\right). \tag{8.2}$$

If we denote the distribution of z as $\psi(z)$, the corresponding Integral Equation form is:

$$\psi(z)=\int_0^{min(2z,1)} \psi\left(\frac{z}{a}-\frac{1}{2}\right)\frac{Q(a)}{a}da. \tag{8.3}$$

The geometric considerations behind this DFPE demand that the average value of a is $\langle a\rangle = 2/3$. Then, if the average new zone size is 1 (red in Figure 8.1), the average reduced zone size will also be 1. In Table 8.1 we show $\langle a\rangle$ and average sizes of new and reduced zones; the zone sizes are not scaled to the average (like z in Eqn. 8.2 is) but are instead measured in lattice spacings. Then the underlying assumption of the DFPE demand that they are identical, however we see that the new zone sizes are always a little smaller. This discrepancy grows with i, so this DFPE might not give a good fit for very high i, although without the kMC data for $i > 3$ we cannot say for which (if any). The intervals of n_{is} in which we collect the data grow smaller as i increases (fewer nucleation events for high i) so getting enough data points for $i > 3$ cases would be problematic.

	$i=0$	$i=1$	$i=2$	$i=3$
data from n_{is} interval:	$(2-9.7)\times10^3$	$(3-13)\times10^3$	$(2-5)\times10^3$	$(2-2.3)\times10^3$
corresponding to θ:	(1.89 - 94)%	(1.1 - 75)%	(1.6 - 90)%	(2.1 - 77)%
$\langle a\rangle$	0.67290	0.68169	0.68266	0.68614
avg. new zone size	182.8	121.0	255.4	373.9
avg. reduced zone size	190.1	130.9	277.9	417.8
$\frac{\text{avg. new size}}{\text{avg. reduced size}}$	0.962	0.924	0.919	0.895

Table 8.1: Average values of a, the new zone sizes (marked red on Figure 8.1) and the reduced zone sizes (marked gray), within the chosen n_{is} intervals for collection of data (these are representative of the scaling regime).

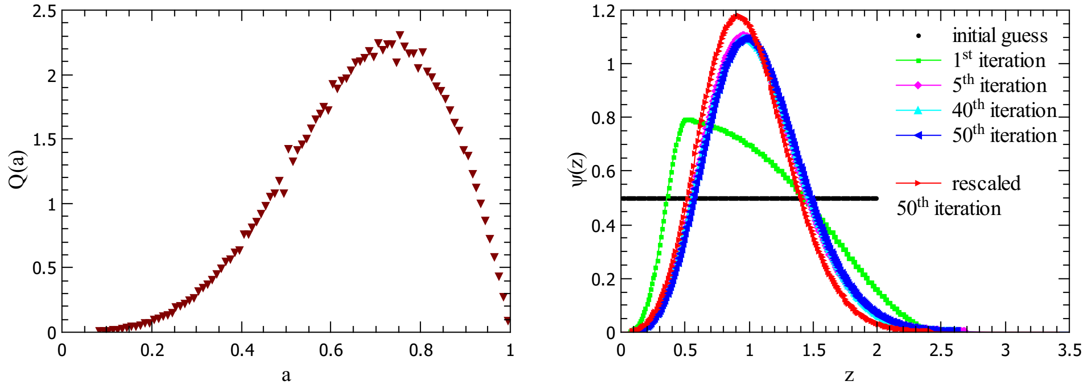

Figure 8.3: Left: $i = 0$ case of $Q(a)$, measured in the interval listed in Table 8.1. Right: ψ iterations from IE (8.3), starting with the initial rectangular guess (plotted black). The 50th iteration (red) is rescaled to 1 (plotted).

8.2.1 DFPE model results

Since the values of $\langle a \rangle$ shown in Table 8.1 aren't exactly 2/3, when inserting them to DFPE (8.2) we get $\langle z \rangle$ slightly different from 1. For $i = 0$ we have $\langle z \rangle = 1.029$ and for the worst case, $i = 3$, we have $\langle z \rangle = 1.093$. Since these are still small deviations, we can treat them as they were a result of numerical noise and simply rescale the result of integrating IE (8.3) so that $\psi(z)$ has a mean of 1.

With a given $Q(a)$, IE (8.3) is solved iteratively as usual; for the $i = 0$ case on the left panel of Figure 8.3 we show the convergence of ψ (for $Q(a)$ shown on the right panel) and the rescaled final result.

For all of the subsequent cases of i we use 50 iterations and rescale the resulting ψ.

In the left panels of Figures 8.4, 8.5, 8.6 and 8.7 we show $Q(a)$ for $i = 0, 1, 2$ and 3, respectively. The intervals of n_{is} (and θ) from which we gathered data are the ones listed in Table 8.1. In the right panels we show the kMC CZD and both scaled and unscaled $\psi(z)$ (Eqn. (8.3) with Q from the left panels).

In all of the cases the (scaled) solution ψ over-represents the average sizes (overshoots kMC CZD around $z = 1$), and therefore under-represents the small amd large sizes. This is the usual ailment of the mean field approximation, but the model can still be of use (at least for small values of i) if precision isn't the main concern. To

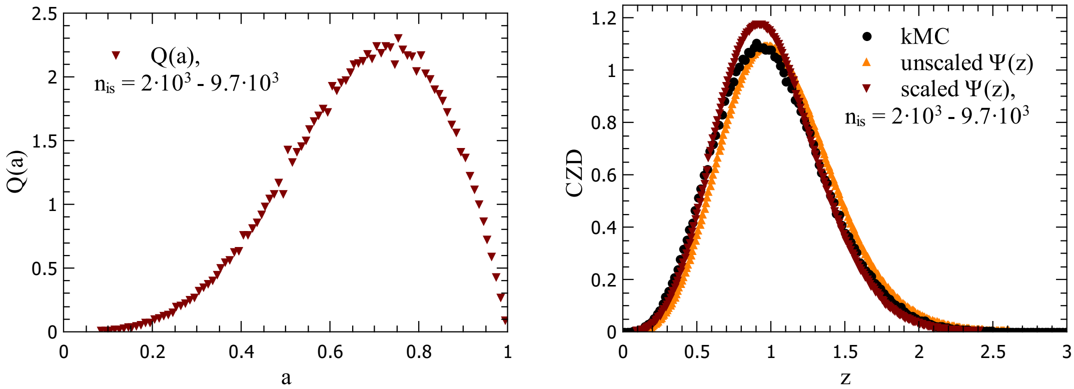

Figure 8.4: $i = 0$ case. Left: $Q(a)$ from the kMC simulations.
Right: ψ from IE (8.3), unscaled and scaled, shown with the kMC CZD (black).

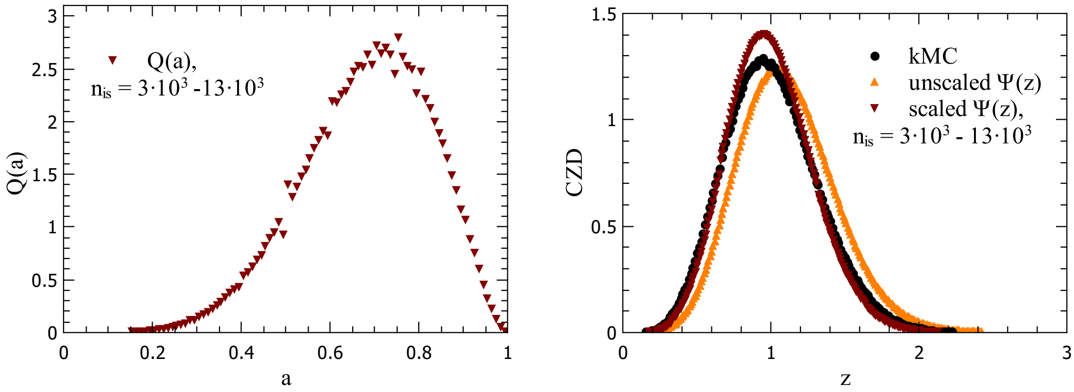

Figure 8.5: $i = 1$ case. Left: $Q(a)$ from the kMC simulations.
Right: ψ from IE (8.3), unscaled and scaled, shown with the kMC CZD (black).

that end, in Figure 8.9 we show the results of finding $Q(a)$ from a known ψ_{kMC}, for the example case of $i = 1$; the inverse problem solved with the Tikhonov regularisation (the L - curve is shown on Figure 8.8) will not give the exact shape of kMC measured $Q(a)$ but it will display it's general behaviour correctly.

If time restraints permitted, we could introduce factors into the DFPE (8.2) that account for the difference between the new and the old, reduced zone (which would fix the difference between the measured $\langle a \rangle$ and the predicted 2/3), but those would be numerical improvements that depend on directly measured values which are only

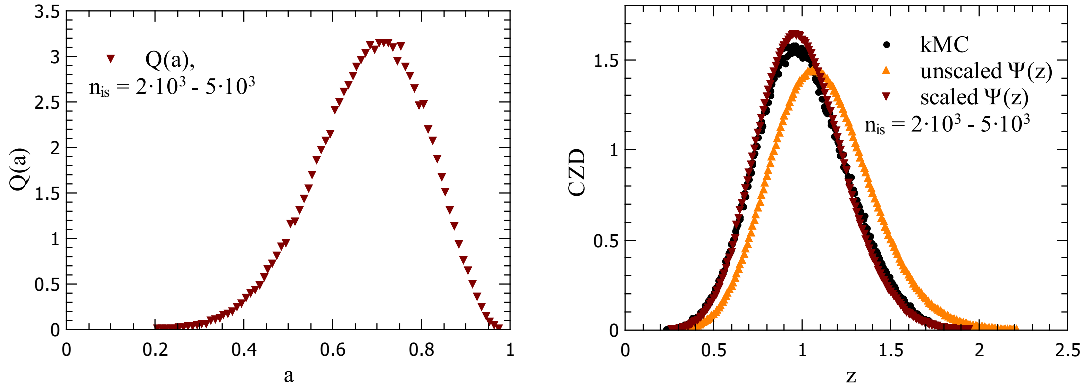

Figure 8.6: $i = 2$ case. Left: $Q(a)$ from the kMC simulations.
Right: ψ from IE (8.3), unscaled and scaled, shown with the kMC CZD (black).

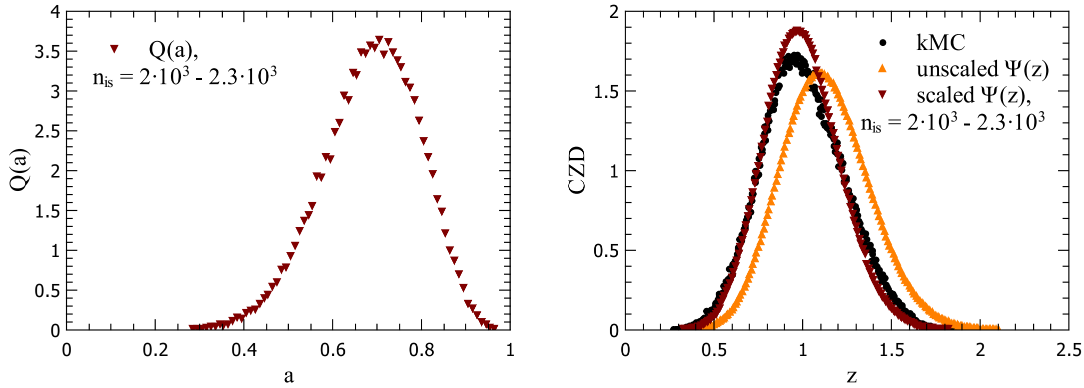

Figure 8.7: $i = 3$ case. Left: $Q(a)$ from the kMC simulations.
Right: ψ from IE (8.3), unscaled and scaled, shown with the kMC CZD (black).

available in simulations.

Since the model DFPE we proposed here doesn't rely on any specific knowledge of the system (only $Q(a)$ or the CZD), and its predictions at least aren't far off, it is more beneficial to look into other aspects of the zone fragmentation from the scheme 8.1 and test this model in two dimensions.

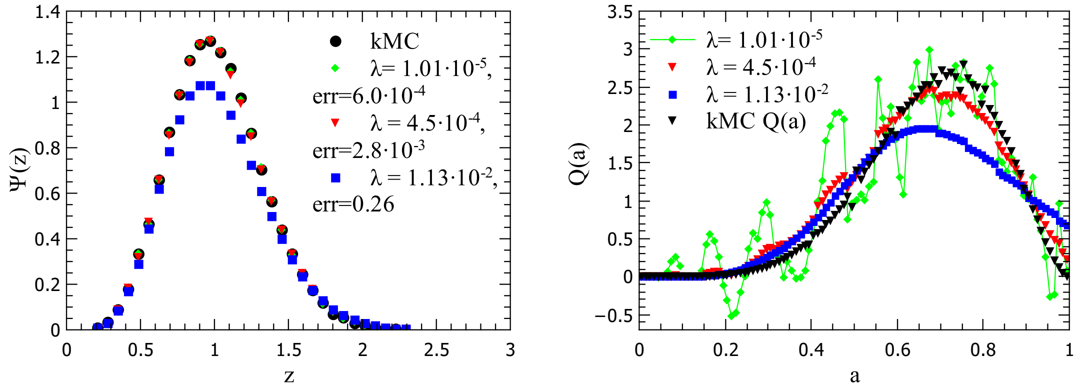

Figure 8.9: $i = 1$ case. Left: the kMC CZD used to calculate the Tikhonov solutions Q_λ (in black), and ψ_λ corresponding to those Q_λ.
Right: the solutions Q_λ for 3 valus of λ shown with kMC $Q(a)$ (in black).

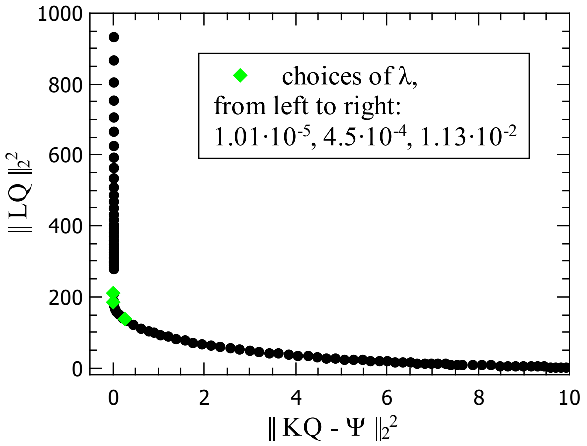

Figure 8.8: L - curve for calculating Q_λ from the kMC CZD, $i = 1$

8.3 The newly created capture zones: an alternative model equation

We have so far been concentrating on the fragmentation and size reduction of the old capture zone, while setting the newly created one to 1. If we now look at the new zone on the schematics 8.1, we can backtrace its evolution in a similar way.

The new zone has been born by taking a portion of the old zone to its left and another portion from the old zone to its right; $Z = dZ_1 + dZ_2$ from Figure 8.1. In this process, we would define the variable a as:

$$a = \frac{\text{piece of the old zone taken by the new zone}}{\text{original old zone size}}, \tag{8.4}$$

so in our example we would have measured two values of a, $a_1 = dZ_1/(Z_1 + dZ_1)$ and $a_2 = dZ_1/(Z_1 + dZ_1)$. The equation governing such a sampling of zones is:

$$z \triangleq \frac{1}{2\langle a\rangle}(a_1 z_1 + a_2 z_2), \tag{8.5}$$

where z is the scaled size of newly created zones, z_1, z_2 of the old, fractured ones and since all of the zones have been created by fragmenting older ones, z, z_1 and z_2 are all drawn from the same distribution. There is no reason for having a preferred direction on the lattice, so a_1 and a_2 (measuring the left and right zone fragmentation) are also drawn from the same distribution, let us call it Q^{new}. $Q^{new}(a)$ defined in this way is just a symmetric image of the old Q around 0.5.

We can also make a mean field version of Eqn. (8.5) by setting $z_1 = z_2 = 1$:

$$z \triangleq \frac{1}{2\langle a\rangle}(a_1 + a_2). \tag{8.6}$$

The distribution of the zone sizes z given by Eqn. (8.6) is easily calculated by randomly drawing values of a_1 and a_2 from the interval $[0, 1]$ with the probability $Q^{new}(a)$, adding them to get a set of values of z and then binning z. The algorithm is similar to the one in section 4.1.

The resulting distributions are shown on Figures 8.10 and 8.11 for all 4 cases of i, along with the kMC CZD. We also show the scaled distribution $\psi(z)$ from IE (8.3); which for all the cases except for $i = 2$ gives a worse fit to the kMC data. We can probably look for reasons for this in the fact that Eqn. (8.6) is a simpler model that only assumes we can set the old zone sizes to 1; IE (8.3) additionally assumes the two older zones contribute (on average) equally to the newly created zone. The selling point of the IE (8.3) is that we have an established way of finding Q from a kMC CZD

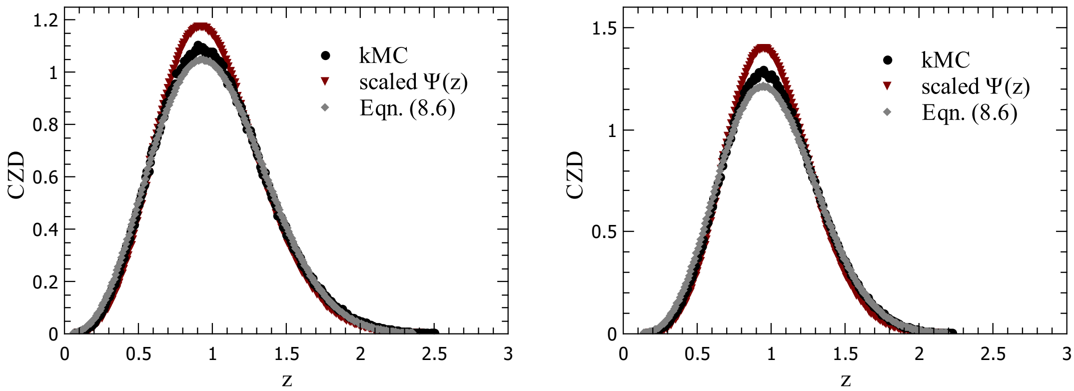

Figure 8.10: Left: $i = 0$ case: CZD shown with scaled $\psi(z)$ (Eqn. (8.3)) and the distribution of z from Eqn. (8.6).
Right: $i = 1$ case.

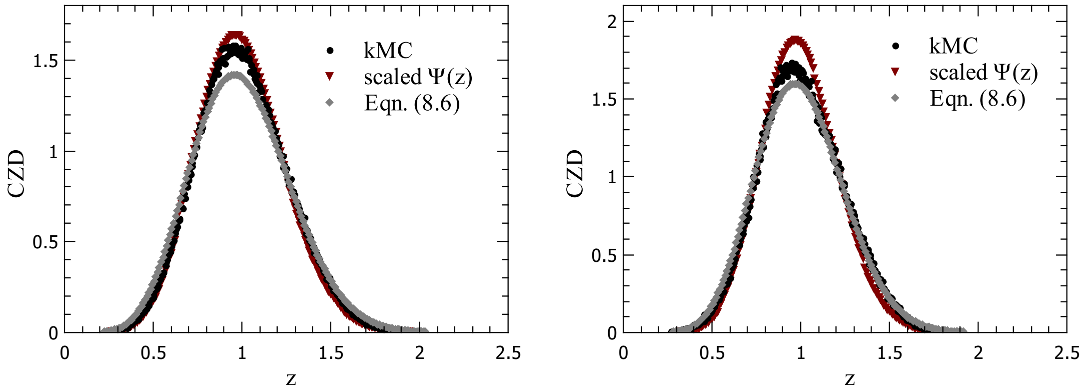

Figure 8.11: Left: $i = 2$ case: CZD shown with scaled $\psi(z)$ (Eqn. (8.3)) and the distribution of z from Eqn. (8.6).
Right: $i = 3$.

through it, which might equivalently be used in two dimensions.

8.3.1 The GSD connection

One additional result can be drawn from Q^{new}: if we look again at the schematics on Figure 8.1, we can guess that the next island which will presumably nucleate later, in the gap between the new (red) island and the old (black) island to the left, will most likely nucleate half way between them - which is where the gray Z_1 and the red Z marked zones meet. The same is most likely to happen on the right hand side: an island nucleation on the edge of Z and Z_2 zone. This makes the zone portions dZ_1 and dZ_2 equal to the new gap sizes x_1, x_2, so we can sample the GSD from Q^{new} as:

$$x \triangleq \frac{a}{\langle a \rangle}, \tag{8.7}$$

where x is the scaled gap size and a is defined as (8.4) and drawn from Q^{new} (the symmetric image of $Q(a)$). In other words, $Q^{new}(a)$ is the rescaled GSD (with a mean of $\langle a \rangle \approx 1/3$; as shown previously in Table 8.1 where the average a drifted slightly from the expected 2/3).

We stress here that this result comes entirely as a geometric property of the capture zones which are defined as Voronoi cells around island centres on a 1d lattice, and the parabolic nucleation probability within a gap (Eqn. (2.28)). The data from which we created Q as a histogram only records the exact positions of the Voronoi cell edges, which then correspond to probabilities of new island positions and gap sizes; but not the actual position of some subsequent island.

With a given by Eqn. (8.7), Eqn. (8.6) becomes:

$$z \triangleq \frac{1}{2}\left(x_1 + x_2\right), \tag{8.8}$$

which is in fact the convolution (2.23) from Ref. [15] we have been using previously (the derivation of the convolution equation (2.23) from Eqn. (8.8) is as the one in the Appendix A, if we set $\eta = a = 1$ and $z \to 2z$).

In the left panel of Figure 8.12 we show $Q(a)$ and $Q^{new}(a)$ for $i = 1$, and on the right panel the kMC GSD and Q^{new} which is rescaled so that its mean is 1 (this matches the distribution of x given by Eqn. 8.7).

For the $i = 2$ case shown on Figure 8.13, we sampled x from the Q^{new} according to Eqn. (8.7).

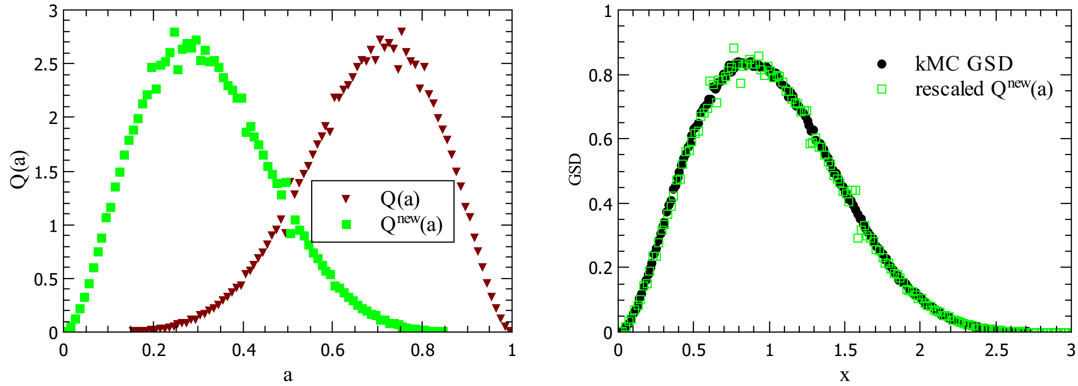

Figure 8.12: $i = 1$ case. Left: $Q(a)$ and $Q^{new}(a)$.
Right: kMC GSD and the rescaled Q^{new}.

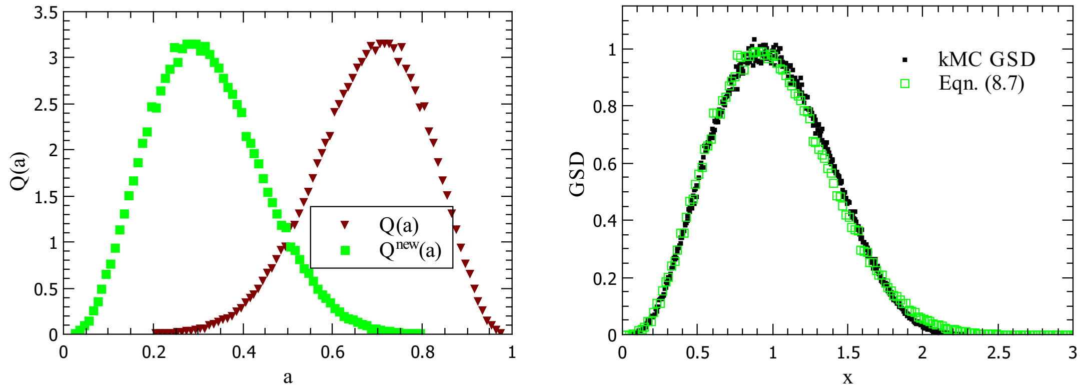

Figure 8.13: $i = 2$ case. Left: $Q(a)$ and $Q^{new}(a)$.
Right: GSD sampled from Q^{new} according to Eqn. (8.7).

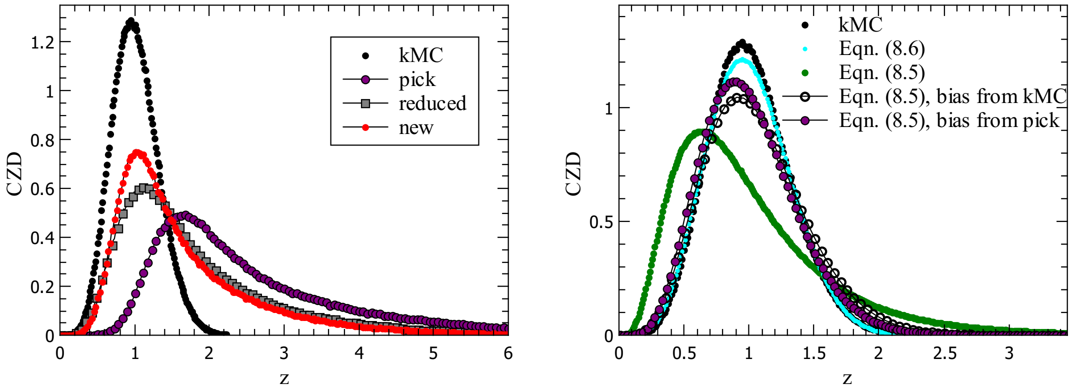

Figure 8.14: $i = 1$ case. Left: kMC CZD (black), measured distribution of zones that got fragmented (purple), distribution of newly created zones (red) and of the reduced (old) ones (gray), all scaled to average size on the lattice.
Right: kMC CZD (black) and the mean - field sampling of the new zones (Eqn. (8.6)). CZD sampled from Q^{new} according to non - mean field Eqn. (8.5) is shown in pink. Biased Eqn. (8.5), where kMC CZD (black on the left panel) is used as a bias, is plotted in empty black squares; and the one where the bias is the measured distribution of fragmented zones (purple from the left panel) is plotted purple.

8.3.2 Non - mean field equation

Equation (8.5) doesn't set z_1, z_2 to 1, which we would then expect to be more accurate, although introducing two more variables increases the chance for errors.

We again use the same procedure as in section 4.1: the algorithm defines an initially empty set (array) of zone sizes and then proceeds to fill it with individually chosen values $z = (a_1z_1 + a_2z_2)/2$, where a_1 and a_2 are randomly drawn from Q^{new} and z_1, z_2 are randomly drawn from the array of zone sizes z. In that way, the system forgets its initial conditions (first z value set to 1) and builds a set of z values that satisfy Eqn. (8.5).

The result of this procedure is shown on Figure 8.14, right panel, in pink. We can see that it is completely different from the kMC CZD (plotted black): much like the non - mean field integral equation for the gap sizes from section 3.3, the process of choosing z_1, z_2 values needs to take into account that the zones in which a new island nucleates are not chosen randomly; they are usually larger than the average ones.

On the left panel of Figure 8.14, those chosen zones are shown in purple, along with the usual kMC CZD (statistics made from all of the zone sizes on the whole lattice). The reduced zone sizes (post nucleation) which were marked gray on our schematics 8.1, are here again plotted in gray. The newly created zone sizes are again plotted in red, and all of the datasets are scaled to the average zone size of the whole lattice.

We can now introduce a bias to Eqn. (8.5): choosing z_1, z_2 with the same probability like in kMC simulation (purple distribution on the left panel of Figure 8.14) should have given a better fit to the kMC CZD than the mean - field equation did; however the result was much worse. It is not clear why this happened. Certainly, introducing a more sophisticated description, with more variables, increases the amount of possible numerical errors; but such a large difference probably points to a deeper issue. With a bias we introduced, z_1 and z_2 are still drawn independently of each other, and in the mean field version setting them both to 1 relates them, in a very brute manner. This might account for, at least a part, of the problem.

To summarize, in this chapter we have defined a fragmentation probability distribution $Q(a)$ (and its symmetric image Q^{new}) for capture zones, measurable from kMC. We have used it in two ways to get CZD: first, by focusing on the old, reduced zone size (post-fragmentation), a DFPE for the capture zones can be identified, equivalent to the DFPE for the gaps. This approach, while giving rough results, also gives promise for an extension to two dimensions where a similar DFPE can be written. Then, if the model is good, it can be used to calculate Q from a known (kMC obtained) CZD by solving the inverse problem, just as we did in Chapters 5 and 6.

A second approach, one that looks at the evolution of the newly created zone, allowed us to sample the CZD according to the alternative model equation. The associated fragmentation probability, Q^{new}, is just a symmetric image of Q. This model gives a better fit to the kMC CZD, but it is not clear if an extension of this equation to two dimensions would still allow for Q^{new} to be calculated from a known CZD.

Chapter 9

Two dimensional substrate: DFPE for the CZD

One of the appeals of the DFPE model (namely, Eqn. (3.16)) has been the possibility of an easy extension to 2d: the lengths of the capture zones z from 1d would become the areas of the zones in 2d, and then an equation such as $z \triangleq a_z(z+1)$ would allow us to determine the correct P_z from the kMC CZD.

While it is certainly possible to calculate such a P_z from kMC CZD with the methods from Chapter 6 and 5 (the resulting P_λ has in fact a parabolic shape similar to the 1d cases of P_z), it wouldn't correspond to any physical (measurable) quantity. In the 1d case, P_z was sampled by drawing from the corresponding P for the gaps, so it was defined through the gaps. However, in 2d it is not clear what an inter - island gap would be.

On the other hand, capture zones have the same straightforward definition in all dimensions, and since in the previous chapter we developed a DFPE for the CZD that relies entirely on capture zones and measurable fragmentation probability Q, we will in this chapter test if that model can be extended to 2d.

This chapter is structured as follows: first we explain the two-dimensional kMC simulation procedure. Then, in Section 9.2, we will define $Q(a)$ and, looking at a zone fragmentation and size reduction on a 2d substrate, write model mean field DFPEs for the CZD analogous to the one in the previous chapter. In Section 9.3 we attempt to refine the (over-simplified) model equation so that it encapsulates the complexities present in a 2d problem. Finally, we will try out the alternative model equation which focuses on the newly created zone using Q^{new} in Section 9.4.

9.1 The kMC simulation on a 2d lattice

In 2d simulations, we use an extended, circular island model. The dynamics are otherwise the same as in the 1d case with point islands: starting on an empty lattice, deposition steps (monomer placed on a random site) are followed by a certain number of diffusion steps (randomly chosen free monomers on the lattice moved by one space in a random direction; up, down, left or right).

A monomer will hop 16 times on average between two deposition events, which (with the lattice size of 1000 × 1000) gives the ratio $R = D/F = 0.25 \times 16 \times 1000 \times 1000 = 4 \times 10^6$. We again use periodic boundary conditions and run the simulation until the desired coverage is achieved.

When $n_{mon} = i+1$ monomers collide, an island nucleates and its position is recorded as the single lattice site - this is the island's centre. Island's size n_{mon} is also recorded. Then, assuming the island is a perfect circle, an effective radius is calculated: $r^2 = n_{mon}/\pi$. If another monomer finds itself in a lattice position whose distance from the island's position (centre) is equal to or less than r, it will be absorbed and island's size and radius r will be incremented.

Capture zones are defined as Voronoi cells around island centres, so they don't change when islands grow; only when a new nucleation occurs. At higher coverages, coalescence of two islands can happen without the Voronoi network registering it. For low coverages, before the coalescence effects start to be relevant (which happens around $\theta \sim 20-30\%$ [16]), we don't expect the choice of generating cells around island's centres rather than around their edges will have a significant impact.

With this algorithm, the resulting structure (islands and Voronoi network) looks like the one shown in Section 2.4 (Figure 2.3).

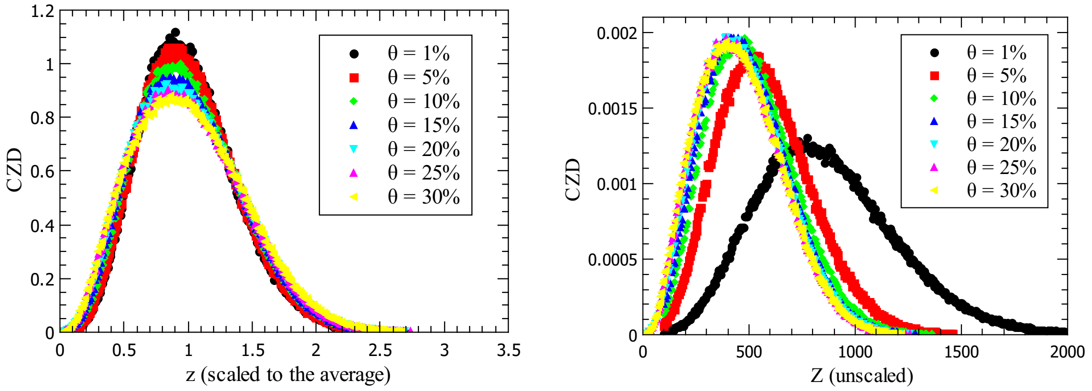

Figure 9.1: Left: kMC obtained CZDs for i=1, scaled to the average zone size at a given coverage. Right: unscaled CZDs.

To get the CZD and $Q(a)$ we used a diffusion to deposition ratio $R = 4 \cdot 10^6$ and averaged outputs of 300 runs.

When plotting CZDs for $i = 1$ for different coverages (Figure 9.1), it is apparent that the scaling is not perfect (for the $i = 2$ case, Figure 9.2, it looks much better). Usually the scaling regime, in terms of R, is found to start around $R = 10^5$ and improves as R grows. In terms of coverage, it starts at $\theta \approx R^{-1/2}$ and ends between 10 and 30 % [16], yet here we see scaled curves within that region slightly sliding down as coverage rises. As a larger contrast to the equivalent 1d case, the unscaled CZD curves within that region are very similar. This makes it difficult to choose the coverage at which it is best to gather data for $Q(a)$; it is unclear how big of an effect this will have on goodness of fit of model equations to the kMC data.

Initially there is a large surge of new nucleations (making the $\theta = 1\%$ and $\theta = 5\%$ CZD distinct from subsequent ones), after which we enter into an imperfect scaling regime. After some higher coverage (dependant on i), new nucleations become so rare it is impossible to collect enough data for constructing $Q(a)$. The CZD curves here overlap each other perfectly (both the ones scaled to the average and the unscaled) - here the Voronoi cells remain more or less unchanged. Therefore the coverages at which the data is collected are chosen roughly between those two extremes:

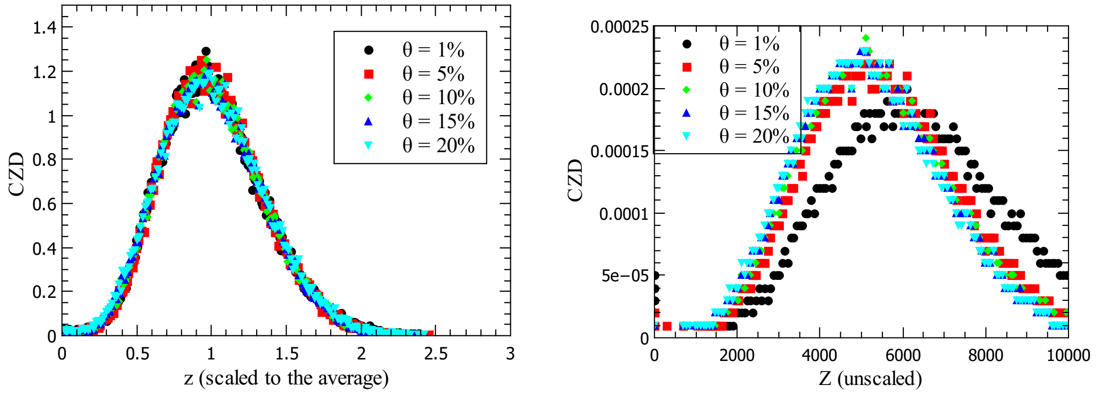

Figure 9.2: Left: kMC obtained CZDs for i=2, scaled to the average zone size at a given coverage. Right: unscaled CZDs.

for $i = 2$ $Q(a)$ is constructed from the data collected between $\theta = 5\%$ and 10 %, for $i = 1$ between $\theta = 10\%$ and 25 %.

9.2 Method: extension of 1d DFPE

Following the same approach as in one-dimensional capture zones, we measure $Q(a)$ from kMC simulations and attempt to construct a similar DFPE for the CZD.

Like before in the 1d case, we define a as the ratio of the reduced Voronoi cell size and its original size: the cell area after a new island nucleated in its vicinity and took away a portion of it, and the original cell area prior to nucleation. Reflecting the difficulty of choosing an appropriate coverage interval based on the CZD behaviour, there is very little difference between $Q(a)$ in the early stage and the one measured in what we believe to be the scaling regime (Figure 9.3).

Whenever a new island nucleates, the areas of the capture zones that are affected are recorded and Voronoi network is updated. The size of the newly created zone size is recorded, along with the areas that zone took away from the old zones. The total number of zones that were reduced is recorded. This is sketched on Figure 9.4. Here, after a new island nucleated, the updated Voronoi network has a new cell drawn in red. Its area is $dZ1 + dZ2 + dZ3$. Three old zones (coloured grey) were reduced in size (from initial $Z1 + dZ1$ to final $Z1$) and the values of a collected are then $a = Z1/(Z1 + dZ1)$,

$a = Z2/(Z2 + dZ2)$ and $a = Z3/(Z3 + dZ3)$.

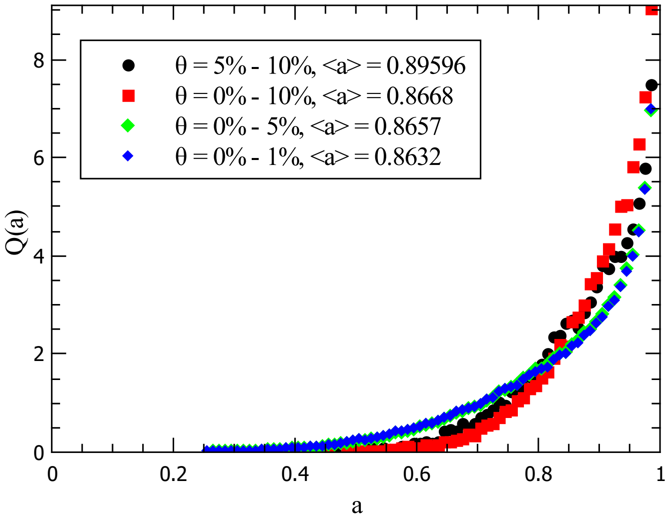

Figure 9.3: $Q(a)$ for $i = 2$, measured in different intervals of coverage θ.

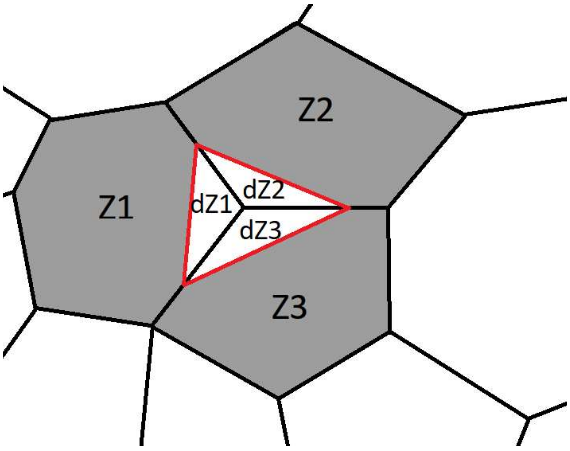

Figure 9.4: Schematics of capture zones after nucleation.

In the model we're testing, the grey area (reduced zone) Z1 was created when a larger, older zone of area Z1+dZ1 was sliced at a proportion a. In other words: a larger, old zone consisting of the reduced zone Z1, and, on average, a third of the new zone (dZ1), was reduced to a times its original size. With the mean field approximation of taking the newly created zone's area to be 1, DFPE that describes this process is

$$z \triangleq a(z + \frac{1}{3}) \tag{9.1}$$

However, a new island will not always break three old capture zones, so instead of 3 in the equation we need to use the average number of broken cells ξ, which varies with coverage and critical island size i. It is averaged over all of the nucleation events within the dataset from which we construct $Q(a)$.

For $i = 1$ and $\theta \in [0.1, 0.25]$ we then have $\xi = 4.7084$ and the average value of a is $\langle a \rangle = 0.909$ (similar to $\xi = 5.5$ found in [60], where point island model, $i = 1$, $R = 10^7$ and $\theta = 10\%$ are used).

For $i = 2$ and $\theta \in [0.05, 0.1]$ it is $\xi = 6.10633$ and the average a is $\langle a \rangle = 0.896$.

With these values alone, the average zone size from Equation (9.1) is slightly larger than 1. Another correction we need to make is to the average size of the newly created zones: new zones are usually smaller than the old ones they fragment. Referring to the schematics on Figure 9.4, newly created (red) zone is smaller than the grey coloured reduced old zones by some factor χ. When collecting all of the corresponding red and grey areas in nucleations occurring within specified coverages for $i = 1, 2$, we get $\chi =$ average of new zone area / average of old, reduced zones.

For $i = 1$, we have $\chi = 0.452$ and for $i = 2$, $\chi = 0.675$, within their respective coverage intervals.

Figure 9.5 (left panel) shows the distribution of newly created cells ψ^{new} (red cell on scheme 9.4) and the reduced old ones $\psi^{reduced}$ (gray Z sizes), together with the distribution of original old zone sizes Z+dZ (distribution of cells that will be fragmented in new nucleations, ψ^{pick}) and the total CZD on the lattice. All are scaled to the average cell size on the lattice at a given coverage. When new cells are scaled to the average new cell size and reduced to the average reduced size, they overlap (right panel).

Now, with introduced $\eta = \frac{\chi}{\xi}$, the DFPE (9.1) becomes:

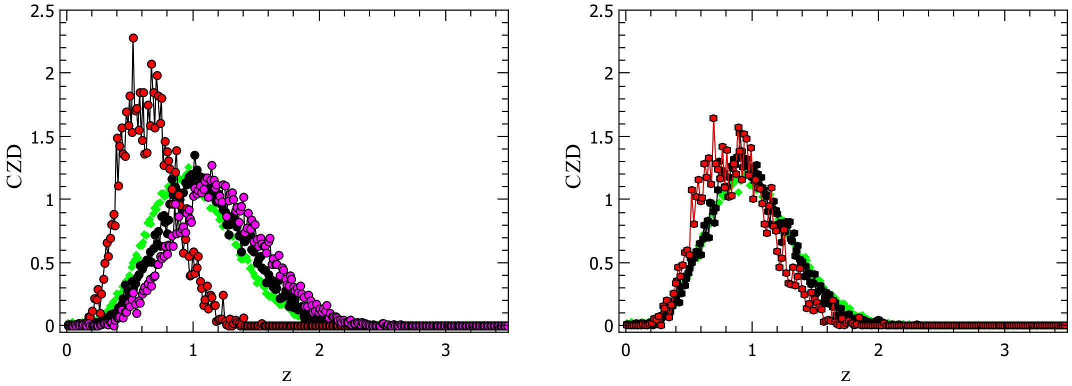

Figure 9.5: Left: CZDs for $i = 2$, all scaled to the average size on the lattice at $\theta = 10\%$. Pink: ψ^{pick}, zones to be fragmented in new nucleations, black: $\psi^{reduced}$, the same zones after they were reduced in size to create a new zone, red: ψ^{new}, newly created zones. The standard kMC CZD (all the zones on the lattice at $\theta = 10\%$) is shown in green. Right: CZDs with zones scaled to their own averages.

$$z \triangleq a(z + \eta). \tag{9.2}$$

Average zone size from this equation is now 0.995 for both cases of i. The corresponding integral equation is:

$$\psi(z) = \int_0^{min(z/\eta,1)} \psi\left(\frac{z}{a} - \eta\right) \frac{Q(a)}{a} da. \tag{9.3}$$

Figure 9.6 shows the solution to the IE for $i = 2$, with the corresponding IE where χ is taken to be 1 for comparison. Both solutions were rescaled to 1 after integrating.

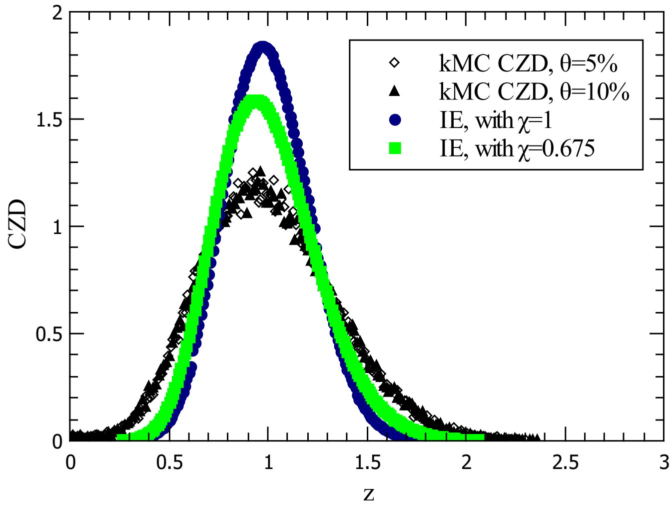

Figure 9.6: Solutions of IE (9.3) for $i = 2$, on top of kMC CZD (plotted black).

Since the DFPE with a single capture zone variable isn't a good fit, we try out a version with two variables:

$$z \triangleq a(z_1 + \eta z_2), \tag{9.4}$$

where we still have $\eta = \chi/\xi = 0.452/4.708$ for $i = 1$ and $0.675/6.106$ for $i = 2$.

The corresponding integral equation is:

$$\psi(z) = \int_{a=0}^{a=1} \int_{z_1=0}^{z_1=z/a} \psi\left(\frac{z}{\eta a} - \frac{z_1}{\eta}\right) \psi(z_1) \frac{Q(a)}{\eta a} dz_1 da, \tag{9.5}$$

and we again solve it iteratively. However, the results are hardly an improvement; they are shown on Figures 9.9 and 9.11 for $i = 1$ and $i = 2$, respectively.

Because the number of cells fractured by a new nucleation is quite high but some of them will only lose a very small proportion of their areas to the new cell, we can assume only 3 cells contribute and the rest are negligible. Figure 9.7 shows individual $Q(a)$ distributions: in each nucleation, all of the fractured zones give a value of a and those are then ordered from the smallest a_1 to the largest a_N and binned to obtain Q_{01}, Q_{02},... ,Q_{07} (Q_{07} contains data from seventh and all of the higher chipped zones). When collecting data only from the three zones that contributed the most to the new one (have the smallest values of a) and neglecting all the rest, we can construct a distribution $Q(a)$ that corresponds to the scheme on Figure 9.4; call it $Q_3(a)$. We collect 3 values of a per nucleation and build a single, collective $Q_3(a)$ from them (also shown in Figure 9.7, and in 9.8 and 9.10).

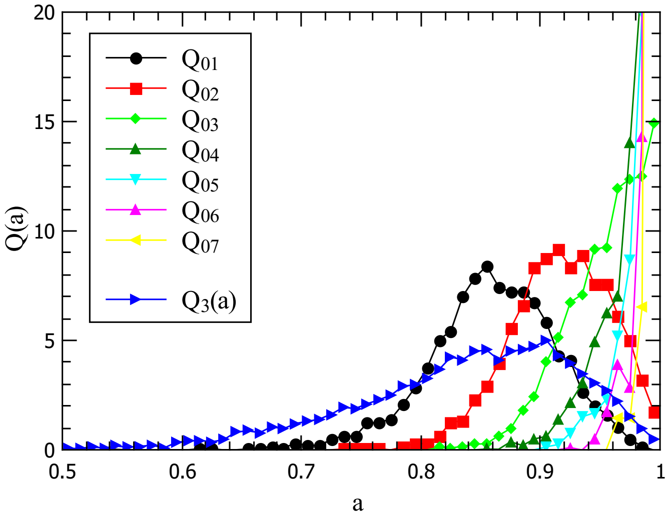

Figure 9.7: Individual Q_{0n} for $i = 2$. Dark blue triangles show a distribution $Q_3(a)$ made by binning only the smallest 3 values of a per nucleation.

Then we have

$$z \triangleq a\left(z + \frac{\xi}{3}\right), \tag{9.6}$$

where for $i = 1$ we have $\xi = 0.4706$ and for $i = 2$, $\xi = 0.6248$. This can also be modified into a DFPE with 2 variables,

$$z \triangleq a\left(z_1 + \frac{\xi z_2}{3}\right). \tag{9.7}$$

9.2.1 Results

Figures 9.8 and 9.10 show $Q(a)$ that takes all of the fractured zones into account, and $Q_3(a)$ where only the 3 that lost the most of their surface count (the rest are neglected). Solutions to the integral equations corresponding to the DFPEs (9.2), (9.4), (9.6), (9.7) are shown on Figures 9.9 and 9.11. All of the solutions are an extremely bad fit, with the solutions with $Q_3(a)$ consistently worse than the ones with the full $Q(a)$.

All of the solutions over - represent the average zone size, giving peaks around $z = 1$ which seriously overshoot the kMC data. We have seen in the 1d case that this overshooting happens when the mean field approximation is used, but only now it is so serious that the model becomes useless.

It is important to notice that the DFPE with 2 variables, z_1 and z_2 (Eqn. (9.4)) is still in a sense mean field, since it works with the average of the fractured cells contribution $a\eta z_2$ instead of all of the fractured parts individually (marked as $dZ1$, $dZ2$ and $dZ3$ on the post - nucleation zone schematics in Figure 9.4). In the case of $i = 1$, there are less of them ($\xi = 4.7084$ on average during the data collecting period of nucleation, as opposed to $\xi = 6.10633$ for $i = 2$). We would expect this to manifest as a slightly better fit of the mean field DFPE in the $i = 1$ case than in the $i = 2$, where more individual contributions were modelled with a single contribution $a\eta z_2$. However the opposite happened. Two problems could have lead to it: firstly, as we have seen on the CZD graphs in Figures 9.1 and 9.2, the choice of the intervals of θ in which the scaling regime is reached and we can collect the data for calculating Q, is somewhat arbitrary. Perhaps in one case (or both) we made bad choices and collected some of the data points which are not representative. Secondly, if we assume the intervals were equally well chosen in both cases, possible correlations between the neighbouring zones could have had a strong impact.

In the 1d case, the non-mean field DFPE improved the mean field results, but its integral equation form (Eqn. (3.21)) involved a bias in choosing the neighbouring gap and it was a double integral, which made it unfit for the task of calculating P from a known ϕ (inverse).

Here, an analogous non-mean field DFPE would complicate the model equation much more, so we will try everything we can to make the mean field model work.

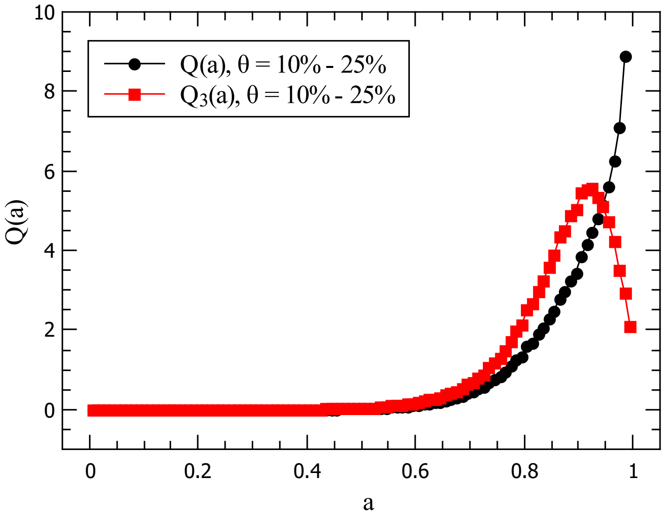

Figure 9.8: $Q(a)$ (black) and $Q_3(a)(red)$, for $i = 1$.

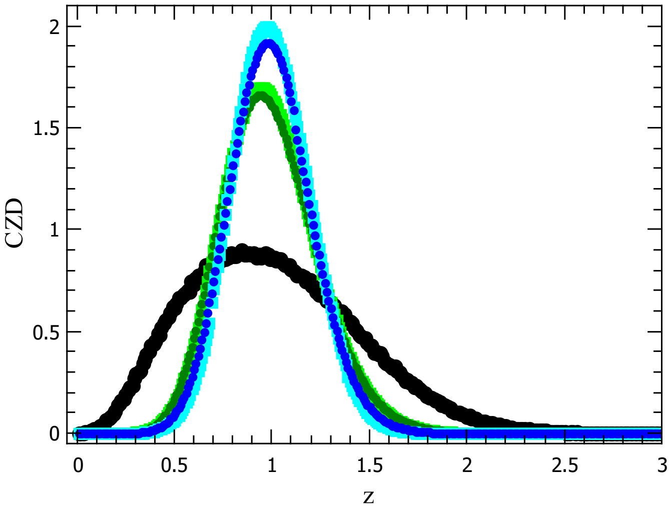

Figure 9.9: Solutions for the IE forms of DFPEs: (9.2) - light green, (9.4) - dark green, (9.6) - light blue, (9.7) - dark blue, for $i = 1$. Plotted on top of kMC CZD (black).

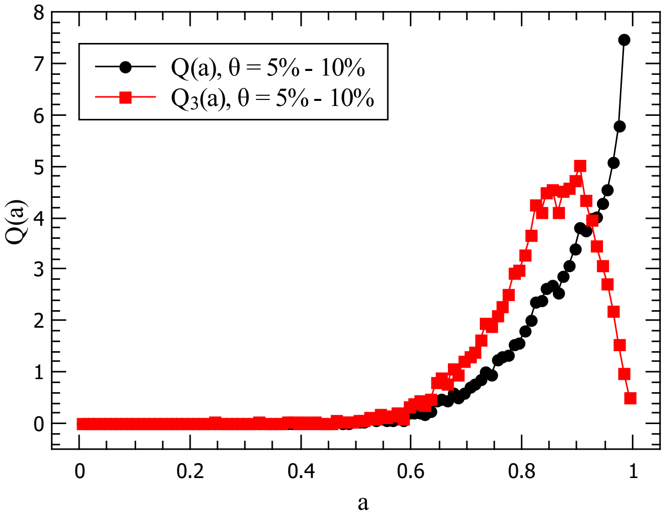

Figure 9.10: $Q(a)$ (black) and $Q_3(a)$ (red), for $i = 2$.

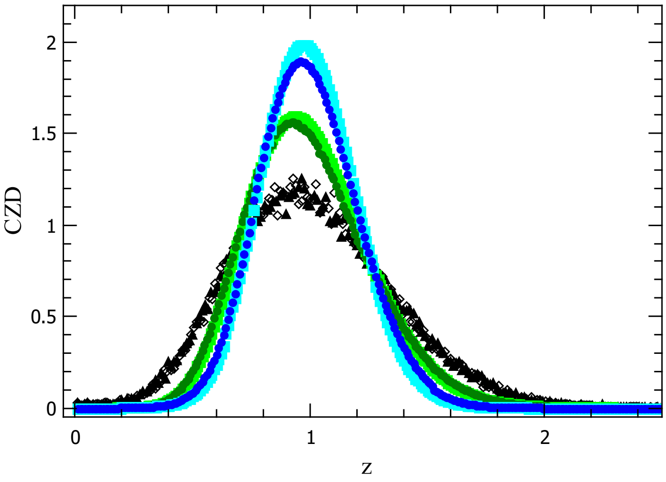

Figure 9.11: Solutions for the IE forms of DFPEs: (9.2) - light green, (9.4) - dark green, (9.6) - light blue, (9.7) - dark blue, for $i = 2$. Plotted on top of kMC CZD (black): $\theta = 5\%$ - empty squares and $\theta = 10\%$ - full triangles.

9.2.2 Inverses

To explore the behaviour of this (clearly bad) IE model a little further, we can invert them to see if we get the starting $Q(a)$ back. Again we use standard Tikhonov regularization method (zeroth order), as before in Chapter 5.

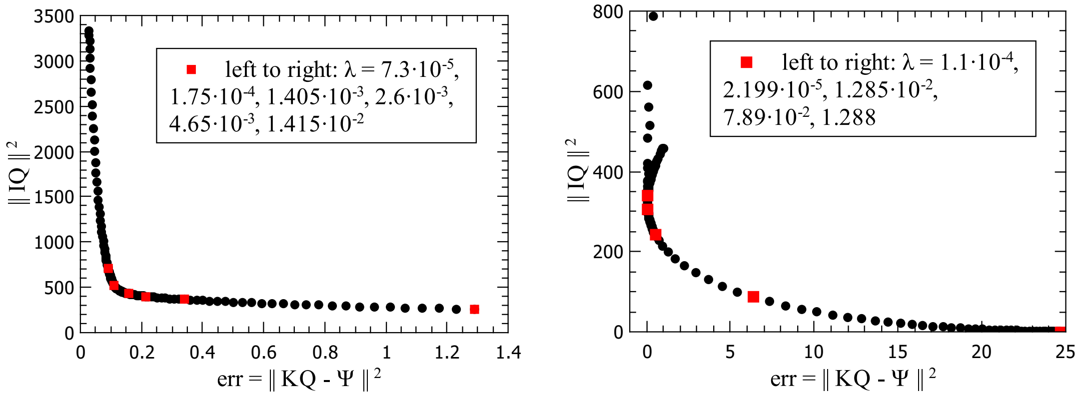

Figure 9.12: Left: L-curve for calculating $Q(a)$ from (9.2). Right: L-curve for calculating $Q_3(a)$ from (9.6).

We take the $i = 2$ case and distributions Q and Q_3 shown in Figure 9.10. For those two Q distributions we have solutions of the IEs corresponding to Equation (9.2) (shown in dark green in Figure 9.13) and Equation (9.6) (shown in black, Figure 9.13); these are the equations we invert to retrieve two distributions Q_λ.

Figure 9.12 shows the L-curve for retrieving Q (left panel) and Q_3 (right).

The best solutions are shown in Figure 9.14, and the integrals of those solutions Q_λ are shown on Figure 9.13, with the original (starting) IEs.

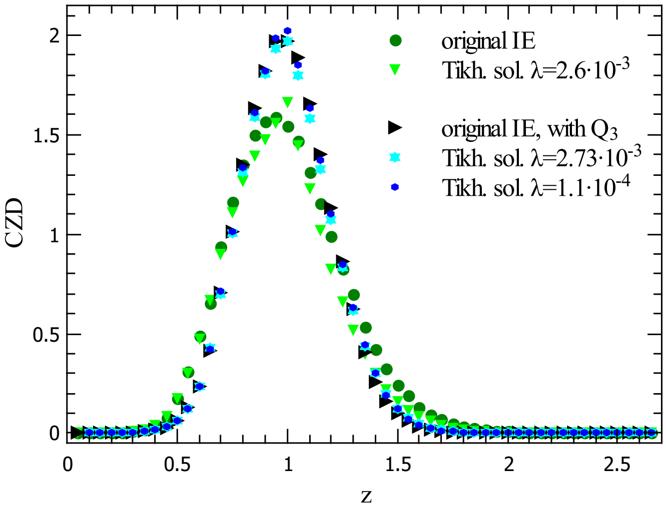

Figure 9.13: Solutions for the IE forms of DFPEs (9.2) (dark green), (9.6) (black) for $i = 2$, shown with the integrals of Tikhonov solutions Q_λ.

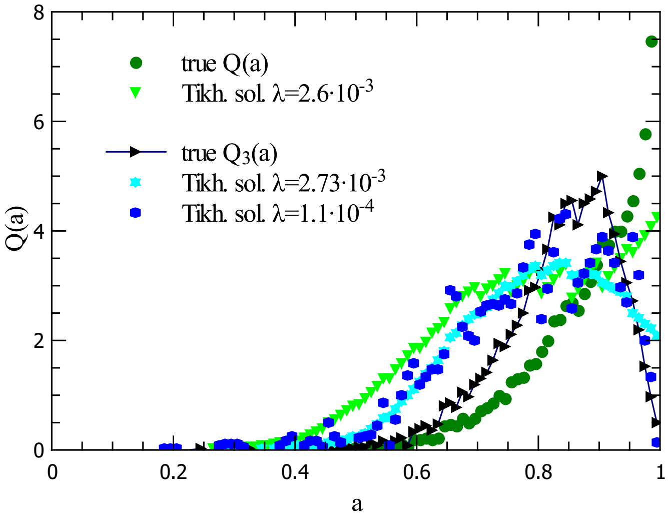

Figure 9.14: Measured Q and Q_3 shown with Tikhonov solutions Q_λ.

It is clear that the retrieved solutions Q_λ differ from the correct Q's (shown in dark green and black on Figure 9.14). Of course, true Q has a lot more noise here than the ones in 1d cases where we were always able to correctly reconstruct P. But, whatever the cause of failure, these are discouraging results. Not only does the IE (DFPE) fail to fit the kMC data directly, but it cannot even be inverted correctly. If CZDs in 2d can at all be somehow modelled with DFPEs of this type, it may not be possible to get a good fit on datasets with such a large amount of noise.

Just for the sake of completeness, results of inverting kMC CZD to get Q_λ and $Q_{3,\lambda}$ according to Equations (9.2) and (9.6) are shown on Figures 9.15 and 9.16.

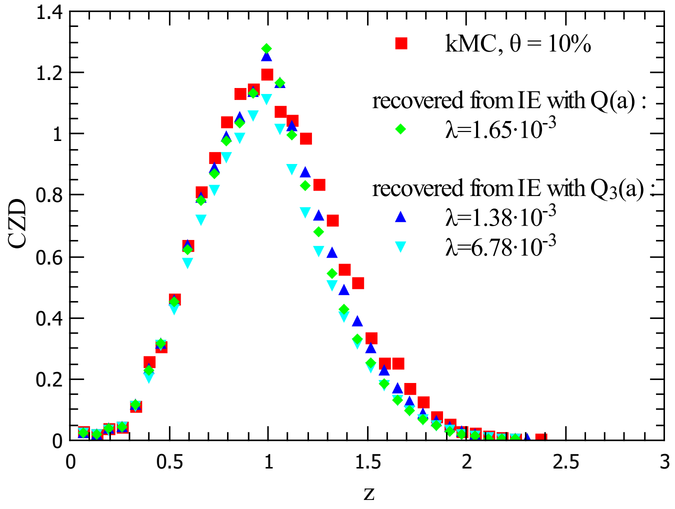

Figure 9.15: kMC CZD for $i = 2$, shown with the integrals of Tikhonov solutions.

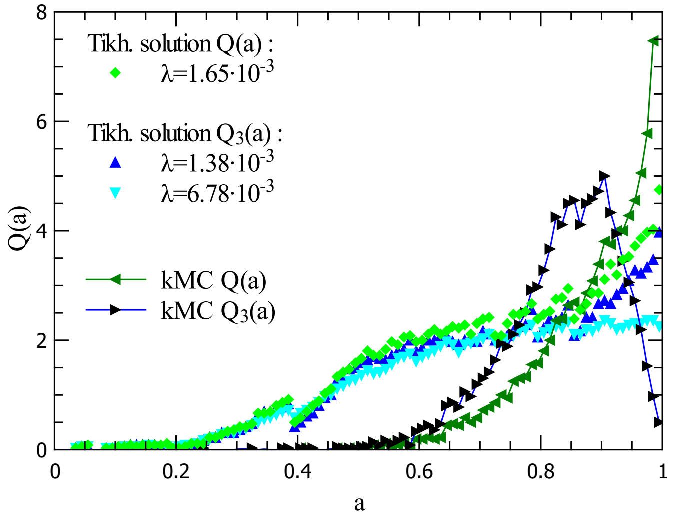

Figure 9.16: Measured Q and Q_3 shown with Tikhonov solutions Q_λ.

9.3 Modifying the model DFPE

9.3.1 Adding more zones

Since IE fails to fit kMC CZDs, the easiest thing to try next is a variation of DFPE (9.4) with different number of variables z:

$$z \triangleq a(z_1 + c\frac{z_2}{2}), \quad z \triangleq a(z_1 + c\frac{z_2 + z_3}{3}), \quad ..., \quad z \triangleq a(z_1 + c\frac{z_2 + ... + z_6}{6}) \tag{9.8}$$

Here the constant c is calculated from assuming all z_i have an average of 1 (and from kMC results, we know that $\langle a \rangle = 0.896$ for $i = 2$).

To get these distributions, we use an algorithm (similar to the one described in Section 4.1) that starts with a set of z's (initially set to 1 and 0). In each step we draw a necessary number of z_i at random from the set (each element of the set has the same probability to be chosen) – two for the first equation in (9.8) : $(z_1,\, z_2)$ etc. We draw a value of $a \in [0, 1]$ (where the probability of choosing a is given by $Q(a)$) and calculate the right hand sides of (9.8) . We repeat this 10^8 times and make a histogram from the results. Resulting distributions are all the same and indistinguishable from previously used DFPE (9.4) $(z = a(z_1 + \eta z_2))$, up to two decimal places, so we don't show the graph here.

During the kMC simulation, when an island nucleates, it fragments a few capture zones of various sizes, in different proportions, so assuming all of them can be taken to be of size 1 on average might be too crude of an approximation. Alternatively, trying to capture this process with a single choice of a per nucleation might be the problem (or both of it). In any case, introducing different zone sizes and values of a per nucleation that would reflect this is not straightforward and it would (if it would work) be an entirely empirical model. So, given the time constraints, we move on to try a simpler modification of (9.4).

9.3.2 Biased DFPE / Weighted IE

The simple MC procedure we have used to get a distribution of z doesn't correspond to the real situation: in kMC simulation, the Voronoi cells that are fragmented in new nucleation events are usually larger than the average cell on the lattice. Figures 9.5 and again 9.18 (left panel) show the distribution of cells fractured in new nucleations, $\psi^{pick}(z)$, as well as the distribution of the resulting new and remaining cell sizes. If we modify the simple MC procedure used to build DFPE solutions in such a way that each randomly chosen zone z from the set is chosen with the probability equal to $\psi^{pick}(z)$ from Figure 9.18 (pink circles), we have a biased DFPE (similar to the 1d case, Eqn. 3.21).

Results for the biased DFPE (9.2) and (9.4) for $i = 2$ are shown on Figure 9.17. It overshoots even more than the unbiased version. Since DFPEs already underestimate the amount of very small and very large zones, a bias that forces the algorithm to mainly choose z's around $z = 1$ only sharpened the result. Distribution of z's the algorithm drew from the available pool of z values to calculate biased DFPE is shown on Figure 9.18. The algorithm is set to prefer choosing z's according to probability distribution plotted in pink, but soon the set of z's is redefined according to $a(z + \eta)$ which leads to a much sharper distribution of z's chosen later on.

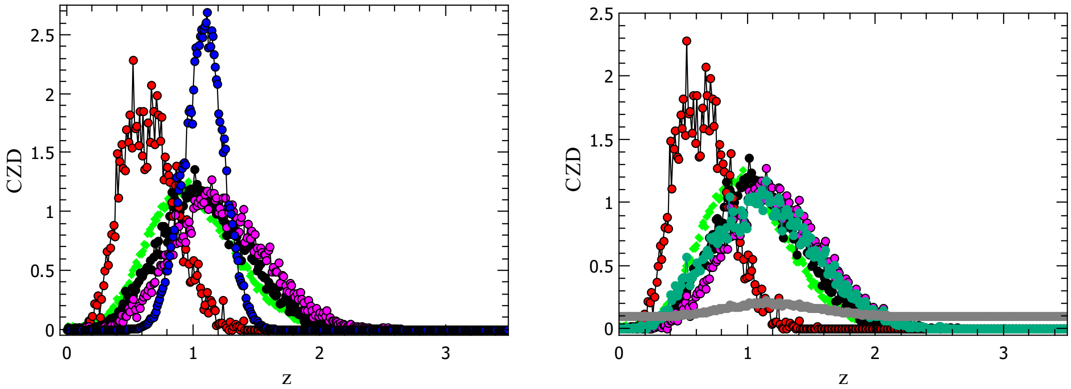

Figure 9.18: Left: Distribution of z's used in calculating the biased DFPE (blue), versus the distribution of zones fragmented in full kMC simulation (pink) that is used as a bias. Shown with full kMC simulation results: CZD at $\theta = 10\%$ (green), distribution of zone sizes after fragmentation (black) and the new zones (red) belonging to newly nucleated islands.
Right: Result of (9.9) shown in turquoise. Gray curve shows the result of (9.9) where we have set $\psi^{new}(z) = 1$.

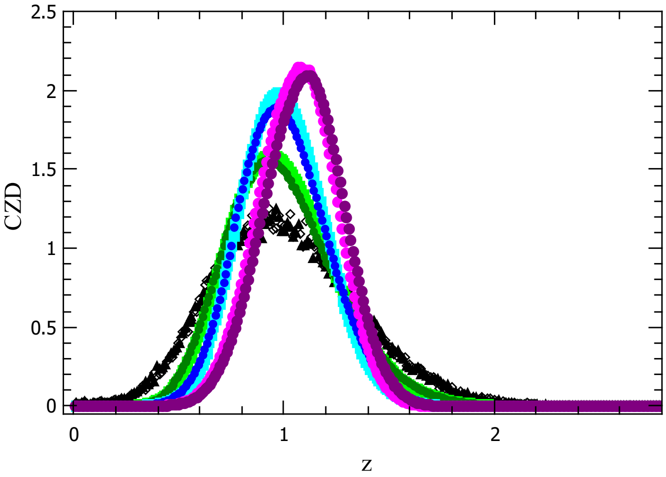

Figure 9.17: Biased DFPE (9.2) (pink) and (9.4) (purple) for $i = 2$, shown with unbiased versions (light green and green) and (9.6), (9.7) (light blue and blue) for comparison; kMC CZD is plotted black ($\theta = 10\%$ in full triangles and $\theta = 5\%$ in empty squares.

If instead of single variables z we add their individual distributions obtained as histograms from kMC simulation (where zone sizes were divided by the average zone size on the lattice at a given coverage before binning), according to:

$$\langle a \rangle \left(\psi^{pick}(z) + \frac{1}{\xi} \psi^{new}(z) \right) \tag{9.9}$$

(where $\langle a \rangle = 0.896$ is the average value of a for $i = 2$ and $\xi = 6.10633$ is the average number of fractured zones per nucleation), we get back the distribution of reduced zone sizes. This is shown in right panel on Figure 9.18.

We would (roughly) expect the distribution of reduced zone sizes to follow from $a(z^{pick} + \eta z^{pick})$, but DFPE $z \triangleq a(z_1 + \eta z_2)$ is either a wrong approach completely or it requires some modifications that would somehow capture the complex two dimensional picture.

We saw in one dimension that the mean filed assumption that we can take the neighbouring zone to be of size 1 leads to CZD results that overestimate the number of zones with size $z \approx 1$ (too high peaks around 1) and underestimate the very small and large zones. This was most apparent in the DFPE model we devised in the previous chapter with intent of expanding it here to 2d; but it was also happening (although far less dramatically) with the gaps and capture zone DFPEs we used all up until Chapter 8.

In 1d case, assuming the neighbouring capture zone can taken to be of size 1 introduces *one* simplification. On a 2d substrate, this multiplies: for $i = 1$ we have (on average) $\xi = 4.7084$, and for $i = 2$ $\xi = 6.10633$, neighbours set to size 1. So instead of one approximation, we are here introducing 5-6 ones.

Another issue is the way we calculate and use a: we assume that the collection of those 5-6 zones we've set to size 1 will be sliced into two proportions, all with the same a - regardless of their positions (and actual shapes!) on the lattice. So again we are averaging: by fragmenting all of the neighbour zones with the same value of a in our model, we are replacing individual fragmentations with a sort of an effective, average a we draw once per nucleation from $Q(a)$.

9.4 Sampling the newly created zones

We have so far only focused at the process of fragmenting (reducing) old zones, so we now explore the newly created zones.

As before in the 1d case, we can look at the zones around newly nucleated islands. On scheme in Figure 9.4, the new zone (white with red edges) consists of 3 fragments of the old zones. Previously we have been defining a as the ratio of the reduced (grey) zones and their original sizes; now if we define it as the portion of the size that was taken ($dZ1$) from the old zone divided by its original size ($Z1 + dZ1$), we have a new $Q^{new}(a)$:

$$Q^{new}(a) = Prob\left(\frac{dZ}{Z}\right) = (1 - Q), \tag{9.10}$$

where by Q we denote the old $Q(a)$ that was used in previous sections. All of the fractured zones were used in creating this Q^{new}, within the same coverage ranges as before (so they are just symmetric images of old Q (Figures 9.8 and 9.10, black circles) around $a = 0.5$).

Then we can sample the size distribution of new cells according to:

$$z \triangleq \frac{1}{\xi}\sum_{i=1}^{\xi}\frac{a_i}{\langle a\rangle}, \tag{9.11}$$

where ξ is the average number of zones fractured in a nucleation and all of the a_i were drawn from Q^{new}.

When we calculate (sample and build histograms) distribution $\psi(z)$ according to (9.11), in each step we draw a_i's from $[0, 1]$ according to Q^{new} and sum them to get left hand z. We draw (and sum) a different number of them in different steps so that the final result contains on average ξ of a_i's (when averaged over all the steps).

For $i = 1$, $\xi = 4.7084$, we sample (9.11) in 10^6 steps: in 9×10^5 steps draw 5 a_i's, in 904×10^2 steps draw 2, in 9×10^3 draw 3 and in 600 draw 1.

For $i = 2$, $\xi = 6.10633$ and from 10^6 steps, in 9×10^5 draw 6, in 9×10^4 draw 7, in

9×10^3 draw 8, in 800 draw 5, in 130 draw 2 and in 70 draw 1.

Results fit nicely on top of the kMC obtained CZD (the usual distribution of zone sizes found on the lattice at a relevant coverage); they are shown on Figure 9.19.

Rounding up ξ to the nearest integer in (9.11) is an approximation that gives a visibly worse fit (as shown on Figure 9.19, left panel) and a simpler model equation $z \triangleq \xi a$ is obviously wrong, so there is no way of (simply) calculating $Q^{new}(a)$ from a known (measured) CZD.

Equation (9.11) contains a mean field assumption which sets all of the newly created zone sizes to 1; without this the equation reads:

$$z \triangleq \frac{1}{\xi \langle a \rangle} \left(a_1 z_1 + a_2 z_2 + ... + a_\xi z_\xi \right). \tag{9.12}$$

The resulting distribution for $i = 2$ is shown on Figure 9.19 (right panel, plotted red). Again, in building this distribution, all of the z_i are drawn with an equal probability from the set of zones (like in section 9.3.1). Average zone size is $\langle z \rangle = 0.89$.

If we bias the selection of z_i's so that each is chosen with a probability $\psi^{pick}(z)$ (pink circles on Figure 9.5), we get a reasonably good fit for kMC CZD that should be within rounding and binning errors from mean field Equation (9.11). Noise in $\psi^{pick}(z)$ also enters the equation, all of which probably contribute to the mean field version being a better fit for kMC CZD. The biased Equation (9.12) is shown for $i = 2$ only (on Figure 9.19, right panel, in orange). In calculation, the right hand side of the equation had to be multiplied by 1.08 to bring $\langle z \rangle$ closer to 1 (this accounts for the noise and binning errors that entered the equation); the result is $\langle z \rangle = 1.009$.

Clearly, focusing on the daughter zones instead of the parents as we did before, leads to a good model for the CZD. Interestingly, the full Equation (9.12) makes a slightly worse fit that Eqn.(9.11) (which is it's approximation, where all of the $z_i = 1$), as seen from the $i = 2$ case graphs (yellow and orange). This may be due to noise levels and rounding errors which always increase as the number of variables we use increases.

Equation (9.11) offers the possibility of getting a CZD that is close to the real, kMC obtained CZD if $Q(a)$ is known; so exploring its properties further looks like the most

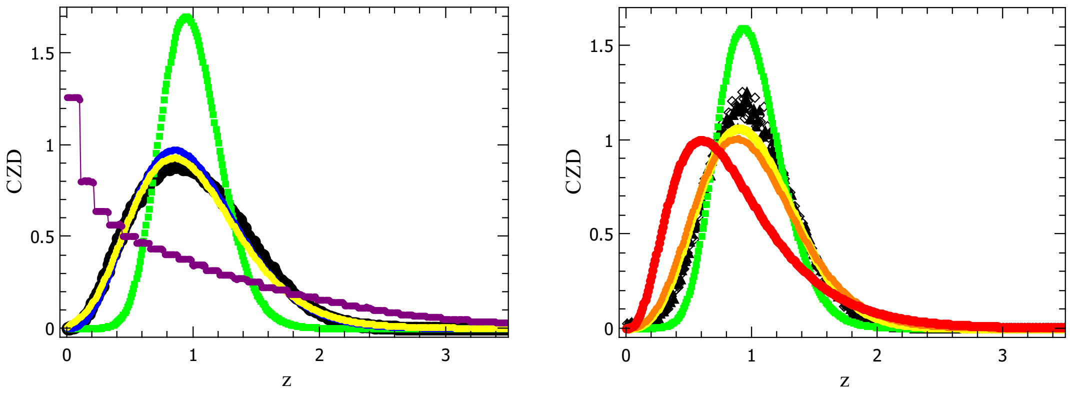

Figure 9.19: Left: kMC CZD for $i = 1$ (black), shown with IE form of DFPE (9.2) (green). Results of Equation (9.11) are shown in yellow. An approximation of (9.11) where ξ is set to 5 is shown in blue. Purple curve is a plot of $z \triangleq \xi a$.
Right: kMC CZD for $i = 2$ (black, full ($\theta = 10\%$) and empty ($\theta = 5\%$) symbols), with IE form of DFPE (9.2) (green). Equation (9.11) is shown in yellow, Equation (9.12) in red and biased (9.12) (each z_i drawn with the probability $\psi^{pick}(z)$) is plotted in orange.

promising future direction.

To summarize, in this chapter we have tried to extend the 1d CZD model from Chapter 8 to 2d. We have tested both the approach that focuses on the reduction of the old zone size, yielding a DFPE model, and the approach where we trace the origins of the newly created (daughter) zone (belonging to the newly nucleated island).

The failed attempts to make the mean field DFPE $z \triangleq a(z_1 + \eta z_2)$ work, along with the assumption that there are no correlations between neighbouring zones, also assume that the reduced parent zone can always be traced back to the original size by adding the portion $a\eta z_2$ (taken by the daughter), with a single a and z_2 variable. This has proved itself to be too crude of an approximation.

Had the time restrictions permitted it, we could have modified the DFPE with 3 variables (z_1, z_2 and a) into a DFPE with $1{+}\xi + \xi$ variables (z and $z_1, z_2, ..., z_\xi$ instead of only z_2, and $a_1, ...a_\xi$ instead of only a):

$$z \triangleq [a_1(z + \eta_1 z_1) + a_2(z + \eta_2 z_2) + ... + a_\xi(z + \eta_\xi z_\xi)] \, \frac{1}{\xi}. \qquad (9.13)$$

Then, instead of having only z_2 and drawing a from the joint Q we would have $z_1, z_2...$ and draw $a_1, a_2, ...$ from the individual distributions Q_{01}, $Q_{02}...$ which were shown on Figure 9.7. However, even if this would give a good fit, it would heavily rely on empirical parameters (η can only be measured from a kMC simulation, where all the nucleation steps can be traced; this cannot be done in experiments). It would also most likely lead to a model from which it is not possible to calculate Q when CZD is known.

The alternative approach of focusing on the new (daughter) zone, gave us reasonably good results. The governing equations still neglect any possible correlations between the neighbouring zones and effects their shapes could have on the fragmentation process. But, unlike the DFPE approach, they include 5-6 (on average) different values of a per nucleation, all independently chosen from $Q^{new}(a)$. Within this model, we also got good results when setting all of the 5-6 zone sizes to 1; equation $z \triangleq \frac{1}{\xi}\sum_{i=1}^{\xi} a_i/\langle a \rangle$ looks like a promising future direction. It does however require that ξ is known; ideally it is simply related to i so it could be deduced in experiments, but it is also possible that this parameter can only be obtained from a kMC simulation. It is also not clear if the model equation would allow Q^{new} to be calculated from a known CZD.

Chapter 10

Conclusion

Explaining the island nucleation and growth processes analytically is an open research problem, with ongoing development of theoretical models to describe the scaling properties of the island sizes and spatial distribution. Within that niche, in the last two decades the focus has somewhat shifted from the problem of obtaining the correct form of the ISD to that of the CZD.

In cases when one needs to fit the kMC or experimentally obtained CZD to a functional form (for example, to deduce i), both the Gamma distribution and the Generalized Wigner surmise have been used frequently. The DFPEs originally proposed in Ref. [5] similarly offer a (relatively) quick to use model function, one that differentiates between i and $P(a)$, and also provides a model for the nucleation process instead of just a fitting function. This makes it a promising candidate, especially if it can be extended to higher dimensions.

We have therefore in this work aimed to explore the behaviour of the model and some of its possibilities.

The 1d DFPE model (Chapter 3.2), both for the gaps and the capture zones, establishes two theoretical limiting cases of nucleation: a purely deposition and a diffusion driven, with the kMC GSD and CZD leaning towards the diffusion limit. One then naturally asks how do the probabilities P_{kMC} which correspond to kMC data look like, and can they be calculated from a given (experimental or simulations) GSD (CZD).

In chapters 6 and 5 we have calculated P distributions, both with a textbook -

method of regularisation and our own method which enforced symmetry and positivity of the solution. For the case of the gaps, where it is possible to measure P directly during the kMC simulations, we have also compared the calculated to the measured P. By doing so, we found a good level of self - consistency within the model. However we have also found recurring discrepancies between the kMC data and the mean field DFPE we have been using, which tell us that the model works as a good approximation but it isn't accurate enough for the purpose of determining exactly how much does the diffusion theoretical case, versus the deposition, contribute to the true nucleation process (which we take to be represented by the kMC simulation). This becomes apparent when we fit the kMC GSD and P_{kMC} on a combination of the diffusion and deposition model: there is no consistency between the P_{kMC} and GSD fitting results (Table 7.1). The only conclusion we can make is that, within the our model framework, the kMC GSD and CZD can be reasonably well described with the mean field DFPE that is close to the diffusion driven theoretical case.

Since P_z for the capture zones is sampled from the distribution P for the gaps, it cannot be directly measured so we can only rely on the inverse problem solutions. However, because the solutions from two different methods look much more alike than they did for the gaps, we can take them with confidence. The solutions have broken slightly above the diffusion theoretical case for $i = 2$ and 3, reflecting again the limits of the mean field approximation. In this model, additionally an assumption that the neighbouring gaps are uncorrelated is used, and we have seen that this is not completely true from the plots of the CZD calculated as a convolution of the kMC GSD.

The inability of directly measuring P_z for the capture zones from simulations has led us to define and measure another distribution, Q; a probability of fragmenting a capture zone at a certain position. This then leads to a DFPE that doesn't rely on the concept of a gap, which makes it a preferred choice of an equation to be tested on a two dimensional substrate - but all our efforts with getting it to work in 2d failed. While in 1d the mean field approximation lead to slightly higher peaks than those of the kMC CZD, in 2d this became so severe the model can't be used. It might be possible to modify it in such a way that it incorporates a sufficient amount of information to model kMC CZD correctly; a possible future direction would be testing an equation such as (9.13), where the contributions of each individual neighbouring zone is taken into account rather than a single, average one. Getting at least a better fit with such an equation would strengthen the case for using a DFPE model which uses the Q distribution. We don't see however if there would be any practical implications since it would rely entirely on numerically determined factors that need to be obtained from simulations for each individual case.

Another possible direction is to return to the original DFPE with P_z sampled from the corresponding distribution for the gaps, and see if it can be extended to 2d. The Delaunay triangulation which is dual to the Voronoi tesselation, might be used in 2d to mimic the idea of the interisland gaps. Then the DFPE (from Chapter 3.2) we used in 1d can be tested in 2d, with x and z this time standing for the area rather than length. If the model is appropriate, it should be possible to calculate the distribution P from the size distribution of the Delaunay cells (gaps) and relate it the distribution P_z for the Voronoi cells, just like in 1d (here we would also need to determine how many neighbouring gaps are involved in a new capture zone formation). Based on the 1d to 2d transition attempt we have done, we strongly suspect that this model might also be inadequate as it oversimplifies the nucleation process, but it would certainly provide new insights into the problem.

Finally, when focusing on the creation of the new capture zones as we did in Chapter 8, we can easily sample the correct form of the CZD from a known distribution Q (as $z \triangleq 0.5(a_1 + a_2)$). In the 1d case, Q can be calculated from the associated mean field DFPE and known CZD, but in 2d we were only able to measure it during simulation. It is unclear if it could in any way be calculated or correctly estimated when working with experimental data. Yet since this method worked reasonably well in both one and two dimensions, its further exploration is the most promising future direction stemming from this thesis.

Appendix A

Derivation of the Integral Equation from the non - mean field DFPE

The non - mean field DFPE has the form:

$$z \triangleq a(z_1 + \eta z_2). \tag{A.1}$$

The random variables $z \in [0, \infty)$, $z_1 \in [0, \infty)$, $z_2 \in [0, \infty)$ and $a \in [0, 1]$ have probability distributions $\phi(z)$, $\phi(z_1)$, $\phi(z_2)$ and $P(a)$.

We denote the cumulative distribution function (CDF) of z as $\Phi(z)$. CDF is defined as $\Phi(z) = \int_0^z \phi(t)dt$, so we can write Eqn. (A.1) as:

$$\begin{aligned}
\Phi(z) &= Prob[a(z_1+\eta z_2) \leq z] \\
&= E\left[Prob[a(z_1+\eta z_2) \leq z \mid a]\right] \\
&= \int_0^1 Prob[a(z_1+\eta z_2) \leq z] P(a) da \\
&= \int_0^1 E[Prob[a(z_1+\eta z_2) \leq z \mid z_1]] P(a) da \\
&= \int_0^1 \int_0^{z/a} Prob[a(z_1+\eta z_2) \leq z] \phi(z_1) P(a) dz_1 da \\
&= \int_0^1 \int_0^{z/a} Prob\left[z_2 \leq \left(\frac{z}{a} - z_1\right)\frac{1}{\eta}\right] \phi(z_1) P(a) dz_1 da.
\end{aligned} \tag{A.2}$$

Here the upper integral limit is z/a because $\left(\frac{z}{a} - z_1\right)$ has to be ≥ 0. Now we have:

$$\Phi(z) = \int_0^1 \int_0^{z/a} \Phi\left(\frac{1}{\eta}\left(\frac{z}{a} - z_1\right)\right) \phi(z_1) P(a) dz_1 da. \tag{A.3}$$

If we differentiate Eqn. (A.3) with respect to z, with the use of the Leibniz rule (3.6), we get:

$$\phi(z) = \int_0^1 da \int_0^{z/a} dz_1 \cdot \phi\left(\frac{z}{\eta a} - \frac{z_1}{\eta}\right) \phi(z_1) \frac{P(a)}{\eta a} + 0. \tag{A.4}$$

Appendix B

Code block for generating gap sizes according to the mean field DFPE

The procedure described in Section 4.1 is written in the code as:

```
x = 0.0
x(1) = 1.0
 DO i = 2, M
  call random_number(harvest)          here, harvest is an auxiliary real variable
  nuse = INT((i-1)*harvest) + 1              nuse is an auxiliary integer variable
  xran = x(nuse)
  call random_number(harvest)
  a = harvest
  x(i) = a*(1.0 + xran)
  x(nuse) = (1.0 - a)*(1.0 + xran)
 END DO
```

Appendix C

Mathematical background for the problem of ill-posedness

Definition C.1. Let $\mathcal{K} : U \to V$ be an operator from a subset U of a normed space X into a subset V of a normed space Y. The equation

$$\mathcal{K} f = g \tag{C.1}$$

(where f is the unknown) is called well - posed or properly posed if $\mathcal{K} : U \to V$ is bijective and the inverse operator $\mathcal{K}^{-1} : V \to U$ is continuous. Otherwise, the equation is called ill - posed or improperly posed.

(A function is bijective if it is surjective (*every* element of the codomain is mapped to by at least one element of the domain; the function "hits" the whole codomain) and injective (every element from the domain is mapped to a *different* element in the codomain; the function never maps different domain elements to the same codomain element).)

According to Definition C.1 there are three possibilities of ill - posedness [81, p.298]. Firstly, equation (C.1) can't be solved for all $g \in V$ if $\mathcal{K}$ is not surjective (nonexistence of a solution). Equation (C.1) can have many solutions if $\mathcal{K}$ isn't injective (nonuniqueness of a solution) and, finally, if $\mathcal{K}^{-1} : V \to U$ isn't continuous then the solution does not depend continuously on the data (instability).

Ill - posedness (or well - posedness) is a property of $\mathcal{K}$ but also of the solution space X and the input data space Y (and the norms on X, Y), so we need to look into the properties of the operator $\mathcal{K}$ and the subspaces it works on:

Definition C.2. A set $U_1 \subset X$ is bounded if there exists a positive number C such that $\|x\| \leq C$ for every $x \in U_1$.

Definition C.3. A bounded operator is a linear operator $\mathcal{K} : U \to V$ (where U, V are subspaces of normed spaces X, Y) for which there is a positive number M such that $\|\mathcal{K}f\| \leq M\|f\|$, for all $f \in U$.

Definition C.4. Let X be a normed space.
a) A sequence $(x_n) \in X$ has an accumulation point in $x_0 \in X$ if every open neighbourhood of x_0 contains infinitely many elements of the sequence.
b) A set $U_1 \in X$ is called compact if every sequence in U_1 has an accumulation point in U_1.

It is also useful to introduce a compact set in another way. By the Heine - Borel theorem, a compact subset of a normed space is a subset that is totally bounded (it can be covered with a finite number of open balls of *any* radius $r \in \mathbb{R}_{>0}$ with centres inside the subset) and complete (contains the limit of all of its Cauchy sequences). In finite dimensional spaces, a bounded set is also totally bounded, but that no longer holds in infinite dimensional spaces, which makes the requirement for a set to be compact much harder to meet in an infinite dimensional space. A typical example that demonstrates this is a closed unit ball: it is only compact in finite dimensional spaces (proof in [82, p.163]).

Definition C.5. A linear operator $\mathcal{K} : U \to V$ from a normed space U into a normed space V is compact if it maps each bounded set in U into a relatively compact set in V; that is, into a set whose closure (a union of a set and its limit points, or equivalently, the unique smallest closed set containing the given set) is compact.

An alternative definition is usually used; in our case it is not as instructive, but for the sake of completeness, we write it here:

Definition C.6. A linear operator $\mathcal{K} : U \to V$ is said to be compact if for every bounded sequence (f_n) in the normed space U the sequence $(\mathcal{K} f_n)$ has a convergent subsequence in the normed space V.

From the previous definitions it is clear that the requirement for an operator to be compact is harder to satisfy than that of boundedness.

Ill - posedness of the operator $\mathcal{K}$ is a consequence of its compactness. To see how the compactness of $\mathcal{K}$ leads to an unbounded inverse $\mathcal{K}^{-1}$, we need the following theorems (2.19,2.21 and 2.25 from [81] , chapter 2):

Theorem C.1. *Compact linear operators are bounded.*

Theorem C.2. *Let U, V, W be subspaces of normed spaces X, Y, Z and $A : U \to V$ and $B : V \to W$ bounded linear operators. Then the product $BA : U \to W$ is compact if and only if one of the two operators, A or B, is compact.*

Theorem C.3. *The identity operator $I : U \to U$ is compact if and only if U is of finite dimension.*

The reason for this is that an identity operator would map a unit ball into a unit ball, which in an infinite dimensional space cannot be compact, so neither can the identity operator [83, p.91].

From Theorems C.1 and C.2, if $\mathcal{K}$ is compact, the product $\mathcal{K}^{-1}\mathcal{K} = I : U \to U$ is compact if $\mathcal{K}^{-1}$ is bounded. Then, if U is not of finite dimension, I is a compact linear operator from infinite-dimensional U to U, which contradicts Theorem 3. Therefore, if U is infinite-dimensional, I must not be compact from which follows that the inverse $\mathcal{K}^{-1}$ must not be bounded.

This can be formulated strictly as the following theorem (for proof see [84, p.12]):

Theorem C.4. *Let X, Y be normed spaces and let $\mathcal{K} : U \to V$, $U \subset X$ and $V \subset Y$, be a compact linear operator. Then the equation of the first kind $\mathcal{K} f = g$ is not well posed if U is not of finite dimension. If U is infinite dimensional, then the inverse $\mathcal{K}^{-1}$ is unbounded; we can find a sequence (f_n) such that $\mathcal{K} f_n \longrightarrow 0$ but $\|f_n\| \longrightarrow \infty$.*

A consequence of this is that, when performing numerical calculations for a finite dimensional approximation of $\mathcal{K}$ ($\mathcal{K}$ being a continuous operator in an infinite dimensional space), increasing the accuracy of the approximation (that is, increasing the degree of discretization) results in less reliable solutions [81, p.300].

Bibliography

[1] M. Einax, W. Dieterich, and P. Maass, “Colloquium: Cluster growth on surfaces: Densities, size distributions, and morphologies,” *Reviews of Modern Physics*, vol. 85, no. 3, pp. 921–939, 2013.

[2] G. Bales and D. Chrzan, “Dynamics of irreversible island growth during submonolayer epitaxy,” *Physical Review B*, vol. 50, no. 9, pp. 6057–6067, 1994.

[3] P. Mulheran and J. Blackman, “The origins of island size scaling in heterogeneous film growth,” *Philosophical magazine letters*, vol. 72, no. 1, pp. 55–60, 1995.

[4] P. Šeba, “Parking in the city,” *Acta Physica Polonica A*, vol. 4, no. 112, pp. 681–690, 2007.

[5] P. A. Mulheran, K. P. O’Neill, M. Grinfeld, and W. Lamb, “Distributional fixed-point equations for island nucleation in one dimension: A retrospective approach for capture-zone scaling,” *Physical Review E*, vol. 86, no. 5, pp. 051 606–051 614, 2012.

[6] W. H. Press, W. T. Vetterling, S. A. Teukolsky, and B. P. Flannery, *Numerical Recipes in Fortran 77 and 90*, 2nd ed. Cambridge University Press, Cambridge, 1992.

[7] W. S. Knodle and R. Chow, “10 - Molecular Beam Epitaxy: Equipment and Practice,” in *Handbook of Thin Film Deposition Processes and Techniques (Second Edition)*, K. Seshan, Ed. William Andrew Publishing, 2001, pp. 381 – 461.

[8] D. Walton, “Nucleation of vapor deposits,” *The journal of chemical physics*, vol. 37, no. 10, pp. 2182–2188, 1962.

[9] C. Ratsch and J. Venables, “Nucleation theory and the early stages of thin film growth,” *Journal of Vacuum Science & Technology A: Vacuum, Surfaces, and Films*, vol. 21, no. 5, pp. S96–S109, 2003.

[10] M. Bartelt, J. Hannon, A. Schmid, C. Stoldt, and J. Evans, “Island formation during deposition or etching,” *Colloids and Surfaces A: Physicochemical and Engineering Aspects*, vol. 165, no. 1, pp. 373–403, 2000.

[11] J. Evans, P. Thiel, and M. Bartelt, “Morphological evolution during epitaxial thin film growth: Formation of 2D islands and 3D mounds,” *Surface Science Reports*, vol. 1, no. 61, pp. 1–128, 2006.

[12] J. Venables, G. Spiller, and M. Hanbucken, “Nucleation and growth of thin films,” *Reports on Progress in Physics*, vol. 47, no. 4, pp. 399–459, 1984.

[13] M. Li and J. Evans, “Geometry-based simulation (GBS) algorithms for island nucleation and growth during sub-monolayer deposition,” *Surface science*, vol. 546, no. 2, pp. 127–148, 2003.

[14] P. Mulheran and J. Blackman, “Capture zones and scaling in homogeneous thin-film growth,” *Physical review B*, vol. 53, no. 15, pp. 10 261–10 267, 1996.

[15] J. Blackman and P. Mulheran, “Scaling behavior in submonolayer film growth: A one-dimensional model,” *Physical Review B*, vol. 54, no. 16, pp. 11 681–11 692, 1996.

[16] C. Ratsch, Y. Landa, and R. Vardavas, “The asymptotic scaling limit of point island models for epitaxial growth,” *Surface science*, vol. 578, no. 1, pp. 196–202, 2005.

[17] J. Blackman and P. Mulheran, “Growth of clusters on surfaces: Monte Carlo simulations and scaling properties,” *Computer physics communications*, vol. 137, no. 1, pp. 195–205, 2001.

[18] P. Mulheran, “Theory of cluster growth on surfaces,” *Handbook of Metal Physics*, vol. 5, pp. 73–111, 2008.

[19] H. Krcelic, M. Grinfeld, and P. Mulheran, “Distributional fixed-point equations for island nucleation in one dimension: The inverse problem,” *arXiv preprint arXiv:1806.03776*, 2018.

[20] J. Nieminen and K. Kaski, “Rate-equation study of nucleation and growth of thin films. i. growth of one monolayer,” *Physical Review A*, vol. 40, no. 4, pp. 2088–2095, 1989.

[21] M. Bartelt and J. W. Evans, “Exact island-size distributions for submonolayer deposition: Influence of correlations between island size and separation,” *Physical Review B*, vol. 54, no. 24, pp. R17 359–R17 362, 1996.

[22] G. Bales and A. Zangwill, “Self-consistent rate theory of submonolayer homoepitaxy with attachment/detachment kinetics,” *Physical Review B*, vol. 55, no. 4, pp. R1973–R1976, 1997.

[23] J. W. Evans and M. Bartelt, “Nucleation, growth, and kinetic roughening of metal (100) homoepitaxial thin films,” *Langmuir*, vol. 12, no. 1, pp. 217–229, 1996.

[24] T. Vicsek and F. Family, “Dynamic scaling for aggregation of clusters,” *Physical Review Letters*, vol. 52, no. 19, pp. 1669–1672, 1984.

[25] C. Ratsch, A. Zangwill, P. Šmilauer, and D. Vvedensky, “Saturation and scaling of epitaxial island densities,” *Physical Review Letters*, vol. 72, no. 20, pp. 3194–3197, 1994.

[26] J. G. Amar, F. Family, and P.-M. Lam, “Dynamic scaling of the island-size distribution and percolation in a model of submonolayer molecular-beam epitaxy,” *Physical Review B*, vol. 50, no. 12, pp. 8781–8797, 1994.

[27] J. A. Stroscio and D. T. Pierce, “Scaling of diffusion-mediated island growth in iron-on-iron homoepitaxy,” *Physical Review B*, vol. 49, no. 12, pp. 8522–8525, 1994.

[28] F. Gibou, C. Ratsch, and R. Caflisch, "Capture numbers in rate equations and scaling laws for epitaxial growth," *Physical Review B*, vol. 67, no. 15, pp. 155 403–155 407, 2003.

[29] H.-J. Ernst, F. Fabre, and J. Lapujoulade, "Nucleation and diffusion of Cu adatoms on Cu(100): A helium-atom-beam scattering study," *Physical Review B*, vol. 46, pp. 1929–1932, 1992.

[30] J.-K. Zuo, J. Wendelken, H. Dürr, and C.-L. Liu, "Growth and coalescence in submonolayer homoepitaxy on Cu (100) studied with high-resolution low-energy electron diffraction," *Physical Review Letters*, vol. 72, no. 19, pp. 3064–3067, 1994.

[31] J. Blackman and A. Wilding, "Scaling theory of island growth in thin films," *EPL (Europhysics Letters)*, vol. 16, no. 1, pp. 115–120, 1991.

[32] J. G. Amar and F. Family, "Critical cluster size: Island morphology and size distribution in submonolayer epitaxial growth," *Physical Review Letters*, vol. 74, pp. 2066–2069, 1995.

[33] J. M. Pomeroy and J. D. Brock, "Critical nucleus phase diagram for the Cu(100) surface," *Physical Review B*, vol. 73, pp. 245 405–245 412, 2006.

[34] F. Loske, J. Lübbe, J. Schütte, M. Reichling, and A. Kühnle, "Quantitative description of C_{60} diffusion on an insulating surface," *Physical Review B*, vol. 82, pp. 155 428–155 433, 2010.

[35] R. Ruiz, B. Nickel, N. Koch, L. C. Feldman, R. F. Haglund, A. Kahn, F. Family, and G. Scoles, "Dynamic scaling, island size distribution, and morphology in the aggregation regime of submonolayer pentacene films," *Physical Review Letters*, vol. 91, pp. 136 102–136 106, 2003.

[36] X. Lu, M. Koyama, Y. Izumi, Y. Nakata, S. Adachi, and S. Muto, "Size distribution and scaling behavior of InAlAs/AlGaAs quantum dots grown on GaAs by molecular beam epitaxy," *Japanese Journal of Applied Physics*, vol. 52, no. 2R, pp. 025 602–025 606, 2013.

[37] A. Banerjee, T. Frost, S. Jahangir, E. Stark, and P. Bhattacharya, “InGaN/GaN self-organized quantum dot lasers grown by molecular beam epitaxy,” *Journal of Crystal Growth*, vol. 378, pp. 566–570, 2013.

[38] T. Potocar, S. Lorbek, D. Nabok, Q. Shen, L. Tumbek, G. Hlawacek, P. Puschnig, C. Ambrosch-Draxl, C. Teichert, and A. Winkler, “Initial stages of a para-hexaphenyl film growth on amorphous mica,” *Physical Review B*, vol. 83, pp. 075 423–075 433, 2011.

[39] M. Bartelt, A. Schmid, J. Evans, and R. Hwang, “Island size and environment dependence of adatom capture: Cu/Co islands on Ru (0001),” *Physical Review Letters*, vol. 81, pp. 1901–1904, 1998.

[40] M. Bartelt, C. Stoldt, C. J. Jenks, P. A. Thiel, and J. W. Evans, “Adatom capture by arrays of two-dimensional Ag islands on Ag (100),” *Physical Review B*, vol. 59, no. 4, pp. 3125–3134, 1999.

[41] F. Gibou, C. Ratsch, M. Gyure, S. Chen, and R. Caflisch, “Rate equations and capture numbers with implicit islands correlations,” *Physical Review B*, vol. 63, no. 11, pp. 115 401–115 405, 2001.

[42] C. Ratsch, M. F. Gyure, R. E. Caflisch, F. Gibou, M. Petersen, M. Kang, J. Garcia, and D. D. Vvedensky, “Level-set method for island dynamics in epitaxial growth,” *Physical Review B*, vol. 65, p. 195403, 2002.

[43] C. Ratsch, M. Gyure, S. Chen, M. Kang, and D. Vvedensky, “Fluctuations and scaling in aggregation phenomena,” *Physical Review B*, vol. 61, no. 16, pp. R10 598–R10 601, 2000.

[44] M. Körner, M. Einax, and P. Maass, “Island size distributions in submonolayer growth: Prediction by mean field theory with coverage dependent capture numbers,” *Physical Review B*, vol. 82, p. 201401, 2010.

[45] ——, “Capture numbers and island size distributions in models of submonolayer surface growth,” *Physical Review B*, vol. 86, p. 085403, 2012.

[46] V. G. Dubrovskii and N. V. Sibirev, “Analytic scaling function for island-size distributions,” *Physical Review E*, vol. 91, p. 042408, 2015.

[47] V. G. Dubrovskii, “Exactly solvable model for cluster-size distribution in a closed system,” *Physical Review E*, vol. 95, pp. 012 135–012 141, 2017.

[48] J.-S. Ferenc and Z. Néda, “On the size distribution of Poisson Voronoi cells,” *Physica A: Statistical Mechanics and its Applications*, vol. 385, no. 2, pp. 518–526, 2007.

[49] V. Tokar and H. Dreyssé, “Size calibration of epitaxial islands via a two-step growth protocol: Kinetic Monte Carlo and effective-medium theory study,” *Surface Science*, vol. 637, pp. 116–123, 2015.

[50] D. L. González, A. Pimpinelli, and T. L. Einstein, “Fragmentation approach to the point-island model with hindered aggregation: Accessing the barrier energy,” *Physical Review E*, vol. 96, p. 012804, 2017.

[51] E. Placidi, E. Zallo, F. Arciprete, M. Fanfoni, F. Patella, and A. Balzarotti, “Comparative study of low temperature growth of InAs and InMnAs quantum dots,” *Nanotechnology*, vol. 22, no. 19, p. 195602, 2011.

[52] C. P. Joshi, Y. Shim, T. P. Bigioni, and J. G. Amar, “Critical island size, scaling, and ordering in colloidal nanoparticle self-assembly,” *Physical Review E*, vol. 90, p. 032406, 2014.

[53] M. Fanfoni, E. Placidi, F. Arciprete, E. Orsini, F. Patella, and A. Balzarotti, “Sudden nucleation versus scale invariance of InAs quantum dots on GaAs,” *Physical Review B*, vol. 75, p. 245312, 2007.

[54] S. Miyamoto, O. Moutanabbir, E. E. Haller, and K. M. Itoh, “Spatial correlation of self-assembled isotopically pure Ge/Si(001) nanoislands,” *Physical Review B*, vol. 79, p. 165415, 2009.

[55] V. I. Tokar and H. Dreyssé, “Universality and scaling in two-step epitaxial growth in one dimension,” *Physical Review E*, vol. 92, p. 062407, 2015.

[56] M. N. Popescu, J. G. Amar, and F. Family, "Rate-equation approach to island size distributions and capture numbers in submonolayer irreversible growth," *Physical Review B*, vol. 64, no. 20, pp. 205 404–205 417, 2001.

[57] P. Mulheran and D. Robbie, "Theory of the island and capture zone size distributions in thin film growth," *EPL (Europhysics Letters)*, vol. 49, no. 5, pp. 617–623, 2000.

[58] P. A. Mulheran, "The dynamics of island nucleation and growth—beyond mean-field theory," *EPL (Europhysics Letters)*, vol. 65, no. 3, pp. 379–385, 2004.

[59] J. W. Evans and M. C. Bartelt, "Nucleation, adatom capture, and island size distributions: Unified scaling analysis for submonolayer deposition," *Physical Review B*, vol. 63, no. 23, p. 235408, 2001.

[60] J. W. Evans and M. Bartelt, "Island sizes and capture zone areas in submonolayer deposition: Scaling and factorization of the joint probability distribution," *Physical Review B*, vol. 66, no. 23, pp. 235 410–235 422, 2002.

[61] A. Pimpinelli and T. Einstein, "Capture-zone scaling in island nucleation: universal fluctuation behavior," *Physical Review Letters*, vol. 99, no. 22, pp. 226 102–226 106, 2007.

[62] F. Shi, Y. Shim, and J. G. Amar, "Capture-zone areas in submonolayer nucleation: Effects of dimensionality and short-range interactions," *Physical Review E*, vol. 79, no. 1, pp. 011 602–011 608, 2009.

[63] M. Li, Y. Han, and J. W. Evans, "Comment on "capture-zone scaling in island nucleation: Universal fluctuation behavior"," *Physical Review Letters*, vol. 104, p. 149601, 2010.

[64] T. L. Einstein, A. Pimpinelli, and D. L. González, "Analyzing capture zone distributions (CZD) in growth: Theory and applications," *Journal of Crystal Growth*, vol. 401, pp. 67–71, 2014, proceedings of 17th International Conference on Crystal Growth and Epitaxy (ICCGE-17).

[65] M. Grinfeld, W. Lamb, K. O'Neill, and P. Mulheran, "Capture-zone distribution in one-dimensional sub-monolayer film growth: a fragmentation theory approach," *Journal of Physics A: Mathematical and Theoretical*, vol. 45, no. 1, p. 015002, 2011.

[66] M. A. Groce, B. R. Conrad, W. G. Cullen, A. Pimpinelli, E. D. Williams, and T. L. Einstein, "Temperature-dependent nucleation and capture-zone scaling of C60 on silicon oxide," *Surface Science*, vol. 606, no. 1, pp. 53–56, 2012.

[67] J. G. Amar, M. N. Popescu, and F. Family, "Rate-equation approach to island capture zones and size distributions in epitaxial growth," *Physical Review Letters*, vol. 86, no. 14, pp. 3092–3095, 2001.

[68] K. P. O'Neill, M. Grinfeld, W. Lamb, and P. Mulheran, "Gap-size and capture-zone distributions in one-dimensional point-island nucleation and growth simulations: Asymptotics and models," *Physical Review E*, vol. 85, no. 2, pp. 021 601–021 609, 2012.

[69] R. P. Treat, "On the similarity solution of the fragmentation equation," *Journal of Physics A: Mathematical and General*, vol. 30, no. 7, pp. 2519–2543, 1997.

[70] R. M. Ziff and E. McGrady, "Kinetics of polymer degradation," *Macromolecules*, vol. 19, no. 10, pp. 2513–2519, 1986.

[71] M. D. Penrose, A. R. Wade *et al.*, "Random minimal directed spanning trees and Dickman-type distributions," *Advances in Applied Probability*, vol. 36, no. 3, pp. 691–714, 2004.

[72] P. Šeba, "Parking and the visual perception of space," *Journal of Statistical Mechanics: Theory and Experiment*, vol. 2009, no. 10, p. L10002, 2009.

[73] P. Hansen, *Rank-Deficient and Discrete Ill-Posed Problems: Numerical Aspects of Linear Inversion*, ser. Mathematical Modeling and Computation. Society for Industrial and Applied Mathematics (SIAM), 1998.

[74] P. C. Hansen and D. P. O'Leary, "The use of the L-curve in the regularization of discrete ill-posed problems," *SIAM Journal on Scientific Computing*, vol. 14, no. 6, pp. 1487–1503, 1993.

[75] M. E. Hochstenbach and L. Reichel, "An iterative method for Tikhonov regularization with a general linear regularization operator," *J. Integral Equations Appl.*, vol. 22, no. 3, pp. 465–482, 2010.

[76] P. C. Hansen, "Analysis of discrete ill-posed problems by means of the L-curve," *SIAM review*, vol. 34, no. 4, pp. 561–580, 1992.

[77] G. H. Golub, M. Heath, and G. Wahba, "Generalized cross-validation as a method for choosing a good ridge parameter," *Technometrics*, vol. 21, no. 2, pp. 215–223, 1979.

[78] D. Calvetti, S. Morigi, L. Reichel, and F. Sgallari, "Tikhonov regularization and the L-curve for large discrete ill-posed problems," *Journal of computational and applied mathematics*, vol. 123, no. 1, pp. 423–446, 2000.

[79] P. C. Hansen, "Regularization tools: A Matlab package for analysis and solution of discrete ill-posed problems," *Numerical algorithms*, vol. 6, no. 1, pp. 1–35, 1994.

[80] M. Lallouache, A. Jedidi, and A. Chakraborti, "Wealth distribution: To be or not to be a Gamma?" *arXiv preprint arXiv:1004.5109*, 2010.

[81] R. Kress, *Linear Integral Equations*, ser. Applied Mathematical Sciences. Springer New York, 2013.

[82] V. Moretti, *Spectral Theory and Quantum Mechanics: With an Introduction to the Algebraic Formulation*, ser. UNITEXT. Springer Milan, 2013.

[83] P. Halmos, *A Hilbert Space Problem Book*, ser. Graduate Texts in Mathematics. Springer New York, 1982.

[84] A. Kirsch, *An Introduction to the Mathematical Theory of Inverse Problems*, ser. Applied Mathematical Sciences. Springer New York, 2011.